

AD_____

Award Number: DAMD17-98-1-8169

TITLE: 3-Dimensional Imaging of the Breast

PRINCIPAL INVESTIGATOR: Andrew D. Maidment, Ph.D.

CONTRACTING ORGANIZATION: Thomas Jefferson University
Philadelphia, Pennsylvania 19107

REPORT DATE: October 2002

TYPE OF REPORT: Final

PREPARED FOR: U.S. Army Medical Research and Materiel Command
Fort Detrick, Maryland 21702-5012

DISTRIBUTION STATEMENT: Approved for Public Release;
Distribution Unlimited

The views, opinions and/or findings contained in this report are those of the author(s) and should not be construed as an official Department of the Army position, policy or decision unless so designated by other documentation.

20030805 077

REPORT DOCUMENTATION PAGE

Form Approved
OMB No. 074-0188

Public reporting burden for this collection of information is estimated to average 1 hour per response, including the time for reviewing instructions, searching existing data sources, gathering and maintaining the data needed, and completing and reviewing this collection of information. Send comments regarding this burden estimate or any other aspect of this collection of information, including suggestions for reducing this burden to Washington Headquarters Services, Directorate for Information Operations and Reports, 1215 Jefferson Davis Highway, Suite 1204, Arlington, VA 22202-4302, and to the Office of Management and Budget, Paperwork Reduction Project (0704-0188), Washington, DC 20503

1. AGENCY USE ONLY (Leave blank)	2. REPORT DATE October 2002	3. REPORT TYPE AND DATES COVERED Final (15 Sep 98 - 14 Sep 02)
---	---------------------------------------	--

4. TITLE AND SUBTITLE 3-Dimensional Imaging of the Breast	5. FUNDING NUMBER DAMD17-98-1-8169
---	--

6. AUTHOR(S)
Andrew D. Maidment, Ph.D.

7. PERFORMING ORGANIZATION NAME(S) AND ADDRESS(ES)
Thomas Jefferson University
Philadelphia, Pennsylvania 19107

E-Mail: Andrew.Maidment@mail.tju.edu

8. PERFORMING ORGANIZATION REPORT NUMBER

9. SPONSORING / MONITORING AGENCY NAME(S) AND ADDRESS(ES)
U.S. Army Medical Research and Materiel Command
Fort Detrick, Maryland 21702-5012

10. SPONSORING / MONITORING AGENCY REPORT NUMBER

11. SUPPLEMENTARY NOTES

12a. DISTRIBUTION / AVAILABILITY STATEMENT
Approved for Public Release; Distribution Unlimited

12b. DISTRIBUTION CODE

13. ABSTRACT (Maximum 200 Words)

An experimental framework for performing 3-D imaging of the breast has been developed. The framework is designed to allow testing of many different detectors and acquisition protocols. We have developed and characterized three detectors. The first is now obsolete. The second detector is an active matrix amorphous-selenium device, and third uses a phosphor screen or an XRII optically coupled to a CCD camera. The second device has excellent dose efficiency (DQE) and resolution, but is too slow to allow easy tomographic imaging. The third device again has excellent resolution, but lacks the dose efficiency of the flat panel detector. This detector does, however, have the temporal response needed to perform CT. We have performed extensive evaluations of the reconstruction methods. In particular, we have concentrated on stereomammography and addressed the issue of dose in stereomammography. We have shown that stereomammography is possible at approximately the same dose as conventional projection mammography. This work considered the effect of x-ray quantum noise. To extend this work to other 3-D imaging techniques, and to consider additional effects, such as visual disparity and depth perception, we developed an extensive 3-D computer simulation of the breast.

14. SUBJECT TERMS
breast cancer, digital mammography, 3-D imaging of the breast, computed tomography, tomosynthesis, stereoscopy, limited-view reconstruction

15. NUMBER OF PAGES
113

16. PRICE CODE

17. SECURITY CLASSIFICATION OF REPORT
Unclassified

18. SECURITY CLASSIFICATION OF THIS PAGE
Unclassified

19. SECURITY CLASSIFICATION OF ABSTRACT
Unclassified

20. LIMITATION OF ABSTRACT
Unlimited

FOREWORD

Opinions, interpretations, conclusions and recommendations are those of the author and are not necessarily endorsed by the U.S. Army.

N/A Where copyrighted material is quoted, permission has been obtained to use such material.

N/A Where material from documents designated for limited distribution is quoted, permission has been obtained to use the material.

N/A Citations of commercial organizations and trade names in this report do not constitute an official Department of Army endorsement or approval of the products or services of these organizations.

N/A In conducting research using animals, the investigator(s) adhered to the "Guide for the Care and Use of Laboratory Animals," prepared by the Committee on Care and use of Laboratory Animals of the Institute of Laboratory Resources, national Research Council (NIH Publication No. 86-23, Revised 1985).

X For the protection of human subjects, the investigator(s) adhered to policies of applicable Federal Law 45 CFR 46.

N/A In conducting research utilizing recombinant DNA technology, the investigator(s) adhered to current guidelines promulgated by the National Institutes of Health.

N/A In the conduct of research utilizing recombinant DNA, the investigator(s) adhered to the NIH Guidelines for Research Involving Recombinant DNA Molecules.

N/A In the conduct of research involving hazardous organisms, the investigator(s) adhered to the CDC-NIH Guide for Biosafety in Microbiological and Biomedical Laboratories.


PI - Signature 1/24/03
Date

Table of Contents

Cover.....	1
SF 298.....	2
Table of Contents.....	4
Introduction.....	5
Body.....	6
Key Research Accomplishments.....	19
Reportable Outcomes.....	20
Conclusions.....	25
References.....	26
Appendices.....	27
Reprint: "Linear Response Theory for Detectors Consisting of Discrete Arrays" Medical Physics, 27(10), 2417-2434, October 2000	A-1
Reprint: "Mammogram synthesis using a 3-D simulation. I. Breast tissue model and the exam simulation", Medical Physics, 29(9), 2131-2139, September 2002	A-2
Reprint: "Mammogram synthesis using a 3-D simulation. II. Evaluation of synthetic mammogram texture", Medical Physics, 29(9), 2140-2151, September 2002	A-3
Preprint: "Classification of Galactograms using Ramification Matrices: Preliminary Results". Academic Radiology, 10(2), In Press, February 2003	A-4
Preprint: Effects of quantum noise on dose and contrast sensitivity in stereoradiography. Submitted to Medical Physics, September 18, 2002.....	A-5

1. Introduction

Previously, we developed a method to allow mammographic differential diagnosis based upon the 3-D orientation and morphology of breast calcifications. This method used a limited-view, binary reconstruction technique. In clinical trials, it was shown to be of value in instances where calcifications are associated with a mass. In such cases, we could distinguish between preferentially peripherally distributed calcifications that are predominantly benign and homogeneously distributed calcifications that are more likely to be malignant. We have also been able to elucidate the linear distribution of calcifications contained within a ductal system. Unfortunately, this reconstruction method does not allow one to image non-calcified tissues, or relate calcifications to the surrounding tissue. Thus, in the present study we have investigated alternative methods of generating 3-D images of the breast, namely stereoscopy, linear tomosynthesis, and micro-CT. Such methods capable of producing 3-D images of both calcifications and the surrounding breast tissue.

It is our purpose to develop a method that will be clinically viable in terms of dose, image quality and equipment cost. We believe that these proposed developments will further enhance the 3-D imaging and evaluation of breast cancer by allowing the radiologist to view calcifications in relation to the surrounding tissue, and to allow 3-D imaging of non-calcified breast tissues at doses which are clinically acceptable. Stereoscopy has the value of providing depth perception of tissues with little additional dose, however, often the small angle separating the views is insufficient to completely determine the causes of superposition. Tomosynthesis requires more views and potentially higher dose, but provides better separation of tissues. Artifacts from the reconstruction algorithms can blur synthetic tomograms. CT, while providing the best 3-D images requires doses that are not clinically acceptable.

This report summarizes the work on this grant.

2. Body

2.1. Summary of Work Items

It is useful to restate the work items listed in the original grant. They are as follows:

- Task 1: Develop 3-D imaging techniques (Months 1-24)
 - Subtask 1a: Stereoscopy (Months 1-4)
 - Subtask 1b: Linear Tomosynthesis (Months 5-8)
 - Subtask 1c: Limited View Reconstruction (Months 9-20)
 - Subtask 1d: Computed Tomography (Months 18-24)
- Task 2: Phantom Development (Months 1-24)
- Task 3: Evaluate 3-D imaging methods with phantoms (Months 1-36)
- Task 4: Acquire image datasets (Months 13-36)
- Task 5: Observer study (Months 25-36)

2.2. Development and Evaluation of 3-D Imaging Techniques

There has been considerable interest in imaging the breast in 3-D. This has included numerous radiographic methods including stereoscopy^{1,2}, tomosynthesis³, limited-view reconstruction of calcifications⁴⁻⁶, limited-view tomography reconstruction, and computed tomography⁷. There has also been interest in 3-D ultrasound, 3-D MRI, and other potential methods of imaging the breast in 3-D. However, to date, there has been a sizeable gap between the proposed techniques and clinical feasibility. To achieve clinical feasibility, it is necessary to consider these techniques on the basis of dose, fundamental imaging physics, and technology. This grant was designed to consider 4 such methods and compare them, both on the basis of physical performance and clinical images.

We had a number of difficulties completing this grant. Significant changes in clinical staff, clinical demands on the time of the participants of this grant, and the sale of a key piece of equipment by Thomas Jefferson University Hospital all served to retard progress on this grant, as reported previously. In spite of these difficulties, we believe that we have considerable advanced 3-D imaging of the breast. The following report details the results of this grant.

Image Acquisition Hardware

The grant originally proposed to use two pieces of hardware for the completion of this grant. The first was a prototype device built in Dr. Maidment's laboratory. It consisted of an Eikonix 1412 linear digital camera, coupled to an x-ray image intensifier (XRII) via lenses. These were mounted on an optical bench with a Siemens Bi150/30/50R x-ray tube, collimators, and a specimen holder mounted on a rotary motion stage. A Siemens Heliophos 5S generator supplied the x-ray tube. All of the components were connected to a 486-computer running Linux. A schematic of the imaging system is shown in figure 1. This system was intended for preliminary investigations. It had known image

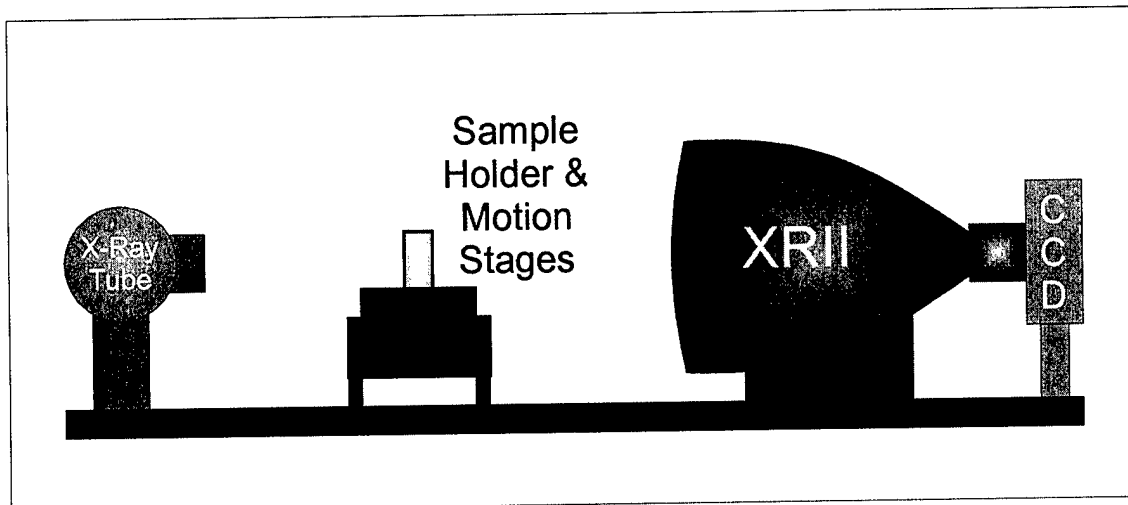


Figure 1 A schematic of the imaging system. The system consists of an x-ray tube, a system of translation and rotation stages for positioning the specimen, an x-ray image intensifier (XRII), lenses and a CCD camera. Pre- and post-object collimation is not shown.

quality problems that would prevent its use through the entire study. Fortunately, a second system existed at that time which had significantly better image quality.

The second system consisted of a Fischer Mammotest stereotactic core biopsy system and a Fischer MammoVision digital x-ray detector (Fischer Imaging, Denver, CO). We have had a long-standing relationship with the Fischer R&D group, and Fischer had for many years provided technical support for this work. The Fischer system was supposed to be modified to include a computer-controlled rotator stage. This would allow us to mount a specimen holder on this stage and use the Fischer system to produce tomographic images. This system was being developed, in part, because of its physical location in the Breast Imaging Center, which is in the same building as our outpatient breast surgery center. We had planned to interview women prior to needle localization, including obtaining informed consent. Then, following their surgery, the surgical specimen would be rapidly imaged on the modified Fischer table. Unfortunately, the hospital sold this unit, August 10th, 1999, just 8 weeks after we hired a post-doc for this grant.

Since that time, we have made a concerted effort to allow this grant to proceed. We have done this in two ways. First, we have altered the original imaging system by replacing the image intensifier and Eikonix camera with a 4" XRII (Toshiba), and an SMD (SMD, Fort Collins, CO) 1M30 CCD camera. The acquisition computer and electronics were also updated. We have characterized their performance, and used the system for computed tomography. Secondly, we obtained a DRC (DRC is a subsidiary of Hologic, Wilmington, DE) amorphous selenium active matrix detector. This system was used for tomosynthesis and stereoscopy. In the following sections, the performance of the various imaging systems is discussed. Then, a summary of the research in the four imaging modalities is presented, concentrating primarily on stereoscopy.

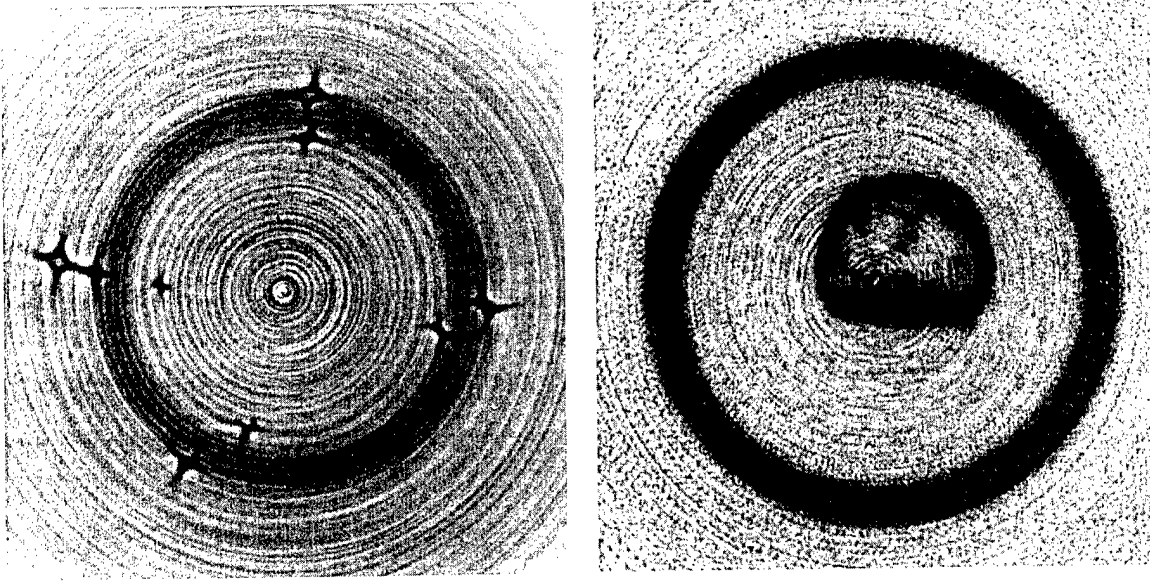


Figure 2 Reconstructed images produced with the Eikonix detector. The left image is a wire phantom designed to test rotational artifacts. Note that the wire is reconstructed with different levels of success (they should look like dots, not crosses). Also note the circular artifacts due to the instability of the XRII. The image on the right is of a fresh chicken thighbone (8.8 mm x 7.4 mm), clearly showing a ring of cortical bone, and details within the medullary cavity. This image still demonstrates subtle circular artifacts that limit the detection of low contrast structures in the bone.

Detector Characterization

In each of the designs discussed below, a Siemens Heliophos 5S x-ray generator and a Siemens Bi150/30/50R x-ray tube, a Parker computer controlled rotary stage, and a custom specimen/phantom holder are used. These form the basis of the imaging system being built. They are all mounted on an optical breadboard that is equipped with appropriate rails and mounting hardware. A rotate only geometry is used to acquire images. The setup allows acquisition of either tomographic or stereoscopic images, depending upon the acquisition protocol used, by varying the angle of acquisition and the dose per image. Each detector is capable of acquiring 2-D images, and hence 3-D volume reconstruction is also possible.

Eikonix Detector

The first detector built consisted of an Eikonix 1412 digital linear camera and a Siemens 9"/6" x-ray image intensifier (XRII). Because this was a linear camera, true CT images were acquired differently than the other methods. In the limited view methods (including stereoscopy), 2-D images were acquired by scanning the detector at selected angles. However, due to time constraints, CT images were made in two different ways. Angular sub-sampling allowed us to acquire up to 200 images for 3-D reconstruction. Alternatively, 1-D images could be acquired at a greater number of angles, but only a single 2-D slice of the object would be reconstructed.

This camera was used to develop the image reconstruction algorithms used for the CT images (discussed in detail below). In the original grant application, the CT images that were shown, were of very high contrast objects, and were acquired as 1-D samples to produce a single 2-D slice. A conventional filtered back-projection reconstruction algorithm was used. Since that time, we have altered our image acquisition code to allow 2-D images to be acquired, and now use a modified Feldkemp algorithm to generate a stack of 2-D slices, which are rendered as 3-D volume data sets.

Use of the Eikonix camera was discontinued due to circular and cross artifacts illustrated in the reconstructed images shown in figure 2. In August, 2000, we decided to change detector designs.

DRC Detector

At the time of our decision to abandon the Eikonix camera, we considered two possible designs. The first was based upon a DRC active matrix detector that we had in our laboratory. This system has very high modulation transfer function (MTF) (see figure 3), and excellent noise power spectra (NPS) and detective quantum efficiency (DQE). These data were measured in our laboratory. In support of this work, we did extensive modeling and experimentation. This work was reported in Medical Physics in October 2000, a reprint (Appendix 1) of which is included with this report⁸. The system has been used to acquire tomographic images. Examples are shown in figures 8 and 9 during the discussion of computed tomography

The great strength of this detector is the image quality. We continue to use it for at least some of experiments to test individual 3-D acquisition methods. However, this detector is very slow, producing one image every 40 to 50 seconds. Thus, even using angular-undersampling, tomographic images produced from 200 individual views take more than 2 hours to acquire. Thus, we had to look for a different detector to perform our CT research.

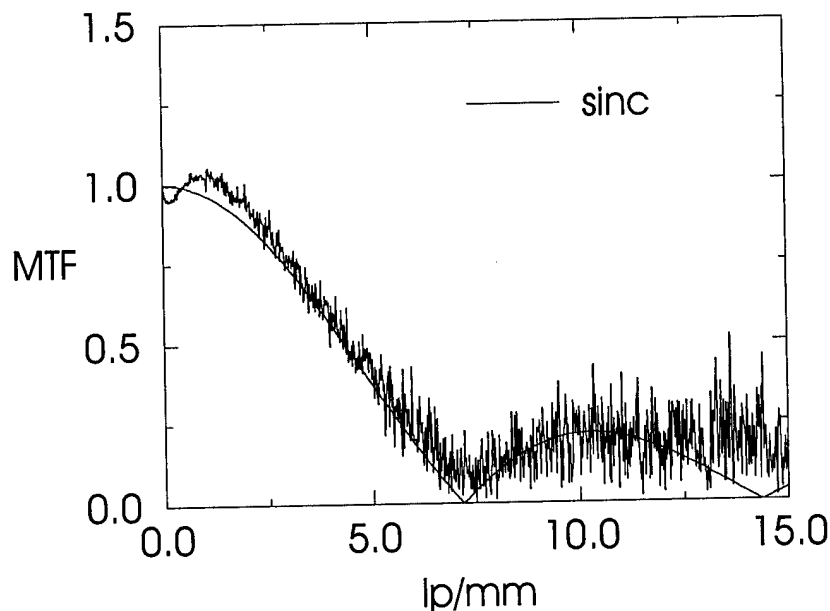
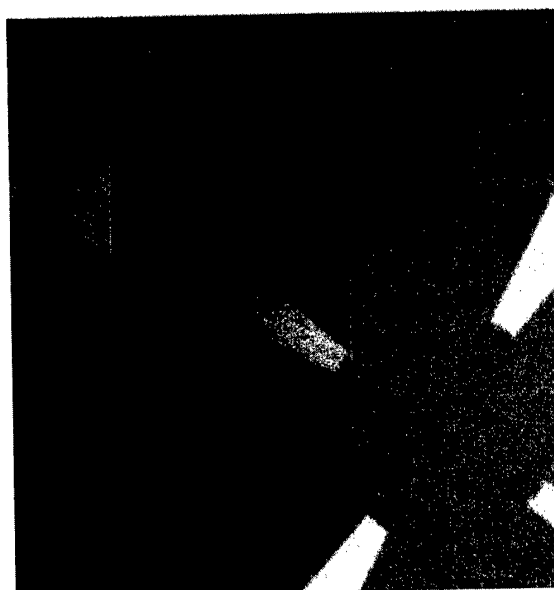


Figure 3 MTF of the DRC detector, compared with the ideal MTF of a sinc function. Note that a small amount of edge enhancement occurs due to the use of an amorphous selenium photoconductor

SMD Detector

The second new detector design was based upon a CCD camera that was coupled with lenses to a phosphor screen, or to a newer 4" Toshiba XRIL. This design allows us to use a very fast camera. The camera we chose is capable of imaging at 30 frames a second. This allows tomographic images to be acquired in as little as 7 seconds for 200 projections to 34 seconds for 1000 projections. However, now we faced limitations of the x-ray generator, which extend that time to a few minutes. The problem with this design is that it is only ever going to be useful as a laboratory system. The use of lenses to couple light from a phosphor screen to a CCD camera is quite inefficient. Our

Figure 4 A portion of a resolution phantom, showing a limiting resolution of 11.3 lp/mm, acquired with the SMD detector, a Lanex phosphor screen, and 85mm:55mm relay lenses giving an overall field of view of 20 mm. A subsection of the image is enhanced for printing.



calculations have shown that as little as 2 light quanta per x-ray interaction may be recorded. We have shown previously⁹⁻¹⁰ that this inefficiency can result in needing higher doses for the patients (or test objects). As a result, we could only image tissue samples and inanimate test objects. It is our expectation that a clinical system could use one of the newer active matrix arrays that are capable of 10 to 30 frames per second, and which would be dose efficient.

We obtained a demonstration detector from the manufacturer during the period of December 2000 to February 2001, and finally installed the permanent system in May 2001. During that time, we wrote the necessary software to control the camera with the existing x-ray system. We performed preliminary testing of the camera, and were satisfied with the performance. An example of a resolution pattern is shown in figure 4.

Image Technique Optimization

Stereoscopy

Stereoscopy is the process by which two views of a scene, obtained at slightly different angles (such as that due to the displacement of our two eyes) provides the viewer with the perception of depth (i.e., the ability to discern that one object is behind another). This process can be applied to radiographic imaging to achieve a similar perception of depth. Originally, we proposed to perform a Raleigh discrimination test to determine optimal angular separation for radiographic imaging. However, work by others in the field, including Chan¹ led us to consider other pertinent research questions. In particular, the issue of dose was particularly important and previously un-addressed. We have expended considerable time on this question.

In the case of a quantum-noise limited detector, signal detection theory suggests that stereoradiographic images can be acquired with one half of the per-image dose needed for a standard radiographic projection, as information from the two stereo images can be combined. Previously, film-screen stereoradiography has been performed using the same per-image dose as in projection radiography, i.e., doubling the total dose. In the resulting paper (Appendix 5), the assumption of a possible decrease in dose for stereoradiography was tested by a series of contrast-detail experiments, using phantom images acquired over a range of exposures. The number of visible details, the effective reduction of the dose, and the effective decrease in the threshold SNR were determined using human observers under several display and viewing conditions. These results were averaged over five observers and compared with multiple readings by a single observer and with the results of an additional observer with limited stereo vision. Experimental results show that the total dose needed to produce a stereoradiographic image pair is approximately 1.1 times the dose needed for a single projection in standard radiography. The observed benefit was greatest when the images were displayed to emphasize the quantum noise, and decreased with increasing dose. To further this work to the more general situation of arbitrary objects, with varying degrees of depth perception, and for use in different imaging systems, it was necessary to develop a 3-D computer breast phantom. This is described in more detail below.

Linear Tomosynthesis

We have also performed preliminary experiments with regard to linear tomosynthesis, using the Fischer Mammovision stereotactic breast imaging system, prior to its sale. For each tomosynthetic data set, fifteen images were acquired as the x-ray tube was moved through a 30 degrees arc. The advantage of synthetic tomography over conventional tomography is that the set of 15 images can be used to reconstruct an arbitrary number of planes, while in conventional tomography each image plane requires an additional x-ray exposure

The principles of tomosynthesis are illustrated in figure 5. As the x-ray focus is moved, the imaging plane \mathbf{P} is held fixed. To perform a reconstruction, each x-ray image is viewed as a gray-scale function g_i defined on a region P_r of the imaging plane \mathbf{P} , where i enumerates the x-ray exposure. For each plane \mathbf{Q} parallel to \mathbf{P} in which reconstruction will be performed, each projection position of the x-ray focus defines a one-to-one correspondence of points in the plane \mathbf{Q} with the points in the plane \mathbf{P} . Explicitly, for the i -th position of the x-ray tube, for each point q in \mathbf{Q} , there is a line passing through the focus and q which meets \mathbf{P} in a unique point p . Thus for every i there is a "projective" transformation between the points of \mathbf{P} and \mathbf{Q} . Further, the gray-scale function g_i on P_r can now be considered as a function g'_i defined in the region Q_i in the plane \mathbf{Q} , and the value of the reconstructed gray scale image at a point q is the sum of all the g'_i which are defined at that point. As with conventional tomography, for objects lying within the plane \mathbf{Q} , the functions g'_i add coherently to produce a focused image, while for objects outside the plane are blurred. An example of images of a preliminary tomosynthesis phantom is shown in figures 6 and 7. The phantom consists of Lucite spheres and cubes contained in a water-filled Lucite box. This box is superimposed upon a contrast-detail phantom. In figure 6, three projection images of this phantom are shown. These images demonstrate the overlaying "clutter" of the spheres and cubes that effectively obscure most of the features of the contrast-detail phantom. Even at 10 times the dose this image was acquired at, we could not visualize more than 5 objects of the contrast-detail phantom. In figure 7, we show three reconstructions of the phantom at different heights above the detector. Two sections contain only the acrylic spheres. At a height of 10 mm, however, the contrast-detail phantom can be seen. In this image, 24 contrast-detail elements are visible. The increase in detection is due to the reduction in the overlaying clutter. Thus, reduction of this structural noise results in an increase in the effective SNR of the contrast-detail elements, without requiring an increase in dose.

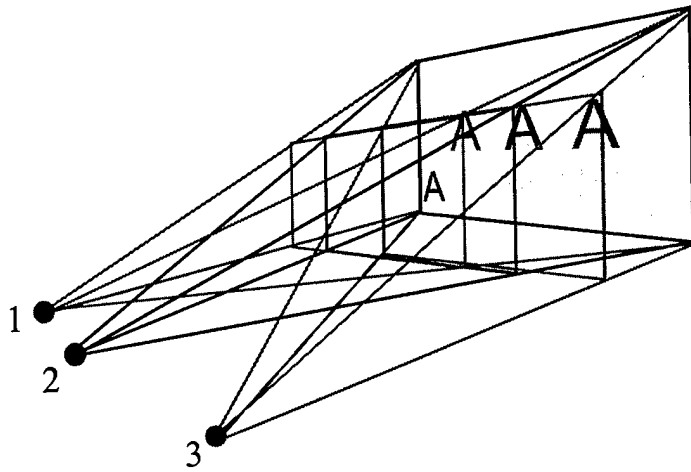


Figure 5 An x-ray tube is shown at three locations (1,2,3); the imaging plane, P, is held fixed. An image of the letter "A", located in a plane Q is projected to three different locations on the detector. Note that the individual regions Q_i overlap.

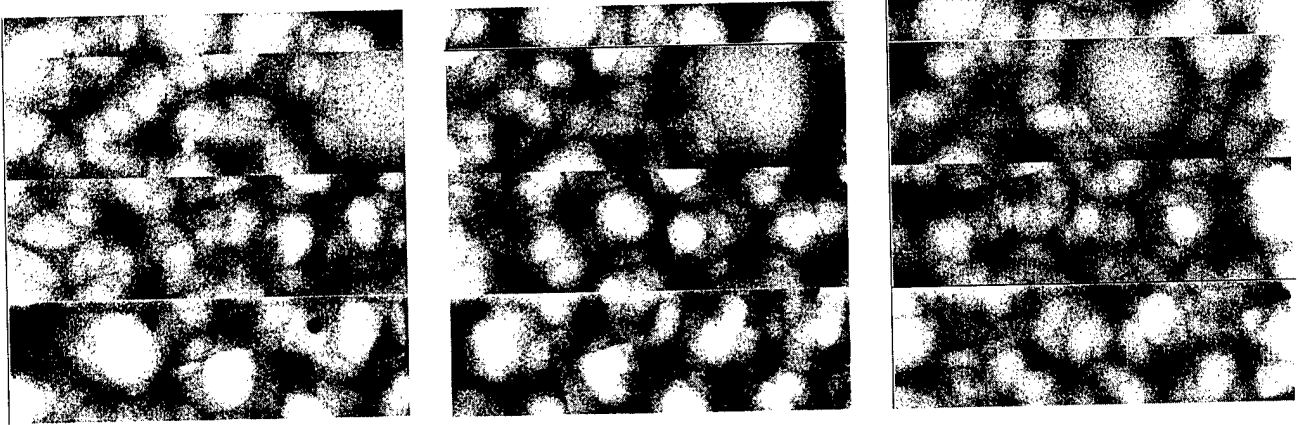


Figure 6 Three source images of a tomosynthesis phantom. The lead BB's on the top edge act as fiducial markers for determining the angle of the image. The phantom consists of lucite cubes and spheres in a water bath. Attached is a contrast detail phantom. The low contrast elements of the contrast detail phantom are not readily seen.

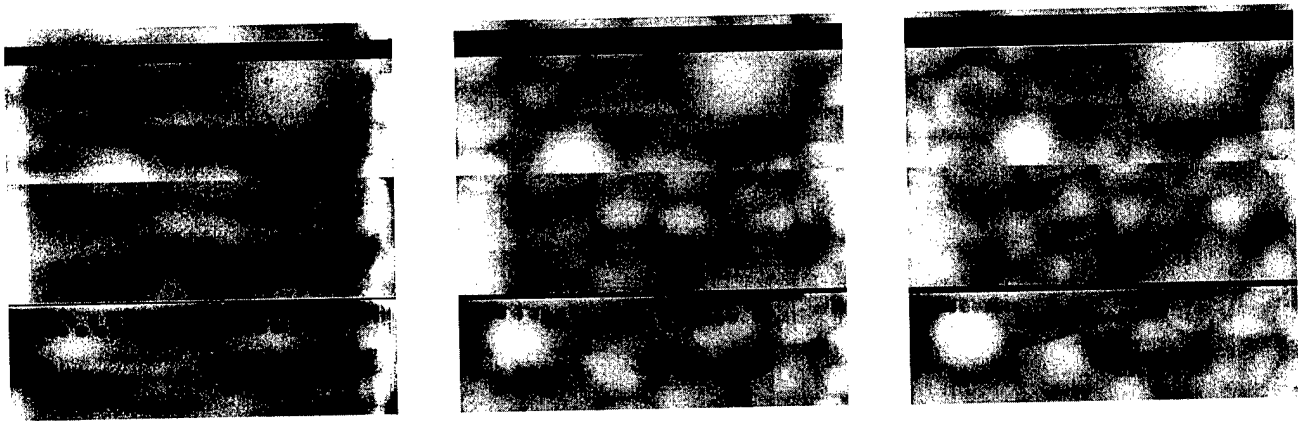


Figure 7 The tomosynthetic images of the phantom shown in figure XX. The phantom is shown at three different depths, including one that incorporates the contrast-detail elements (leftmost). Numerous elements are now visible

Computed Tomography

A computed microtomography system has been built to image breast specimens. The system has been evaluated. As discussed above, the system has been built so that it can accommodate two different types of detectors, a DRC active matrix detector, and one based on a phosphor screen optically-coupled to a CCD camera. The DRC detector is complete, while the CCD based detector was completed in the summer of 2002.

We evaluated both conventional and fully 3-D CT image acquisition methods. Experimentally, we have acquired images using between 200 and 1000 projections, rotating over an angle of 360°. Given the acquisition geometry used, there is a minimum number of projections that are required to avoid undersampling the projection space. This number depends upon many factors including the object size and detector pitch. However, undersampling generally only causes artifacts in very highly attenuating objects such as bone. Thus, given the low attenuation of breast tissues, undersampling is likely to be less of a problem.

For performing simple axial reconstructions, the projection data are reconstructed using a filtered back-projection algorithm (RECLBL, Donner Laboratory). A Hanning filter is used in the reconstruction. Prior to reconstruction, the projection data are corrected for pixel-to-pixel variations in the detector response, fluctuations in x-ray exposure between projections, and error in the center of rotation.

Numerous phantoms have been constructed and imaged. Two are shown in figure 8. Shown are a tomographic resolution test object and a uniformity test object. The resolution test object has 5 rows of holes, varying in size from 1/16" to 1/64". All are clearly visible. The uniformity test object (right) consists of a Lucite cylinder 1" in diameter. The image demonstrates a very uniform background without cupping or other

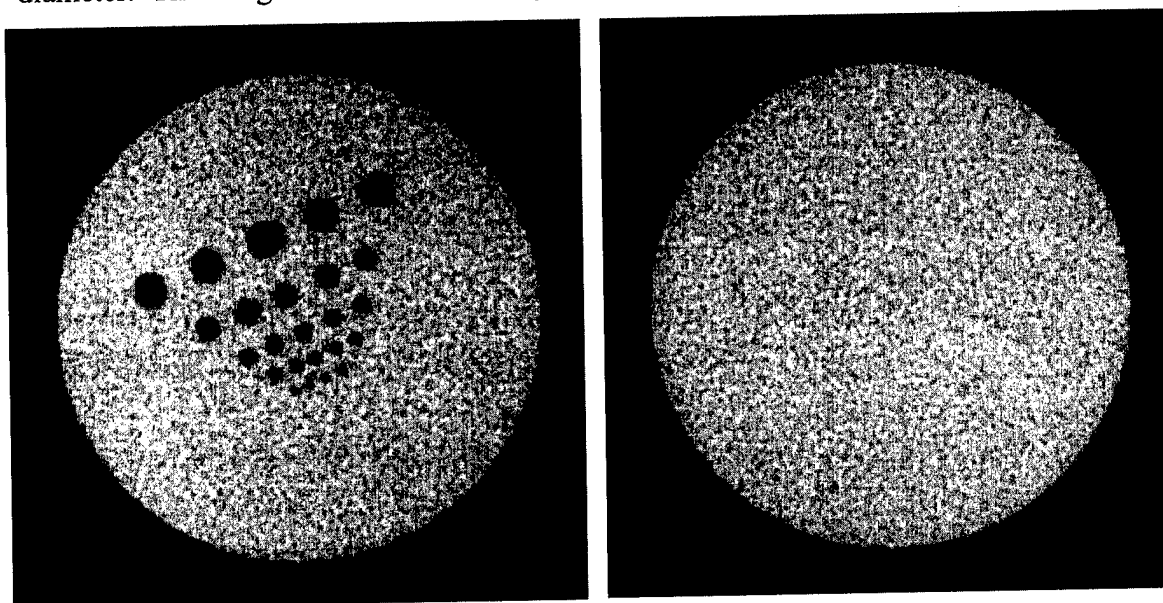


Figure 8 Two reconstructed axial images, acquired with a CT scanner based on the DRC detector. The image on the left shows a resolution phantom, with elements of size 1/16" to 1/64" all visible. On the right is a uniform lucite phantom, clearly showing the image uniformity and low noise that is achievable.

artifacts. These images show the excellent potential of using the DRC detector to produce tomographic images.

Shown in figure 9 are some 3-D images of biological tissue. The 3-D images are rendered in two different ways, surface rendering and volume rendering. Both show exquisite detail. We believe that these are the first CT images of *periplaneta Americana*. We chose to image this species due to its ready availability and due to the size of the anatomic structures. Simply stated, this represents a hard imaging task. Attention should be paid to the quality of the reconstruction of the leg muscles. Note that the muscle fibers inside the insect's exoskeleton are clearly visible and discernable. Similarly, part of the exoskeleton is seen. The muscles are less than 1 mm in diameter and less than 200 microns separate them at their closest point.

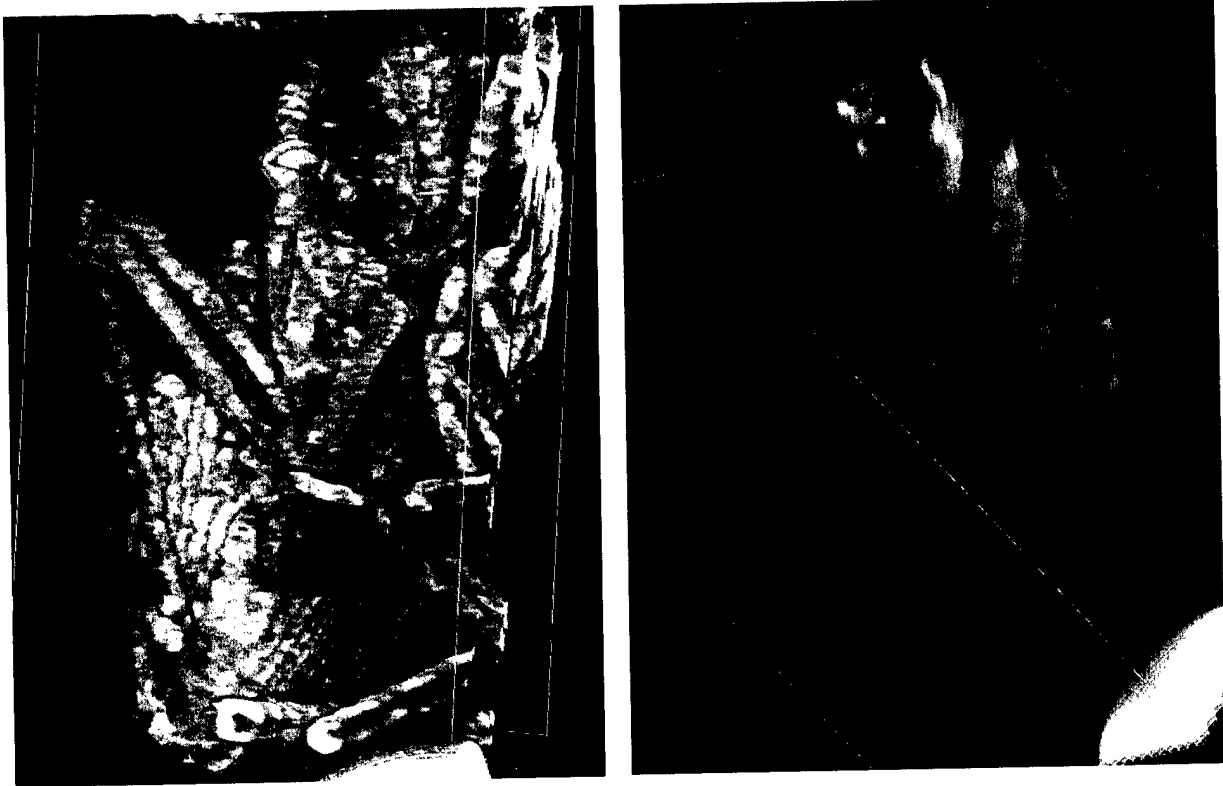


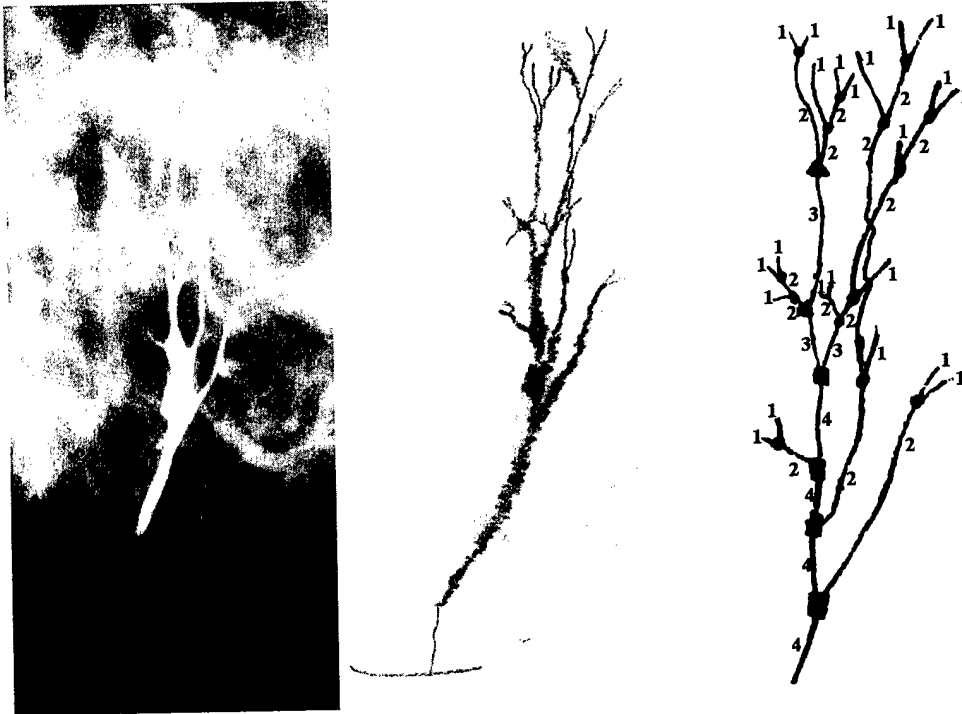
Figure 9 Surface rendered (left), and volume rendered (right) microtomography images of species *periplaneta Americana* (common American cockroach), acquired with the DRC detector. The insect is approximately 25 mm long. The muscle fibers and the exoskeleton of the legs are clearly visible.

3-D Breast Model

The observer experiments for stereomammography, stimulated considerable interest by a number of groups, and motivated us to consider this problem more carefully. Much of the last half of the grant was spent specifically addressing the issues of the dose requirements for 3-D imaging of the breast. Such questions must be addressed either through phantom experiments or computer simulations. The number of x-ray images needed to perform this research solely using phantom images was prohibitive. So, we had to develop a suitable computer simulation of the breast. This simulation is discussed in detail in Appendices 2 and 3. The phantom consists of a 3-dimensional array of geometric objects positioned using rules developed from observing MRI and subgross histology specimens. The phantom can have various properties associated with it, such as mechanical properties, x-ray attenuation coefficients, MRI or ultrasound properties. To date, we have only simulated x-ray imaging with breast compression. This model has generated more collaborative research interest than any other research project that we have ever worked on. Currently more than 10 research groups are using this model worldwide.

Breast Duct Analysis

Although not originally part of the statement of work, there has been an interested side-research project, which developed from this grant. This project, based upon ramification matrices, originated when we found it necessary to simulate the breast ductal network for the breast simulation described above. We evaluated a number of galactograms to measure the branching properties of the ductal tree. These measurements were then used in modeling the breast. However, it was noted that the measured ramification matrix values correlated with radiographic appearance of the galactograms. We have investigated this further, and have shown that there is a strong correlation between ductal branching and disease state. This work has been published (Appendix 4). This work has led to more collaborative research, where we intend to look at the effect of breast ductal network structure as a predictive metric of breast cancer risk, both in humans and murine models.



2.3. Discussion and Summary of Scientific Results

This grant has generated significant progress toward developing an experimental and theoretical (computational) framework for performing 3-D imaging of the breast. The experimental framework consists of an x-ray generator, x-ray tube, collimators, and rotary stage for holding specimens or phantoms. Each of the components is under computer control. The framework is designed to use standard optical mounting hardware and an optical breadboard to allow testing of many different detectors and acquisition protocols.

We have developed and characterized two detectors that fit within this framework. The first detector is an active matrix amorphous-selenium device, and second uses a phosphor screen or XRII optically coupled to a CCD camera. The first device has excellent dose efficiency (DQE) and resolution, but is too slow to allow easy tomographic imaging. The latter device again has excellent resolution, but lacks the dose efficiency of the flat panel detector. This detector does, however, have the temporal response needed to perform CT.

We have performed extensive evaluations of the reconstruction methods. In particular, we have concentrated on stereomammography and addressed the issue of dose in stereomammography. We have shown that stereomammography is possible at approximately the same dose as conventional projection mammography. This work considered the effect of x-ray quantum noise. To extend this work to other 3-D imaging techniques, and to consider additional effects, such as visual disparity and depth perception, we developed an extensive 3-D computer simulation of the breast. This work in turn, has led to efforts in characterizing breast tissue based upon breast ductal branching.

3. Key Research Accomplishments

The following is a list of key research accomplishments resulting from this work:

- Developed a generic testbed for 3-D imaging research, consisting of x-ray generator, rotary stage, specimen/phantom holder, and detector assembly.
- Developed three different detectors
 - the original was based on an Eikonix linear CCD coupled to an XRII
 - the second was based on a DRC active matrix detector
 - the third was based on an SMD 30 fps CCD camera
- Developed stereotactic, tomosynthetic, and volume rendering display software
- Developed theoretical framework for measuring and calculating the physical performance of aliasing and non-aliasing digital x-ray detectors.
- Performed dose optimization of stereoscopy based on experimental and theoretical techniques.
- Developed a 3-D breast simulation for projection and tomographic imaging of the breast using x-rays (and potentially other imaging modalities).
- Developed (as a result of the model) a method to analysis breast ductal network branching, and have identified a relationship to radiographic findings.

4. Reportable Outcomes

a) Published Manuscripts

Theses

1. P.R. Bakic, "Breast Tissue Description and Modeling in Mammography", Lehigh University, Department of Electrical Engineering, Ph.D. Thesis, December 2000.

Peer Reviewed

1. Michael Albert, and Andrew D.A. Maidment. Linear Response Theory for Detectors Consisting of Discrete Arrays. *Medical Physics*, **27**(10), 2417-2434, October 2000.
2. P.R. Bakic, M. Albert, D. Brzakovic, and A.D.A. Maidment. Mammogram Synthesis using a 3-D simulation: I. Breast Tissue Model and the exam simulation. *Medical Physics*, **29**(9), 2131-2139, September 2002.
3. P.R. Bakic, M. Albert, D. Brzakovic, and A.D.A. Maidment. Mammogram Synthesis using a 3-D simulation: II. Evaluation of Synthetic Mammogram Texture. *Medical Physics*, **29**(9), 2140-2151, September 2002.
4. P.R. Bakic, M. Albert, and A.D.A. Maidment. Classification of Galactograms using Ramification Matrices: Preliminary Results. *Academic Radiology*, **10**(2), In Press, February 2003.
5. A.D.A. Maidment, P.R. Bakic, and M. Albert. Effects of quantum noise on dose and contrast sensitivity in stereoradiography. Submitted to *Medical Physics*, September 18, 2002.

Proceedings Papers

1. P. Bakic, M. Albert, D. Brzakovic, A.D.A. Maidment, "Generation and Evaluation of Physically Inspired Synthetic Mammograms", CD-ROM Proceedings of the World Congress on Medical Physics and Biomedical Engineering, 4, July 23-28, 2000.
2. P. Bakic, M. Albert, A.D.A. Maidment, and B. Reljin, "Experiment with 3-D Mammography and their Possible Applications in Telemammography," *Annals of the Academy of Studenica*, **4**, 67-69 (2001).
3. P.R. Bakic, M. Albert, D. Brzakovic, A.D.A. Maidment. Evaluation of a Mammography Simulation. In *IWDM 2000 5th International Workshop on Digital Mammography*, edited by M.J. Yaffe, Medical Physics Publishing, Madison WI, 681-687 (2001).

4. P.R. Bakic, M. Albert, and A.D.A. Maidment. Dose Requirements in Stereoradiography. In Physics of Medical Imaging edited by L. Antonuk and M.J. Yaffe, Proceedings of the SPIE, **4682**, 126-137 (2002).
5. A.D.A. Maidment, P.R. Bakic, and M. Albert. Is Stereomammography Possible Without Increased Dose. In IWDM 2002, 6th International Workshop on Digital Mammography, edited by H-O Peitgen, In press (2002).
6. P.R. Bakic, M. Albert, and A.D.A. Maidment,. Evaluation of Breast Ductal Networks Using Ramification Matrices. In IWDM 2002, 6th International Workshop on Digital Mammography, edited by H-O Peitgen, In press (2002).

b) Abstracts and Presentations

Abstracts

1. A.D.A. Maidment, 3-D Imaging of the Breast. Program for the "6th International Cambridge Conference on Breast Cancer Screening", April 1999.
2. A.D.A. Maidment. "3-D Imaging of the female breast". Program for "Imaging 2000", June 2000.
3. A.D.A. Maidment, and M. Albert. "A Clinical Study of Calcifications Imaged by 2-D and 3-D Digital Mammography". Program for "DOD Era of Hope", Vol. 1, p. 212, June 2000.
4. A.D.A. Maidment, and M. Albert. "3-D Digital Mammography: An Automated Method of Image Reconstruction". Program for "DOD Era of Hope", Vol. 1, p. 213, June 2000.
5. A.D.A. Maidment, P. Bakic and M. Albert. "3-D Digital Mammography: A Comparison of Image Reconstruction Methods". Program for "DOD Era of Hope", Vol. 1, p. 214, June 2000.
6. A.D.A. Maidment, M. Albert. Automated Reconstruction of 3-D Calcifications. Program for "TWDM 2000 – 5th International Workshop on Digital Mammography", p. 26, June 2000.
7. P.R. Bakic, M. Albert, D. Brzakovic, A.D.A. Maidment. Evaluation of a Mammography Simulation. Program for "TWDM 2000 – 5th International Workshop on Digital Mammography", p. 123, June 2000.
8. A.D.A. Maidment. "3-D Imaging of the female breast". Program for "Imaging 2000", June 2000.

9. A.D.A. Maidment, and M. Albert, "Automated 3-D Limited-View Binary Reconstruction of Breast Calcifications", CD-ROM Proceedings of the World Congress on Medical Physics and Biomedical Engineering, 4, July 23-28, 2000.
10. P.R. Bakic, M. Albert, and A.D.A. Maidment. Dose Requirements in Stereoradiography. Program for "Physics of Medical Imaging", p. 36, February 2002.
11. A.D.A. Maidment, P.R. Bakic, and M. Albert. Is Stereomammography Possible Without Increased Dose. IWDM 2002 Program & Abstracts – 6th International Workshop on Digital Mammography, p. 27 June 2002.
12. P.R. Bakic, M. Albert, and A.D.A. Maidment. Evaluation of Breast Ductal Networks Using Ramification Matrices. IWDM 2002 Program & Abstracts – 6th International Workshop on Digital Mammography, p. 78, June 2002.
13. A.D.A. Maidment, P.R. Bakic, and M. Albert. Dose Requirements in Stereomammography. The Department of Defense Breast Cancer Research Program Meeting – Era of Hope Proceedings. Volume II, p. 30-6, September 2002.
14. A.D.A. Maidment, P.R. Bakic, and M. Albert. 3-Dimensional Imaging of the Breast. The Department of Defense Breast Cancer Research Program Meeting – Era of Hope Proceedings. Volume II, p. 30-7, September 2002.
15. P.R. Bakic, M. Albert and A.D.A. Maidment. "Quantum Noise and Dose in Digital Stereomammography: A 2-AFC Observer Study", Radiology, 225(P), 644 (2002).

Presentations

1. A.D.A. Maidment, M. Albert, E.F. Conant, and S.A. Feig. Three-Dimensional Visualization of Breast Cancer. 4th International Workshop on Digital Mammography, Nijmegen, The Netherlands, June 10, 1998.
2. A.D.A. Maidment, 3-D Imaging of the Breast. 6th International Cambridge Conference on Breast Cancer Screening. Cambridge, England. April 14, 1999. (Invited Presentation)
3. A.D.A. Maidment, and M. Albert. "A Clinical Study of Calcifications Imaged by 2-D and 3-D Digital Mammography". DOD Era of Hope, Atlanta, GA, June 8-11, 2000.
4. A.D.A. Maidment, and M. Albert. "3-D Digital Mammography: An Automated Method of Image Reconstruction". DOD Era of Hope, Atlanta, GA, June 8-11, 2000.

5. A.D.A. Maidment, P. Bakic and M. Albert. "3-D Digital Mammography: A Comparison of Image Reconstruction Methods". DOD Era of Hope, Atlanta, GA, June 8-11, 2000.
6. P. Bakic, M. Albert, D. Brzakovic, and A.D.A. Maidment. "Evaluation of a Mammography Simulation". 5th International Workshop on Digital Mammography, Toronto, Canada, June 11-14, 2000.
7. A.D.A. Maidment, and M. Albert. "Automated Reconstruction of 3-D Calcifications". 5th International Workshop on Digital Mammography, Toronto, Canada, June 14, 2000.
8. A.D.A. Maidment. "3-D Imaging of the female breast". Imaging 2000, Stockholm, Sweden, June 29, 2000. (Invited Presentation)
9. A.D.A. Maidment, and M. Albert. "Automated 3-D Limited-View Binary Reconstruction of Breast Calcifications". 42nd Annual Meeting of the American Association of Physicists in Medicine, Chicago, IL, July 25, 2000.
10. P. Bakic, M. Albert, D. Brzakovic, and A.D.A. Maidment. "Generation and Evaluation of Physically Inspired Synthetic Mammograms". 42nd Annual Meeting of the American Association of Physicists in Medicine, Chicago, IL, July 25, 2000.
11. P.R. Bakic, M. Albert, and A.D.A. Maidment, "Dose Requirements in Stereoradiography", SPIE Medical Imaging 2002 (Physics of Medical Imaging), San Diego, California, February 24, 2002.
12. A.D.A. Maidment, P.R. Bakic, and M. Albert. "Is Stereomammography Possible Without Increased Dose", 6th International Workshop on Digital Mammography, Bremen, Germany, June 24, 2002.
13. "Networks Using Ramification Matrices", 6th International Workshop on Digital Mammography, Bremen, Germany, June 25, 2002.
14. A.D.A. Maidment, P.R. Bakic, and M. Albert. Dose Requirements in Stereomammography. The Department of Defense Breast Cancer Research Program Meeting – Era of Hope, Orlando, FL, September 25-28, 2002.
15. A.D.A. Maidment, P.R. Bakic, and M. Albert. 3-Dimensional Imaging of the Breast. The Department of Defense Breast Cancer Research Program Meeting – Era of Hope, Orlando, FL, September 25-28, 2002.
16. P.R. Bakic, M. Albert and A.D.A. Maidment. "Quantum Noise and Dose in Digital Stereomammography: A 2-AFC Observer Study", 88th Scientific Assembly of the Radiological Society of North America, Chicago, IL, Dec. 6, 2002.

c) Funding Applications

Funded Grants

1. Department of Defense, DAMD17-00-1-0465, "A Novel Method for Determining Calcification Composition", Andrew D. A. Maidment, PI.
2. Department of Defense, DAMD 17-02-1-0593, "Polarization Imaging", Andrew D. A. Maidment, PI.

Current Grant Applications

1. RSNA Seed Grant, "Analysis of Breast Ductal Branching by Automated Tracing from MR Galactograms", Predrag R. Bakic, PI, Submitted 1/15/03

Research Personnel

Andrew D. A. Maidment, Ph.D.	Principle Investigator
Michael Albert, Ph.D.	Programmer and Research Assistant.
Predrag Bakic, Ph.D.	Post-Doctoral Fellow.

5. Conclusions

An experimental framework for performing 3-D imaging of the breast has been developed. This framework consists of an x-ray generator, x-ray tube, collimators, and rotary stage for holding specimens or phantoms. Each of the components is under computer control. The framework is designed to use standard optical mounting hardware and an optical breadboard to allow testing of many different detectors and acquisition protocols.

We have developed and characterized three detectors. The first is now obsolete. The second detector is an active matrix amorphous-selenium device, and third uses a phosphor screen or an XR11 optically coupled to a CCD camera. The second device has excellent dose efficiency (DQE) and resolution, but is too slow to allow easy tomographic imaging. The third device again has excellent resolution, but lacks the dose efficiency of the flat panel detector. This detector does, however, have the temporal response needed to perform CT.

We have performed extensive evaluations of the reconstruction methods. In particular, we have concentrated on stereomammography and addressed the issue of dose in stereomammography. We have shown that stereomammography is possible at approximately the same dose as conventional projection mammography. This work considered the effect of x-ray quantum noise. To extend this work to other 3-D imaging techniques, and to consider additional effects, such as visual disparity and depth perception, we developed an extensive 3-D computer simulation of the breast. This work in turn, has led to efforts in characterizing breast tissue based upon breast ductal branching.

6. References

1. H.P. Chan, M.M. Goodsitt, J.M. Sullivan, K.L. Darner and L.M. Hadjiiski. "Depth perception in digital stereoscopic mammography", DOD Era of Hope, 242 (2000).
2. D.J. Getty, R.M. Pickett, J.A. Swets, C.J. D'Orsi, A. Karallas. "Use of stereoscopic digital mammography to improve early detection and diagnosis of breast lesions", DOD Era of Hope, 248 (2000).
3. L.M. Hamberg, L.T. Niklason, V. Venkatakrishnan, M. Rosol, R. Moore, and D.B. Kopans. "Tomosynthesis breast imaging", DOD Era of Hope, 197 (2000).
4. A.D.A. Maidment, M. Albert, and E.P. Conant. Three-Dimensional Imaging of Breast Calcifications. In *Exploiting New Image Sources and Sensors*. Proceedings of the SPIE, 3240, 200-208 (1997).
5. A.D.A. Maidment, M. Albert, E.F. Conant, and S.A. Feig. Three-Dimensional Visualization of Breast Cancer. In *Digital Mammography '98*, edited by N. Karssemeijer, M. Thijssen, J. Hendricks, and L. van Erning, Kluvier, Holland, 57-60, (1998).
6. A.D.A. Maidment, and M. Albert. "Automated Reconstruction of 3-D Calcifications", In *Digital Mammography 2000*. In press.
7. R. Ning, B. Chen, D.L. Conover, and R. Yu. "Flat-panel detector-based cone beam volume CT mammography imaging: Preliminary phantom study". *Physics of Medical Imaging, 2001*, Proceeding of the SPIE, Bellingham WA, In press.
8. Michael Albert, and Andrew D.A. Maidment. Linear Response Theory for Detectors Consisting of Discrete Arrays. *Medical Physics*, 27(10), 2417-2434, October 2000.
9. A.D.A. Maidment and M.J. Yaffe. Analysis of signal propagation in optically-coupled detectors for digital mammography: I. Phosphor Screens. *Phys. Med. Biol.*, 40, 877-889 (1995).
10. A.D.A. Maidment and M.J. Yaffe. Analysis of signal propagation in optically-coupled detectors for digital mammography: II. Lens and fibre optics. *Phys. Med. Biol.*, 41, 475-493 (1996).

7. Appendices

Copies of the following manuscripts are provided:

- Reprint: "Linear Response Theory for Detectors Consisting of Discrete Arrays"
Medical Physics, **27**(10), 2417-2434, October 2000 A-1
- Reprint: "Mammogram synthesis using a 3-D simulation. I. Breast tissue model
and the exam simulation", Medical Physics, **29**(9), 2131-2139, September 2002 A-2
- Reprint: "Mammogram synthesis using a 3-D simulation. II. Evaluation of
synthetic mammogram texture", Medical Physics, **29**(9), 2140-2151, September
2002 A-3
- Preprint: "Classification of Galactograms using Ramification Matrices:
Preliminary Results". Academic Radiology, 10(2), In Press, February 2003 A-4
- Preprint: Effects of quantum noise on dose and contrast sensitivity in
stereoradiography. Submitted to Medical Physics, September 18, 2002..... A-5

Reprinted from

Medical Physics

AVAILABLE ONLINE—See <http://www.medphys.org>

October 2000

Volume 27, Number 10

Linear response theory for detectors consisting of discrete arrays

Michael Albert and Andrew D. A. Maidment

*Thomas Jefferson University, Department of Radiology, Suite 3390, Gibbon Building,
111 South 11th Street, Philadelphia, Pennsylvania 19107-5563*

pp. 2417-2434

Linear response theory for detectors consisting of discrete arrays

Michael Albert and Andrew D. A. Maidment^{a)}

Thomas Jefferson University, Department of Radiology, Suite 3390, Gibbon Building,
111 South 11th Street, Philadelphia, Pennsylvania 19107-5563

(Received 17 March 2000; accepted for publication 5 May 2000)

The optical transfer function (OTF) and the noise power or Wiener spectrum are defined for detectors consisting of a lattice of discrete elements with the assumptions of linear response, Gaussian statistics, and stationarity under the discrete group of translations which leave the lattice fixed. For the idealized classification task of determining the presence or absence of a signal under signal known exactly/background known exactly (SKE/BKE) conditions, the Wiener spectrum, the OTF, along with an analog of the gray-scale transfer characteristic, determine the signal-to-noise ratio (SNR), which quantifies the ability of an ideal observer to perform this task. While this result is similar to the established result for continuous detectors, such as screen-film systems, the theory of discrete lattices of detectors must take into account the fact that the lattice only supports a bounded but (in the limit of a detector of arbitrarily great extent) continuous range of frequencies. Incident signals with higher spatial frequencies appear in the data at lower aliased frequencies, and there are pairs of signals which are not distinguishable by the detector (the SNR vanishes for the task of distinguishing such signals). Further, the SNR will in general change if the signal is spatially displaced by a fraction of the lattice spacing, although this change will be small for objects larger than a single pixel. Some of the trade-offs involved in detectors of this sort, particularly in dealing with signal frequencies above those supported by the lattice, are studied in a simple model.
© 2000 American Association of Physicists in Medicine. [S0094-2405(00)00908-1]

Key words: image theory, MTF, DQE, Wiener spectrum, digital detectors

I. INTRODUCTION

The importance of signal detection theory in quantifying the performance of medical imaging systems (x-ray screen-film imaging being perhaps the best example) gives impetus to applying the same techniques to the digital radiographic imaging systems which are now coming into clinical use. As applied to screen-film systems, signal detection theory requires three assumptions to be at least approximately fulfilled: that the detector responds linearly to the incoming signal, and is both stationary and homogeneous (i.e., both the detector response and the additive noise are translationally invariant). One can then summarize the response of the system in terms of the gray-scale transfer characteristic, the optical transfer function (OTF), and the noise power or Wiener spectrum.

The digital x-ray imaging systems which are now appearing generally behave as a lattice of discrete detector elements. Although digital, these detectors are generally operated under conditions such that the effects of quantization are negligible. When compared to screen-film systems, these detectors tend to be linear over a wider range of exposures. Like screen-film, for low-contrast signals the noise is approximately additive and Gaussian. However, as the size of the imaging elements is now comparable to the size of some of the smaller objects which are of clinical interest (around 0.1 mm), these detectors are not strictly homogeneous in that translations by a fraction of the lattice spacing result in the signal being recorded in a different manner. As these devices generally consist of a regular lattice of sensitive elements, they still possess a symmetry with respect to a discrete group

of translations. This symmetry is approximate due to the finite extent of physical detectors. However, as in the theory of screen-film systems, corrections for the limited extent of the detector are negligible for many practical applications. Thus, one can apply Fourier techniques to put the signal detection theory of such devices in a form which is both tractable and similar to the theory of screen-film systems. Instead of using a continuous Fourier transform, one uses a discrete space Fourier transform, which recodes the data acquired by the detector at a discrete lattice of positions in terms of a bounded and continuous range of spatial frequencies.

For screen-film systems, the OTF diagonalizes the linear operator which relates the input signal to the output. As detailed below, for discrete-array detectors the effects of aliasing introduce a null space, different for each device, which prevents this operator from being diagonalized using a basis common to all devices, but the OTF represents the operator in a basis in which it is sparse in the sense that all terms vanish except those between input and output spatial frequencies which are equal or aliased. The Wiener spectrum is the discrete space Fourier transform of the discrete autocovariance function, and thus is also defined in the region of frequency space which the lattice supports. As in the case of continuous detectors, for low-contrast objects (so that responses are approximately linear), these quantities determine the signal-to-noise ratio (SNR) which is an appropriate figure-of-merit for the classification task of discriminating between the presence or absence of an exactly known signal against an exactly known background (SKE/BKE).

To make notation definite, it is necessary to review the relevant parts of signal detection theory for screen-film imaging systems (Sec. II) and the relevant Fourier techniques (Sec. III). Subsequently, the OTF (Sec. IV) and Wiener spectrum (Sec. V) of discrete detectors can be studied leading up to the calculation of SNR for the case of SKE/BKE (Sec. VI).

As discussed below, the effects of aliasing on the interpretation of the OTF have been noted in the literature, and the definition of the Wiener spectrum given here has appeared before. However, this paper presents a systematic theory of signal detection for discrete-array x-ray detectors. The approach here differs from the more general theoretical approach of cross-talk matrices¹ in that the work reported here uses the additional assumptions of infinite extent, Gaussian statistics, and discrete translational symmetry. There are many imaging systems for which these assumptions are not appropriate [e.g., three-dimensional (3D) tomographic reconstruction²]. However, the work presented here has certain advantages in that so long as the additional assumptions are approximately true, the quantities involved are closely related to those used with screen-film systems and are similar or identical to measured quantities relating to digital systems which have appeared in the literature.

To demonstrate the use of this theoretical structure and to investigate some of the trade-offs inherent in discrete-array systems, Sec. VII presents a simple model of a detector. In particular, this gives the opportunity to investigate how the detector's response to high spatial-frequency signals affects the detection of objects in terms of SNR, and in particular the effect which is sometimes called "noise aliasing" is addressed.

II. REVIEW

The theory of SKE/BKE detection and classification for screen-film-like systems has been expounded in detail,³⁻⁷ and is reviewed here in order to establish notation for later comparison with discrete-array detectors. The input signal is the x-ray intensity per unit area and the output signal is the film density, both as a function of position. The interesting and tractable case is the search for low-contrast variations $I(\mathbf{r})$ in an x-ray beam whose baseline intensity, I_o , is such that the changes in film density $D(\mathbf{r})$ are a linear function of $I(\mathbf{r})$. The additional assumption of translational invariance then gives

$$\langle D(\mathbf{r}) \rangle = \frac{\gamma(\log_{10} e)}{I_o} \int \int d^2\mathbf{r}' P(\mathbf{r}-\mathbf{r}') \langle I(\mathbf{r}') \rangle, \quad (1)$$

where $P(\mathbf{r}-\mathbf{r}')$, the point spread function (PSF), is the density increase of the film at position \mathbf{r} due to a given x-ray intensity at \mathbf{r}' . The brackets $\langle \rangle$ represent ensemble averages, i.e., averages over many exposures. Since $I(\mathbf{r})$ and $D(\mathbf{r})$ are here defined as variations relative to baseline values, $\langle I(\mathbf{r}) \rangle = 0$ and $\langle D(\mathbf{r}) \rangle = 0$ in the absence of a signal.

Because the PSF is translationally invariant, the convolution operator is diagonalized in frequency space, giving

$$\langle \hat{D}(\mathbf{f}) \rangle = \frac{\gamma(\log_{10} e)}{I_o} T(\mathbf{f}) \langle \hat{I}(\mathbf{f}) \rangle, \quad (2)$$

where \mathbf{f} represents a two-dimensional vector in frequency space and T , the optical transfer function (OTF), is the Fourier transform of the PSF. The function $\hat{D}(\mathbf{f})$ is the Fourier transform of the data $D(\mathbf{r})$, following the convention that for any suitable⁸ function g ,

$$\hat{g}(\mathbf{f}) = \int \int d^2\mathbf{r} g(\mathbf{r}) e^{-2\pi i \mathbf{r} \cdot \mathbf{f}},$$

$$g(\mathbf{r}) = \int \int d^2\mathbf{f} \hat{g}(\mathbf{f}) e^{2\pi i \mathbf{r} \cdot \mathbf{f}}, \quad (3)$$

so that \mathbf{f} is in units of cycles per unit length. The factor of $\gamma(\log_{10} e)/I_o$ serves to convert units of x-ray beam intensity into units of change of film density in the region of linear response, allowing the normalization $T(\mathbf{0}) = 1$.

Realizations of the imaging process will be subject to noise which can be characterized by the autocovariance function

$$C(\mathbf{r}_1, \mathbf{r}_2) = C(\mathbf{r}_2, \mathbf{r}_1) = \langle D(\mathbf{r}_1) D(\mathbf{r}_2) \rangle, \quad (4)$$

that, for Gaussian noise, completely determines the statistical nature of the noise process. For stationary processes, the autocovariance function depends only upon the displacement,

$$C(\mathbf{r}_1, \mathbf{r}_2) = C(\mathbf{r}_2 - \mathbf{r}_1), \quad (5)$$

so that the autocovariance $C(\mathbf{r})$ is now a function of a single vector, the displacement \mathbf{r} . The Wiener spectrum is the Fourier transform of the autocovariance function, and

$$W(\mathbf{f}) = \lim_{|A| \rightarrow \infty} \frac{1}{|A|} \left\langle \left| \int \int_A d^2\mathbf{r} D(\mathbf{r}) e^{-2\pi i \mathbf{r} \cdot \mathbf{f}} \right|^2 \right\rangle \quad (6)$$

shows that the Wiener spectrum can be estimated in terms of the Fourier components of signal-free ("flat-field") images over regions A of sufficiently large area $|A|$.

For Gaussian noise it can be shown⁹ that the optimal strategy for SKE/BKE signal detection or classification consists of choosing a mask function $g(\mathbf{r})$ and a cutoff value for the statistic

$$\theta_g = \int \int d^2\mathbf{r} g(\mathbf{r}) D(\mathbf{r}). \quad (7)$$

The efficacy of θ_g for discriminating between hypothesis I (e.g., signal absent) and hypothesis II (e.g., signal present) is measured by the signal-to-noise ratio

$$\text{SNR}_g^2 = \frac{(\langle \theta_g \rangle_I - \langle \theta_g \rangle_{II})^2}{\text{Var}(\theta_g)}, \quad (8)$$

where the numerator is the difference between the expectation values of θ_g under the two hypotheses and the denominator is the variance in the statistic θ_g , which for additive noise is independent of the hypothesis.

While only real-valued functions $g(\mathbf{r})$ are needed for calculating decision statistics, it will be useful to extend the definition of θ_g to complex valued $g(\mathbf{r})$, in which

case the variance of θ_g is the sum of the variances of the real and imaginary parts. The variance of the statistic θ_g is given by

$$\text{Var}(\theta_g) = \langle (\theta_g - \langle \theta_g \rangle)(\theta_g - \langle \theta_g \rangle)^* \rangle \tag{9}$$

$$= \int \int d^2\mathbf{r} \int \int d^2\mathbf{r}' g(\mathbf{r}) C(\mathbf{r}, \mathbf{r}') g(\mathbf{r}')^* \tag{10}$$

$$= \int \int d^2\mathbf{f} \hat{g}(\mathbf{f}) \hat{g}^*(\mathbf{f}) W(\mathbf{f}), \tag{11}$$

as can be seen by substitution of Eqs. (7) and (4) into Eq. (9) [indeed, Eq. (10) can be taken as the definition of the auto-covariance function]. It can be shown, for example using the Schwarz inequality,^{10,11} that the optimal choice of mask function is given by

$$\hat{g}_{\mathcal{I}}(\mathbf{f}) = \frac{\langle \hat{I}(\mathbf{f}) \rangle_{\Pi} - \langle \hat{I}(\mathbf{f}) \rangle_{\mathcal{I}} T(\mathbf{f})}{W(\mathbf{f})}, \tag{12}$$

for which the SNR is given by

$$\text{SNR}_{\mathcal{I}}^2 = \int \int d^2\mathbf{f} \frac{\gamma^2 (\log_{10} e)^2}{I_o^2} \frac{|\langle \hat{I}(\mathbf{f}) \rangle_{\Pi} - \langle \hat{I}(\mathbf{f}) \rangle_{\mathcal{I}}|^2 |T(\mathbf{f})|^2}{W(\mathbf{f})}, \tag{13}$$

where the subscript \mathcal{I} indicates that this represents the optimal or ideal⁷ observer given the detector and task at hand.

Returning momentarily to the task of estimating the Wiener spectrum from flat-field images, if in Eq. (9) one sets $g(\mathbf{r}) = G(\mathbf{r}) e^{2\pi i \mathbf{f}_o \cdot \mathbf{r}}$, where $G(\mathbf{r})$ is a window function with normalization

$$\int \int d^2\mathbf{r} G^2(\mathbf{r}) = 1, \quad \int \int d^2\mathbf{f} |\hat{G}(\mathbf{f})|^2 = 1, \tag{14}$$

then calculating $\langle \theta_g \theta_g^* \rangle$ by Eq. (11) one obtains

$$\int \int d^2\mathbf{f} |\hat{G}(\mathbf{f} - \mathbf{f}_o)|^2 W(\mathbf{f}) = \left\langle \left| \int \int d^2\mathbf{r} G(\mathbf{r}) e^{-2\pi i \mathbf{f}_o \cdot \mathbf{r}} D(\mathbf{r}) \right|^2 \right\rangle, \tag{15}$$

which, since $|\hat{G}(\mathbf{f} - \mathbf{f}_o)|^2$ will be sharply peaked near \mathbf{f}_o , shows that for finite length data sets one actually estimates the Wiener spectrum convolved with the square of the Fourier transform of the window function. In particular, for a rect window so that G is chosen to vanish outside of a square region of area $|A| = L^2$ and to have value $1/\sqrt{|A|}$ inside that region,

$$|\hat{G}(\mathbf{f})|^2 = A \left(\frac{\sin(\pi L f_x) \sin(\pi L f_y)}{\pi^2 L^2 f_x f_y} \right)^2 = A \text{sinc}^2(L f_x) \text{sinc}^2(L f_y), \tag{16}$$

where f_x, f_y are the components of \mathbf{f} . For large areas, this becomes increasingly like a delta-function, giving Eq. (6).

III. MATHEMATICAL PRELIMINARIES

In the case of screen-film, described above, we studied a mapping of functions defined for all spatial positions to func-

tions defined for all frequencies, namely the Fourier transform defined by Eq. (3). For the digital x-ray detectors of interest in this paper, the input is still a continuous distribution of x-rays, but the output signal consists of data with values assigned only at a discrete set of lattice points. The size of the array is assumed to be sufficiently large so that boundary effects play no part, and thus is treated as being of infinite extent. To analyze these data it is appropriate to use a Fourier technique based on the discrete translational symmetry of the detectors. Mathematically, this transform is similar to the Fourier series, but with the roles of the space and frequency domains reversed.¹² Following Giger,¹³ this is called the ‘‘discrete’’ space Fourier transform (DFT). The ‘‘finite’’ Fourier transform (FFT)¹⁴ is the Fourier technique applied to finite sequences of data points that is customarily implemented using an algorithm known as the ‘‘fast Fourier transform.’’ For practical purposes, one always deals with finite data sets, and the discrete space Fourier transform is a limiting case of the finite Fourier transform. As the number of equally spaced data points used in calculating a finite Fourier transform increases, the discrete set of frequencies calculated fill more and more densely a bounded region of frequency space, so that in the limit one obtains a function of a continuous range of frequencies. The function obtained by this limiting process is the discrete space Fourier transform of the spatial data.

To deal with the two-dimensional arrangements of sensitive elements which are of interest, it will be convenient to introduce the ideas of vectors generating a lattice and of dual basis vectors. A two-dimensional lattice of points can be specified by vectors \mathbf{v}_1 and \mathbf{v}_2 such that every point in the lattice can be represented as

$$\mathbf{r}_{m_1, m_2} = m_1 \mathbf{v}_1 + m_2 \mathbf{v}_2, \tag{17}$$

where m_1 and m_2 are integers. The vectors \mathbf{v}_1 and \mathbf{v}_2 are said to generate the lattice, but the choice of vectors for a given lattice is not unique. For the common case of a square grid the choice of \mathbf{v}_1 as lying along the x -axis and \mathbf{v}_2 as lying along the y -axis is natural. The plane containing the lattice can be tiled in such a way that each tile contains a total of one lattice point. Each tile is then called a ‘‘unit cell.’’ For the case of a square grid of detectors with spacing a , the most natural choice of a unit cell would be the square centered at the coordinate origin extending to $\pm a/2$ along both axes. A small region of a plane containing a square lattice and one of the unit cells is drawn in Fig. 1(a). The reciprocal vectors denoted by \mathbf{w}_1 and \mathbf{w}_2 are defined by the requirements

$$\mathbf{v}_i \cdot \mathbf{w}_j = \delta_{ij} = \begin{cases} 1: i=j \\ 0: i \neq j \end{cases}, \tag{18}$$

and serve as a basis for frequency space and as generators of the reciprocal lattice. In the case of the rectangular grid mentioned above, each \mathbf{w}_i would be parallel to \mathbf{v}_i and scaled appropriately as illustrated in Fig. 1(b), which also shows a unit cell of the reciprocal lattice. To help clarify these ideas, Fig. 1(c) shows a hexagonal lattice with two choices of the

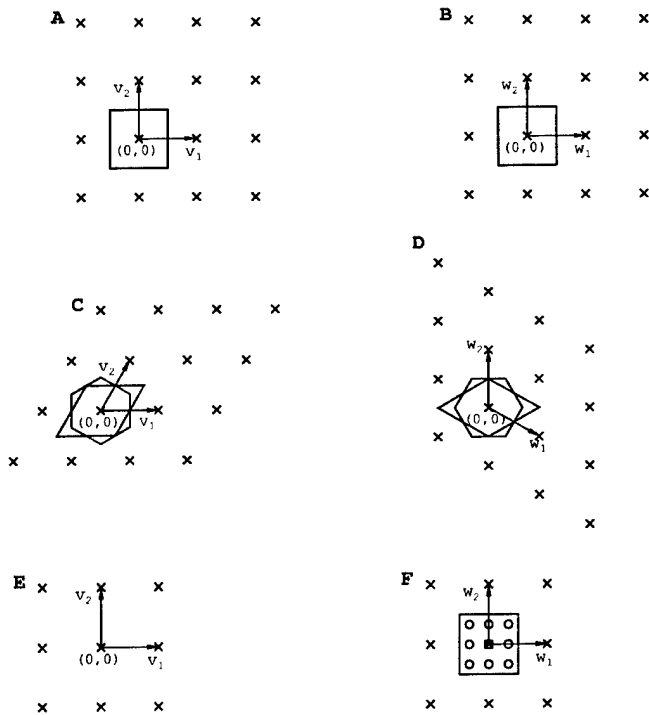


FIG. 1. (a) a rectangular lattice. (b) The reciprocal lattice of (a). (c) A hexagonal lattice. (d) the reciprocal lattice of (c). Note that (a), (b), (c), and (d) represent a finite region of a lattice which covers the entire plane. (e) A 3×3 finite rectangular lattice. (f) The circles represent the frequencies used in the finite Fourier transform of (e). For comparison, a unit cell of the full reciprocal lattice is shown. See Sec. III for details.

unit cell (parallelogram or hexagon) and Fig. 1(d) shows the reciprocal lattice (note that \mathbf{v}_1 is perpendicular to \mathbf{w}_2 and \mathbf{v}_2 is perpendicular to \mathbf{w}_1). The area $|A| = |\mathbf{v}_1 \times \mathbf{v}_2|$ of a unit cell is independent of the choice of unit cell, since it is fixed by the average density of lattice points over large regions. The area of the unit cell of the reciprocal lattice, $|K| = |\mathbf{w}_1 \times \mathbf{w}_2|$, is inversely proportional to $|A|$, as can be seen by

$$\begin{aligned}
 |A||K| &= \left| \det \begin{pmatrix} (\mathbf{v}_1)_x & (\mathbf{v}_1)_y \\ (\mathbf{v}_2)_x & (\mathbf{v}_2)_y \end{pmatrix} \det \begin{pmatrix} (\mathbf{w}_1)_x & (\mathbf{w}_2)_x \\ (\mathbf{w}_1)_y & (\mathbf{w}_2)_y \end{pmatrix} \right| & (19) \\
 &= \left| \det \begin{pmatrix} \mathbf{v}_1 \cdot \mathbf{w}_1 & \mathbf{v}_1 \cdot \mathbf{w}_2 \\ \mathbf{v}_2 \cdot \mathbf{w}_1 & \mathbf{v}_2 \cdot \mathbf{w}_2 \end{pmatrix} \right| \\
 &= \left| \det \begin{pmatrix} 1 & 0 \\ 0 & 1 \end{pmatrix} \right| = 1, & (20)
 \end{aligned}$$

making use of the fact that the determinant of a product of matrices is equal to the product of the determinants and Eq. (18).

For any function $g(m_1, m_2)$ of the lattice, the discrete space Fourier transform is defined^{12,13} as

$$\hat{g}(\mathbf{f}) = |A| \sum_{m_1, m_2} g(m_1, m_2) e^{-2\pi i \mathbf{r}_{m_1, m_2} \cdot \mathbf{f}} \quad (21)$$

for all spatial frequencies \mathbf{f} . This definition is equivalent to evaluating the z -transform on the unit circle in the complex plane.^{12,15} It is also equivalent to the Fourier transform of the function obtained from the data set by interpolation with

sinc functions (e.g., Ref. 16, p. 230). Direct calculation from Eq. (21) gives

$$\hat{g}(\mathbf{f}) = \hat{g}(\mathbf{f} + m_1 \mathbf{w}_1 + m_2 \mathbf{w}_2), \quad (22)$$

which shows that \hat{g} is periodic in Fourier space for displacements in the dual lattice and one need only consider values of \hat{g} on one unit cell of this lattice. Any frequency \mathbf{f} outside of this unit cell is an alias of a frequency \mathbf{f}' inside the cell, with $\mathbf{f} - \mathbf{f}'$ in the reciprocal lattice. Viewed another way, the reciprocal lattice divides points in the frequency plane into equivalence classes of points, two points being equivalent if and only if they are separated by a vector in the reciprocal lattice. Any unit cell will contain exactly one point from each equivalence class (except for boundaries), and knowledge of \hat{g} on the unit cell determines \hat{g} on the entire plane. Alternatively, one can consider \hat{g} as being defined on the topological ‘‘quotient space,’’ a torus, just as one can consider a function on the real line with period 2π as defined on the unit circle (Ref. 17, p. 155).

The exponential functions in the discrete Fourier transformation satisfy a simple orthogonality condition

$$\iint_K d^2 \mathbf{f} e^{-2\pi i \mathbf{f} \cdot \mathbf{r}_{m_1, m_2}} e^{2\pi i \mathbf{f} \cdot \mathbf{r}_{n_1, n_2}} = |K| \delta_{m_1, n_1} \delta_{m_2, n_2}, \quad (23)$$

where K is the region corresponding to the unit cell of the reciprocal lattice in the frequency plane and $|K|$ is the area of this region, thus giving

$$g(m_1, m_2) = \iint_K d^2 \mathbf{f} \hat{g}(\mathbf{f}) e^{2\pi i \mathbf{f} \cdot \mathbf{r}_{m_1, m_2}} \quad (24)$$

as the inverse transform. The complex exponentials form a complete set of orthogonal functions, so that any appropriate periodic function of frequency \mathbf{f} can be represented in terms of them. The completeness can also be expressed in terms of a comb function as

$$\sum_{m_1, m_2} e^{2\pi i (\mathbf{f} - \mathbf{f}') \cdot \mathbf{r}_{m_1, m_2}} = |K| \sum_{k_1, k_2} \delta(\mathbf{f} - \mathbf{f}' - \mathbf{f}_{k_1, k_2}), \quad (25)$$

where the equality is interpreted in terms of distributions and the sum on the right-hand side is over the frequencies in the reciprocal lattice.^{8,16,17}

For actual finite data sets, one applies the finite Fourier transformation. The discrete space Fourier transformation can be interpreted as a limit of the finite Fourier transformation as the number of equally spaced points in the data set is increased. Specifically, consider a bounded subset of the $\{\mathbf{r}_{n_1, n_2}\}$ such as \mathcal{R} of the form

$$\mathcal{R} = \{\mathbf{r}_{n_1, n_2} | N_1 \leq n_1 < N'_1, N_2 \leq n_2 < N'_2\}, \quad (26)$$

for which the finite Fourier transform and its inverse are given by

$$\hat{g}(l_1, l_2) = \sum_{\mathbf{r}_{n_1, n_2} \in \mathcal{R}} g(n_1, n_2) e^{-2\pi i \mathbf{f}_{l_1, l_2} \cdot \mathbf{r}_{n_1, n_2}}, \quad (27)$$

$$g(n_1, n_2) = \frac{1}{\Delta N_1 \Delta N_2} \sum_{\mathbf{f}_{l_1, l_2} \in \mathcal{R}} \hat{g}(l_1, l_2) e^{2\pi i \mathbf{f}_{l_1, l_2} \cdot \mathbf{r}_{n_1, n_2}}, \quad (28)$$

where $\Delta N_i = N'_i - N_i$. The points in the Fourier space are given by

$$\mathbf{f}_{l_1, l_2} = \frac{l_1}{\Delta N_1} \mathbf{w}_1 + \frac{l_2}{\Delta N_2} \mathbf{w}_2 \quad (29)$$

and

$$\mathcal{R} = \{\mathbf{f}_{l_1, l_2} | L_1 \leq l_1 < L'_1, L_2 \leq l_2 < L'_2\}, \quad (30)$$

where the L 's are chosen so that $L'_i - L_i = N'_i - N_i$. The reciprocal relationship [Eq. (18)] between the basis vectors $\{\mathbf{v}_i\}$ and the dual basis vectors $\{\mathbf{w}_i\}$ gives

$$\begin{aligned} \mathbf{f}_{l_1, l_2} \cdot \mathbf{r}_{n_1, n_2} &= \left(\frac{l_1}{\Delta N_1} \mathbf{w}_1 + \frac{l_2}{\Delta N_2} \mathbf{w}_2 \right) \cdot (n_1 \mathbf{v}_1 + n_2 \mathbf{v}_2) \\ &= \frac{l_1 n_1}{\Delta N_1} + \frac{l_2 n_2}{\Delta N_2}, \end{aligned} \quad (31)$$

which, along with choosing $N'_i = -N_i = N_o/2$ and $L_i = -L'_i = N_o/2$ for N_o even, produces a more conventional representation of the finite Fourier transform.

As the number of data points $\Delta N_1 \Delta N_2$ increases, the spacing between the frequencies \mathbf{f}_{l_1, l_2} decreases, so that in the limit the data points on the lattice extend across the entire plane and the frequency values fill a unit cell of the reciprocal lattice. The finite sum in the FFT [Eq. (27)] approximates (with a factor of $|A|$) the infinite sum in the DFT [Eq. (21)], and for the inverse transform the sum in Eq. (28) (with the introduction of a factor of $|A||K|=1$) becomes

$$\begin{aligned} g_{\text{FFT}}(n_1, n_2) &= \sum_{\mathbf{f}_{l_1, l_2} \in \mathcal{R}} \frac{|K|}{\Delta N_1 \Delta N_2} (|A| \hat{g}_{\text{FFT}}(l_1, l_2)) \\ &\quad \times e^{2\pi i \mathbf{f}_{l_1, l_2} \cdot \mathbf{r}_{n_1, n_2}}, \end{aligned} \quad (32)$$

which approximates the integral used in the inversion of the discrete space Fourier transform, Eq. (24). To illustrate this concept, Fig. 1(e) shows a small rectangular lattice (corresponding to $N_i = -1, N'_i = 2$). The circles in Fig. 1(f) represent the corresponding frequency vectors for use with the finite Fourier transform. The box shows the region which would correspond to a unit cell of the reciprocal lattice if the lattice in Fig. 1(e) were extended to an infinite lattice. If the finite lattice shown in Fig. 1(e) were extended (but still finite), the corresponding frequency vectors of the finite Fourier transform would fill the unit cell more and more densely.

It should be noted that if ΔN_1 or ΔN_2 are even, then some of the frequencies at which the finite Fourier transform is defined [shown as the circles in Fig. 1(f)] would lie on the boundary of the unit cell, and such frequencies would have aliases which also lie on the boundary. For example, in the square lattice considered in Fig. 1(f), if one of the frequencies at which the finite Fourier transform is defined fell on the edge of the unit cell, an alias of that frequency would lie on the opposite edge, and a frequency on any corner would be aliased with all of the other corners. In certain sums over frequency components, such as Eq. (28), it is useful to adopt the convention that such sums include exactly one representative from each class of aliased frequencies, so that frequencies falling on the boundary of the unit cell are not counted multiple times. If one uses the "quotient space" point of

view, this follows automatically as the aliases correspond to a single point in the quotient space. Alternatively, one might weigh each frequency by a factor (1/2 for frequencies lying on edges and 1/4 for corners) so that each class of aliased frequencies has a total weight of 1 (similar to counting fractional atoms when reckoning the number of atoms in a unit cell of a crystal).

The results pertaining to Fourier transformations and dual lattices which are reviewed in this section have direct generalizations to any number of dimensions, but as the statement of the results for arbitrary finite dimension would be notationally cumbersome, only the two-dimensional results have been explicitly stated. For notational convenience, let \mathbf{m} represent the ordered pair m_1, m_2 , so that $g(\mathbf{m}) = g(m_1, m_2)$ and $\mathbf{r}_m = \mathbf{r}_{m_1, m_2}$, and similarly for \mathbf{k} , e.g., $\mathbf{f}_k = \mathbf{f}_{k_1, k_2}$.

IV. TRANSFER FUNCTION

The analog of the optical transfer function, which relates the response of the detector to the input signal in frequency space, can now be defined. The input signal $\langle I \rangle$ is a continuous function of the plane. As $\langle I \rangle$ is defined relative to the "flat-field," it is reasonable to assume that $\langle I \rangle$ has compact support, or at least vanishes sufficiently quickly at infinity to leave the quantities considered here well defined. Thus the Fourier transform $\langle \hat{I} \rangle$ is a continuous function of the entire frequency plane. The data $D(\mathbf{r}_m)$ are well-defined only at the discrete lattice points \mathbf{r}_m , so that the discrete space Fourier transform $\langle \hat{D}(\mathbf{f}) \rangle$ is determined by its values in one unit cell of the reciprocal lattice. Values of $\langle \hat{D} \rangle$ outside of the first unit cell are determined by the periodicity relative to the reciprocal lattice and contain no new information. For spatial frequencies inside the first unit cell, the detector responds at the same frequency as the input signal. For frequencies outside of the first unit cell, the detector responds at an aliased frequency, so it is impossible to uniquely determine the input signal without additional information, although it will be argued in later sections that for reasonable tasks this is not a significant problem.

Each point on the detector grid is assumed to respond linearly to the incident signal, so that the analog of Eq. (1) is

$$\langle D(\mathbf{r}_m) \rangle = \Gamma \iint d^2 \mathbf{r}' P(\mathbf{r}_m, \mathbf{r}') \langle I(\mathbf{r}') \rangle, \quad (33)$$

where P , the analog of the point spread function, represents the response of the detector at \mathbf{r}_m to x-ray light incident at \mathbf{r}' , and Γ is a constant for converting x-ray intensity into digital values, generally chosen so that the integral of P with respect to \mathbf{r}' is unity. With a discrete detector, one no longer has full translational invariance, but there remains an invariance under translations which take lattice points to lattice points, assuming that each pixel is identical except for position. Thus we can write

$$P(\mathbf{r}_m, \mathbf{r}') = P(\mathbf{r}_m - \mathbf{r}'), \quad (34)$$

to indicate that the response of a detector element to an input signal depends upon the displacement of the detector ele-

ment from the region to which the signal is applied, but not upon the absolute position of the detector element or the signal, from which it follows^{18,19} that

$$\langle D(\mathbf{r}_m) \rangle = \Gamma \int \int d^2 \mathbf{r}' P(\mathbf{r}_m - \mathbf{r}') \langle I(\mathbf{r}') \rangle \quad (35)$$

for each position \mathbf{r}_m of the sensitive elements on the lattice. While the data $D(\mathbf{r}_m)$ are only available at the lattice points, the convolution can be calculated at any point, so that

$$\mathcal{D}(\mathbf{r}) = \Gamma \int \int d^2 \mathbf{r}' P(\mathbf{r} - \mathbf{r}') \langle I(\mathbf{r}') \rangle, \quad (36)$$

$$\hat{\mathcal{D}}(\mathbf{f}) = \Gamma \hat{P}(\mathbf{f}) \langle \hat{I}(\mathbf{f}) \rangle, \quad (37)$$

serves as a definition of $\mathcal{D}(\mathbf{r})$ for any position \mathbf{r} . Although $\mathcal{D}(\mathbf{r})$ is equal to the data $\langle D(\mathbf{r}_m) \rangle$ at the lattice points where $\mathbf{r} = \mathbf{r}_m$, at other points $\mathcal{D}(\mathbf{r})$ is an interpolation which will not in general represent a physical quantity, although it is sometimes useful to think of $\mathcal{D}(\mathbf{r})$ as the response of a virtual sensitive element added to the detector at position \mathbf{r} in such a manner as to not perturb or be perturbed by the other elements. The discrete space Fourier transform on $\langle D(\mathbf{r}_m) \rangle$ can now be calculated using $\langle D(\mathbf{r}_m) \rangle = \mathcal{D}(\mathbf{r}_m)$ for $g(\mathbf{r}_m)$ in Eq. (21), giving

$$\begin{aligned} \langle \hat{D}(\mathbf{f}) \rangle &= |A| \sum_m e^{-2\pi i \mathbf{r}_m \cdot \mathbf{f}} \mathcal{D}(\mathbf{r}_m) \\ &= |A| \sum_m \int \int_K d^2 \mathbf{r}' \hat{\mathcal{D}}(\mathbf{r}') e^{2\pi i \mathbf{r}_m \cdot (\mathbf{r}' - \mathbf{f})} \\ &= \sum_{\mathbf{f}_k} \hat{\mathcal{D}}(\mathbf{f} + \mathbf{f}_k) = \Gamma \sum_{\mathbf{f}_k} T(\mathbf{f} + \mathbf{f}_k) \langle \hat{I}(\mathbf{f} + \mathbf{f}_k) \rangle, \end{aligned} \quad (38)$$

which follows from expressing \mathcal{D} in terms of its Fourier transform and using the completeness relationship expressed in Eq. (25).

Comparison of Eq. (38) with its screen-film analog, Eq. (2), helps to clarify the interpretation of the OTF, $T(\mathbf{f})$. The spacings in the discrete lattice introduce new length scales which occur explicitly in the summation over aliases. In the limit of a very finely grained lattice, so that $|A| \rightarrow 0$, the spacing of the reciprocal lattice points gets larger, until only the one unaliased term contributes significantly to Eq. (38), and the screen-film case is recovered.

When frequencies higher than those supported by the lattice are present in the signal, the summation in Eq. (38) introduces "aliasing," that is, there exist multiple spatial input frequencies whose output is at the same frequency and are thus not distinguishable. For example, considering a one-dimensional lattice with pixel-pitch of 1 cm, oscillations at a rate of 0.5 cycles per cm can not be distinguished from oscillations at a rate of 1.5 cycles per cm. From Eq. (38), two components of the input signal generate the same component of the output signal if and only if their spatial frequencies differ by an element \mathbf{f}_{k_1, k_2} of the reciprocal lattice.

More generally for any lattice there are frequencies \mathbf{f}_o such that $-\mathbf{f}_o$ is an alias of \mathbf{f}_o (for example, if \mathbf{f} and $-\mathbf{f}$ are on opposite boundaries of the first unit cell in the reciprocal

lattice). For such a frequency \mathbf{f}_o [noting that $T(\mathbf{f}) = T^*(-\mathbf{f})$ and $\langle \hat{I}(\mathbf{f}) \rangle = \langle \hat{I}^*(-\mathbf{f}) \rangle$ for real-valued $P(\mathbf{r})$ and $\langle I(\mathbf{r}) \rangle$] it is possible to choose the phase of $\langle \hat{I}(\mathbf{f}_o) \rangle$ so that

$$T(\mathbf{f}_o) \langle \hat{I}(\mathbf{f}_o) \rangle + T(-\mathbf{f}_o) \langle \hat{I}(-\mathbf{f}_o) \rangle = 0, \quad (39)$$

showing by Eq. (38) that a sinusoidal signal concentrated at frequency \mathbf{f}_o and displaced by an appropriate offset relative to the lattice (as determined by the phase of $\langle I(\mathbf{f}_o) \rangle$) would be indistinguishable from the flat-field signal. Returning to the simple one-dimensional model of pixels spaced at 1 cm, this result means that for some displacement relative to the lattice the input of a sinusoidal wave of frequency 1 cycle/cm would give vanishing output. If the detector elements were assumed to integrate over 1 cm intervals, then the output vanishes for all relative phases of the sinusoidal input wave and the lattice. If, alternatively, the detectors integrated over only 0.5 cm regions but still were spaced at 1.0 cm intervals, then the sinusoidal wave would have vanishing output only when the nodes of the sinusoid fell upon the centers of the 0.5 cm sensitive regions of the detectors and would otherwise change each digital value by a phase-dependent offset from the flat-field value.

The optical transfer function has been written in terms of a Fourier transform using complex exponentials. Since complex-valued exponential inputs are not readily available, it is necessary to ask how T can be experimentally measured. In principle, phantoms machined to produce sinusoidal patterns of x-ray intensity could be used, and by repeated measurements with different offsets one could separate the positive and negative frequency components. A more practical method is the well-known slanted edge technique,^{20,21} in which images are acquired under flat-field conditions except that one half-plane of the detector is shielded so as not to receive any input signal. The detector response D as a function of distance from the edge is referred to as the edge-spread function ESF, which can be differentiated²² to give the line spread function, LSF. Alternatively, by providing an appropriate input the LSF can be acquired directly.²³ The LSF represents integrals through the PSF along lines parallel to the edge, so that by acquiring data with the edge at multiple angles one obtains the radon transform of the PSF. One can reconstruct the PSF, but it is more common to stop after computing the Fourier transform of the ESF, which gives values of the OTF for spatial frequencies \mathbf{f} which are normal to the edge. For discrete-array detectors it is desirable that the slope of the edge is not commensurate with the lattice spacing (for example, on a square grid, if the edge is not parallel to one of the axes and does not have a slope which is a ratio of small whole numbers like 1/2 or 2/3). When this condition is satisfied, for a given region of interest the distances z of the lattice points \mathbf{r}_m from the edge will be distributed sufficiently densely and evenly so that the ESF is said to be "super-sampled," i.e., sampled at a rate significantly higher than the reciprocal of the lattice spacing, so that it is possible to measure values of the OTF for input frequencies beyond those supported by the lattice.

For discrete-array detectors, rotational symmetry will generally be only approximately valid at low spatial frequen-

cies, so it is desirable to make measurements at multiple angles relative to the lattice. When the ESF $_{\theta}$ at a given angle θ is acquired, it is often the case that the precise position of the edge relative to the lattice is not known, so that one actually acquires data for ESF $_{\theta}(z+z_{\theta})$, where z_{θ} represents the lack of knowledge of the exact position of the edge. Upon taking the Fourier transform of the ESF, this introduces a phase uncertainty of the form $e^{2\pi i f |z_{\theta}|}$ into the value of $T(\mathbf{f})$. While this phase uncertainty also occurs in measurements of screen-film systems, for discrete-array systems summations over aliased frequencies generally are not possible given uncertainties in the relative phases of values of T at different spatial frequencies. In general one can remove this phase uncertainty by redefining the lattice positions to correspond to the "centers-of-mass" of the response functions of the sensitive elements. More specifically, if

$$\iint d^2\mathbf{r} P(\mathbf{r}) = \int dz \text{ESF}_{\theta}(z+z_{\theta}) > 0, \quad (40)$$

then it is possible to redefine the lattice (by a shift) so that each lattice point sits at the center of mass of the response function of the associated detector element, giving

$$\iint dx dy x P(\mathbf{r}) = \iint dx dy y P(\mathbf{r}) = 0. \quad (41)$$

With this redefinition of the lattice position, each LSF acquired corresponds to a radon projection of the PSF (onto a line perpendicular to the edge) and thus the center of mass of each LSF should be at the origin. This corresponds to shifting the acquired LSF (adjusting z_{θ}) so that

$$\int dz \text{ESF}_{\theta}(z) z = 0 \quad (42)$$

for each angle.

As a practical matter this results in an increase in the amount of data it is desirable to report for a given detector. If one can assume an inversion symmetry, i.e., $P(\mathbf{r}) = P(-\mathbf{r})$, then the imaginary part of the transfer function will vanish identically, so that only the real part need be reported. The absolute value of the OTF, traditionally called the modulation transfer function (MTF), gives enough information to calculate quantities such as the spatial average of SNR² (Sec. VI), but does not give enough information to explore other aspects of the detector, such as the spatial variation of SNR² as the test object is moved relative to the lattice. Researchers should also note that with the slanted edge technique, when combining raster lines to plot the edge spread function, the independent variable of interest is the distance from the edge, which for square lattices differs from the distance along a raster line by a factor of the cosine of the angle between the raster line and the normal to the edge. This factor becomes significant when trying to measure the transfer function at angles away from the detector axes. Based upon the experience of the authors, one can generally measure values of the OTF at frequencies several times the highest frequency supported by the lattice. One is, of course, measuring the response of the detector at low frequency aliases to higher frequency input signals. Whether the pres-

ence of these aliased signals in the output is desirable will depend upon the task at hand. For example, it might be desirable to detect a high-frequency signal even if one can't distinguish it from a low-frequency signal, or the resulting ambiguity might be unacceptable.

The question of what, if anything, should be identified as either the OTF or MTF for digital systems has been addressed in several ways in the literature. For example, Dobbins²⁴ discusses the "pre-sampled OTF" (OTF_{pre}, our T) as measured via the LSF,²³ but then emphasizes the fact that the response to an input signal with either sinusoidal or delta-function spatial variation will change if the input signal is shifted by a fraction of the lattice spacing. This dependence, which follows from Eq. (38) when the input is expanded into Fourier components, confounds attempts to define the MTF either in terms of the frequency response to a single delta function or as the ratio of output-to-input amplitude for a sinusoid. Dobbins addresses this issue by defining

$$\text{OTF}_d(\mathbf{f}) = \sum_{\mathbf{f}_i} \text{OTF}_{\text{pre}}(\mathbf{f} + \mathbf{f}_i), \quad (43)$$

and defining EMTF(\mathbf{f}) as the amplitude of the detector response at frequency \mathbf{f} to a delta-function input averaged over all positions of the delta function. Giger and Doi²⁵ included such a summation of OTF over aliased frequencies in their study of data acquisition and display for digital systems. Both OTF_d and EMTF can be computed in terms of the OTF, but it can be seen that neither is sufficient for calculating SNR. Metz²⁶ approaches the problem in essentially the same manner as discussed in this paper, and indeed Eqs. (19) and (30) of that paper essentially give our Eq. (38), but for a slightly more specialized case. Metz then brings up the point that a shift by a fraction of the lattice spacing in the input signal does not result in a simple shift in the output data, and concludes that "the effect is accounted for mathematically, but it prevents us from defining a unique 'transfer function' of the sampling process."

Experimentally, Sones and Barnes²⁷ recognized the desirability of measuring the transfer function above the maximum frequency supported by the sampling lattice in their work with a digital radiography unit. This measurement was performed using a novel technique based upon a phantom consisting of periodically arranged wires, the distance between the wires chosen to be incommensurate with the distance between samples acquired by the detector. Fujita, Doi, and Giger²⁸ measured the "pre-sampling analog MTF" above the maximum frequency supported by their sampling lattice via a slanted slit technique and recognized that "knowledge of the pre-sampling analog MTF ... will be useful in the determination of signal-to-noise ratio (SNR) [and] the evaluation of digital systems," a statement with which we heartily agree.

Working from a complementary theoretical perspective, Barrett *et al.*¹ uses the "cross-talk" matrix to address the more general case of any detector whose response is linear, then proceeds to more specialized cases. In Barrett *et al.*, the input to the system is defined as the object being imaged

parameterized in terms of the coefficients of its three-dimensional Fourier series, while for our purposes the input is the x-ray fluence incident on the detector. For projection radiography, which is our primary interest, the incident x-ray fluence is directly related to the integrated attenuation coefficient of the object along rays diverging from the x-ray focus, at least to a first approximation. As our goal is to attempt to quantify the detector response independently of other technical factors, this approximation is adequate. Barrett *et al.* is concerned with detectors which may have relatively few sensitive elements, so the application of Fourier techniques to the acquired data is not considered. Barrett *et al.* applies the cross-talk matrix to the case of a one-dimensional array of detector elements with aperture size equal to the element spacing, and finds that the cross-talk between components of the input at separate frequencies decreases as the length of the array is increased, so long as the frequencies are not aliases of each other. Thus in the limit of a homogeneous detector of infinite extent one recovers the fact that the transfer function behaves as a sparse matrix, in which all terms vanish except those on the diagonal or relating aliased frequencies.

In order to use Eq. (38) to calculate the response of the detector to a given input, it would be necessary to know the position of the object being imaged with a precision finer than the lattice spacing. Strictly speaking, to calculate the response in either the discrete or continuous case requires that the input be "perfectly known." However, in the case of a continuous detector, a shift in position of the input will result in a corresponding shift in position of the output, while for a discrete detector the "shape" of the output would change. In many cases, such as predicting the detectability of randomly placed objects, one would need to calculate for an ensemble of objects displaced with random phases relative to the lattice, as will be illustrated below in calculating the SNR of small objects.

V. NOISE

Individual realizations of an imaging process have an irreducible variability which sets a fundamental limit on how effectively the detector can distinguish between various inputs. For discrete-array systems, as for screen-film systems, the noise can be quantified in terms of the autocovariance function. If the noise is additive and Gaussian, then the autocovariance matrix completely summarizes the stochastic process which generates the noise. If the system is also stationary, then Fourier techniques can be used to define the Wiener spectrum.

The discrete autocovariance function is given by^{13,15}

$$C(\mathbf{r}_m, \mathbf{r}_n) = \langle D(\mathbf{r}_m) D(\mathbf{r}_n) \rangle, \quad (44)$$

where \mathbf{r}_m and \mathbf{r}_n are points in the lattice of detectors, the angled brackets represent averaging over an ensemble of flat-field images, and as discussed above $\langle D(\mathbf{r}_m) \rangle = 0$ in the absence of a signal. Symmetry under interchange of positions

$$C(\mathbf{r}_m, \mathbf{r}_n) = C(\mathbf{r}_n, \mathbf{r}_m) \quad (45)$$

is an immediate result. With the assumption of stationarity, the autocovariance depends only upon the displacement $\mathbf{r}_m - \mathbf{r}_n$, so we can write

$$C(\mathbf{r}_m, \mathbf{r}_n) = C(\mathbf{r}_m - \mathbf{r}_n) \quad (46)$$

without ambiguity. Note that the difference between two vectors corresponding to lattice points is again a vector corresponding to a lattice point, so C on the right-hand side of Eq. (46) is defined at precisely the lattice points.

The Wiener spectrum $W(\mathbf{f})$ is defined as the discrete space Fourier transform [Eq. (21)] of the autocovariance function $C(\mathbf{r}_m)$. As with any discrete space Fourier transform, the Wiener spectrum is periodic in frequency space [Eq. (22)] so that one need only consider the values of $W(\mathbf{f})$ on a single unit cell of the reciprocal lattice. It is noteworthy that both the autocovariance C and the Wiener spectrum W are real-valued and even. As with screen-film systems, one considers statistics which are linear functions of the data, so if $g(m_1, m_2)$ is a set of real (or complex) numbers defined on the lattice points, one defines

$$\theta_g = |A| \sum_{\mathbf{r}_m} g(\mathbf{m}) D(\mathbf{r}_m). \quad (47)$$

The variance of θ_g (for g complex valued, the sum of the variances of the real and complex parts) is given by

$$\text{Var}(\theta_g) = \langle \theta_g \theta_g^* \rangle \quad (48)$$

$$= |A|^2 \left\langle \left(\sum_{\mathbf{m}} g(\mathbf{m}) D(\mathbf{r}_m) \right) \left(\sum_{\mathbf{n}} g^*(\mathbf{n}) D(\mathbf{r}_n) \right) \right\rangle \quad (49)$$

$$= |A|^2 \sum_{\mathbf{m}} \sum_{\mathbf{n}} g(\mathbf{m}) C(\mathbf{r}_n - \mathbf{r}_m) g^*(\mathbf{n}) \quad (50)$$

in terms of real space. Expressing the autocovariance matrix as the inverse discrete space Fourier transform [Eq. (24)] of the Wiener spectrum one obtains

$$\text{Var}(\theta_g) = |A|^2 \sum_{\mathbf{m}} \sum_{\mathbf{n}} g(\mathbf{m}) \int \int_K d^2 \mathbf{f} \times W(\mathbf{f}) e^{2\pi i \mathbf{f} \cdot (\mathbf{r}_n - \mathbf{r}_m)} g^*(\mathbf{n}) \quad (51)$$

$$= \int \int_K d^2 \mathbf{f} \hat{g}(\mathbf{f}) \hat{g}^*(\mathbf{f}) W(\mathbf{f}), \quad (52)$$

where the second step follows from the definition of the discrete space Fourier transform [Eq. (21)].

Thus one can calculate the variance of a statistic θ_g , which depends in a linear manner upon the data, using either the autocovariance function or the Wiener spectrum. Statistics of this form, for $g(\mathbf{m})$ real-valued, will be seen to correspond to decision variables of ideal observers in Sec. VI. As in the screen-film case, it is useful to consider functions $g(\mathbf{m})$ corresponding to the product of a plane wave and a windowing function, which can be written as

$$g_{\mathbf{f}_0}(\mathbf{m}) = G(\mathbf{m}) e^{2\pi i \mathbf{f}_0 \cdot \mathbf{r}_m}, \quad (53)$$

where $G(\mathbf{m})$ is a real-valued window function with normalization

$$|A| \sum_{\mathbf{m}} G(\mathbf{m})G^*(\mathbf{m})=1, \quad \int \int_K d^2\mathbf{f} \hat{G}(\mathbf{f})\hat{G}^*(\mathbf{f})=1, \quad (54)$$

where the two normalizations are equivalent by Parseval's theorem. Applying Eq. (49) and Eq. (52),

$$\text{Var}(\theta_g) = |A|^2 \left\langle \left| \sum_{\mathbf{m}} G(\mathbf{m})e^{-2\pi i\mathbf{f}_o \cdot \mathbf{r}_m} D(\mathbf{r}_m) \right|^2 \right\rangle \quad (55)$$

$$= \int \int_K d^2\mathbf{f} |\hat{G}(\mathbf{f}-\mathbf{f}_o)|^2 W(\mathbf{f}). \quad (56)$$

For suitable windowing functions G , $|\hat{G}(\mathbf{f}-\mathbf{f}_o)|^2$ will be strongly peaked near \mathbf{f}_o so that one obtains an estimate of the Wiener spectrum at the specified frequency, $W(\mathbf{f}_o)$. In particular, if $G_{\text{rect}}(\mathbf{m})$ is chosen as $1/(M_1M_2|A|)^{1/2}$ at the lattice points $\mathbf{m} \in [0, \dots, M_1-1] \times [0, \dots, M_2-1]$, then

$$\theta_{\text{rect}} = \sum_{m_1=0}^{M_1-1} \sum_{m_2=0}^{M_2-1} \frac{1}{\sqrt{M_1M_2|A|}} D(\mathbf{r}_m) e^{2\pi i\mathbf{f}_o \cdot \mathbf{r}_m}, \quad (57)$$

$$|\hat{G}(\mathbf{f}-\mathbf{f}_o)|^2 = \frac{|A|}{M_1M_2} \frac{\sin^2(M_1\pi(\mathbf{f}-\mathbf{f}_o) \cdot \mathbf{v}_1)}{\sin^2(\pi(\mathbf{f}-\mathbf{f}_o) \cdot \mathbf{v}_1)} \times \frac{\sin^2(M_2\pi(\mathbf{f}-\mathbf{f}_o) \cdot \mathbf{v}_2)}{\sin^2(\pi(\mathbf{f}-\mathbf{f}_o) \cdot \mathbf{v}_2)}, \quad (58)$$

which explicitly shows that for this choice of G , $|\hat{G}(\mathbf{f}-\mathbf{f}_o)|^2$ is strongly peaked near \mathbf{f}_o . For a square lattice with conventional choice of basis vectors, $(\mathbf{f}-\mathbf{f}_o) \cdot \mathbf{v}_1 = (f_x - (f_o)_x)\Delta x$, where $f_x - (f_o)_x$ is the difference in the x components of the frequencies and Δx is the lattice spacing in the x direction, and similarly for the y axis. In general, if a separable window is chosen, so that $G(\mathbf{m}) = G_1(m_1)G_2(m_2)$, then $\hat{G}(\mathbf{f}) = \hat{G}_1(\mathbf{f} \cdot \mathbf{v}_1)\hat{G}_2(\mathbf{f} \cdot \mathbf{v}_2)$, so that one can make use of the variety of one-dimensional windows which have been studied.²⁹

Returning to the case of a general lattice, Eq. (58) shows that for this particular choice of window, as is typical, the estimate of $W(\mathbf{f})$ becomes sharper as the spatial width of the window increases, so that

$$W(\mathbf{f}) = \hat{C}(\mathbf{f}) = \lim_{M_1, M_2 \rightarrow \infty} \langle W_{M_1M_2}(\mathbf{f}) \rangle, \quad (59)$$

$$W_{M_1M_2}(\mathbf{f}) = \frac{|A|}{M_1M_2} \left| \sum_{m_1=0}^{M_1-1} \sum_{m_2=0}^{M_2-1} D(\mathbf{r}_m) e^{-2\pi i\mathbf{f} \cdot \mathbf{r}_m} \right|^2, \quad (60)$$

where, by stationarity, any $M_1 \times M_2$ region of the detector lattice will serve. Specializing to the zero frequency case, $\mathbf{f}=\mathbf{0}$, one gets

$$W(\mathbf{0}) = \lim_{M_1, M_2 \rightarrow \infty} (M_1M_2|A|) \times \left\langle \left(\frac{1}{M_1M_2} \sum_{m_1=0}^{M_1-1} \sum_{m_2=0}^{M_2-1} D(\mathbf{r}_m) \right)^2 \right\rangle, \quad (61)$$

which is the discrete-array version of Selwyn granularity⁵ (the variance in the average digital value corresponds to the

variance in the spatially averaged optical density of film). Comparing Eq. (61) to Eq. (52), one can interpret Eq. (61) as the statement that the integrated response over large regions of the detector depends only upon the low-frequency components of the Wiener spectrum. Viewed spatially, this result means that the digital values averaged over sufficiently large disjoint regions are approximately independent, so that the variance of the average over N large subregions scales with $1/N \propto 1/M_1M_2$.

As with the OTF, the results of the screen-film theory appear as a limiting case for sufficiently fine lattices. Writing Eqs. (59) and (60) as

$$W(\mathbf{f}) = \lim_{M_i \rightarrow \infty} \frac{1}{M_1M_2|A|} \times \left\langle \left| \sum_{m_1=0}^{M_1-1} \sum_{m_2=0}^{M_2-1} |A| D(\mathbf{r}_m) e^{-2\pi i\mathbf{f} \cdot \mathbf{r}_m} \right|^2 \right\rangle, \quad (62)$$

the summations become approximations of the integrals in Eq. (6).

The discrete autocovariance [Eq. (44)], the definition of the Wiener spectrum as the discrete space Fourier transform of the autocovariance, and the use of Fourier components of flat-field images to estimate the NPS [Eq. (59)] have occurred in several places in the medical physics literature,^{13,30} but historically these results seem to have been considered less than satisfactory from a theoretical point of view. For example, Cunningham³¹ stated that while "[i]t is tempting to write out the NPS of [the sampled digital signal], but strictly speaking this violates the shift-invariance assumption since [the data] is sampled and is therefore not shift invariant." More recently, Cunningham,³² in analyzing the concept of NPS in terms of cyclostationary^{15,33} random processes, defines $W_{M_1M_2}$ [Eq. (60)] as "a working definition of the digital NPS." As detailed in Sec. VI, the NPS, as defined here, is precisely the noise which sets the detection-theoretic limits on the use of the detector. In the detection-theoretic approach of Barrett *et al.*,¹ the Fisher information matrix relates the detector noise back into uncertainties in the estimates of the Fourier coefficients of the object being imaged. This has the advantage that it removes the fundamentally arbitrary choice of scale in using digital values, but if aliased frequencies become important the Fisher information matrix becomes singular so that the inversion of this matrix is problematic.

The definition of NPS given here is intended to be operational in the sense that it is defined in a manner which can be implemented using the experimentally available digital values. For the purposes of understanding the sources of noise in detectors, it may be useful to consider the noise in the "presampled" signal, and for some detectors this presampled signal might be experimentally accessible. For example, in a detector based on a phosphor screen coupled with a lens to a charge-coupled device (CCD) camera, one could do experiments in which the camera is replaced by a photographic film. For some devices, such as TFT arrays using direct conversion mechanisms, the meaning of the presampled

mpled signal is less clear as removal or refinement of the sampling array is likely to change the electric fields responsible for charge collection.

As reviewed by Wagner and Sandrik,³⁰ the calculation of the NPS can be implemented in several ways. One method is to estimate the autocovariance function [Eqs. (44) and (46)] using pairs of points in one or (preferably) more images, and then performing the Fourier transform to give the NPS. Alternatively, the variance in the Fourier components is used, as in Eq. (55). If G is chosen as a rectangular window, then Eq. (55) reduces to Eq. (59), so that $\langle W_{M_1 M_2}(\mathbf{f}) \rangle$ [Eq. (60)] is used as an estimate of $W(\mathbf{f})$. In principle the frequency \mathbf{f} is a continuous variable, but the spread of $|\hat{G}(\mathbf{f})|^2$ limits the resolution in frequency space [by Eq. (56)] and this spread is inversely proportional to the size of the spatial region and on the order of $|K|/M_1 M_2$. Given this resolution, it is reasonable to calculate the NPS at $M_1 M_2$ frequencies spaced evenly in the unit cell K in frequency space. Thus, the techniques commonly in use by experimenters give precisely the quantities of interest from our current theoretical point of view, although the use of windows other than the rectangular window might be of interest to obtain better frequency resolution.

Generally, frequency resolution is not a limiting factor in estimating the Wiener spectrum, and the NPS estimated by $\langle W_{M_1 M_2}(\mathbf{f}) \rangle$ is subjected to further smoothing. From Eq. (57) it is seen that $\langle W_{M_1 M_2}(\mathbf{f}_o) \rangle$ is the variance in the random variable θ_{rect} , and as the region of interest used in the calculation is made larger, the variance in θ_{rect} tends to $W(\mathbf{f})$ which will be nonzero in general. Because the variance of θ_{rect} does not vanish, neither will the variance in $|\theta_{\text{rect}}|^2$, so the variance in $W_{M_1 M_2}(\mathbf{f})$ does not converge to zero as $M_1, M_2 \rightarrow \infty$. As the region of interest is made larger, one gains in spectral resolution but not precision, and this represents an unavoidable trade-off.^{30,34} One can only decrease the uncertainty in the estimates of the Wiener spectra by averaging estimates of $W(\mathbf{f})$ from several different regions of interest. Of course, for the purposes of analysis one could divide a large region into several smaller regions, and the averaged value of estimates of $W(\mathbf{f})$ would then have less uncertainty, but the spectral blur would be increased. Since it is often inconvenient to obtain sufficiently many flat-field images to make the standard error in the estimates of $W(\mathbf{f})$ at individual frequencies small, researchers often opt for smoothing the experimental spectrum.

VI. KNOWN SIGNAL DETECTION

Having addressed the issues of OTF and Wiener spectrum, it is now possible to use the signal-to-noise ratio (SNR) to quantify the ability of the detector to perform SKE/BKE tasks. First, however, it is useful to briefly review the meaning of the SNR in terms of an ideal^{9,35} observer working with Gaussian statistics. The ideal observer is challenged with deciding between two hypotheses based upon a given set of data. In the current context, these data consist of the digital values obtained from the detector, and for the moment we will restrict the observer to knowledge of only a finite

region of the detector, corresponding to indexes $\mathbf{m} \in \mathcal{M} = [M_1, \dots, M_1' - 1] \times [M_2, \dots, M_2' - 1]$. This observer works under the assumption that given hypothesis H_I , corresponding to an expected input signal $\langle I(\mathbf{r}) \rangle_I$ and an expected data set $\langle D(\mathbf{r}_m) \rangle_I$, the probability density function describing the expected range and frequency of observed data sets is Gaussian. This Gaussian distribution in $(M_1' - M_1) \times (M_2' - M_2) = \Delta M_1 \Delta M_2$ dimensions, one dimension for each detector element available to the observer, can be written explicitly, but to make the formulas somewhat less cumbersome we use the following notation: $X_m = D(\mathbf{r}_m)$, $\langle X_m \rangle_I = \langle D(\mathbf{r}_m) \rangle_I$, $\langle X_m \rangle_{II} = \langle D(\mathbf{r}_m) \rangle_{II}$, and $\{X_m\} = \{D(\mathbf{r}_m) | \mathbf{m} \in \mathcal{M}\}$ is a $\Delta M_1 \Delta M_2$ -dimensional vector in the space of all possible data values for the detector elements in region \mathcal{M} . The probability distribution which governs the frequency with which particular data sets will be obtained under hypothesis H_I is given by

$$P_I(\{X_m\}) = N_o e^{-1/2 \sum_{\mathbf{m}, \mathbf{n} \in \mathcal{M}} (X_m - \langle X_m \rangle_I) (C^{-1})_{\mathbf{mn}} (X_n - \langle X_n \rangle_I)}, \quad (63)$$

where the normalization factor is given by

$$N_o = \left(\frac{1}{2\pi} \right)^{(\Delta M_1 \Delta M_2)/2} \frac{1}{\sqrt{\det C}}. \quad (64)$$

The matrix $C_{\mathbf{mn}}$ is the autocovariance function $C(\mathbf{r}_m, \mathbf{r}_n)$ of Sec. V restricted to the range $\mathbf{m}, \mathbf{n} \in \mathcal{M}$. The fact that \mathbf{m} and \mathbf{n} are double indices, e.g., \mathbf{m} stands for m_1, m_2 , is not a problem from the theoretical point of view, and in principle for a numerical calculation one could simply choose a convenient one-to-one pairing of the double indices $m_1, m_2 \in \mathcal{M}$ with the integers $1, \dots, \Delta M_1 \Delta M_2$ so that C would be indexed in a more customary manner. Under hypothesis H_{II} , the range and frequency of observed data sets will be governed by a Gaussian probability density P_{II} , this time concentrated around $\langle X \rangle_{II}$. The restricted covariance matrix, C , occurring in both cases, will be the same under the assumption that the noise is additive.

Returning to the question of how to decide between hypothesis H_I and hypothesis H_{II} , if for a given instance of the experiment a data set $\{X_m\} = \{D(\mathbf{r}_m) | \mathbf{m} \in \mathcal{M}\}$ is obtained such that $P_{II}(\{X_m\})$ is relatively large and $P_I(\{X_m\})$ is relatively small, it would generally be reasonable to favor H_{II} . Thus the ideal observer's decision rule based on the likelihood ratio P_{II}/P_I , as discussed below, is intuitively reasonable.

The ideal observer attempts to minimize the expected cost^{9,36} given knowledge of the cost of misclassification under either hypothesis and the *a priori* probabilities associated with each hypothesis,

$$\langle \text{Cost} \rangle = P(H_I) P(\text{ChII}|I) C_{I \rightarrow II} + P(H_{II}) P(\text{ChI}|II) C_{II \rightarrow I}, \quad (65)$$

where in the first term $P(H_I)$ is the *a priori* probability of the state corresponding to hypothesis H_I being true, $P(\text{ChII}|I)$ is the probability of mistakenly choosing hypothesis H_{II} when hypothesis H_I is correct, $C_{I \rightarrow II}$ is the cost associated with this error, and similarly for the second term. Given a region R_{II}

of the $\Delta M_1 \Delta M_2$ dimensional data space and the decision rule that, if the observed data $\{D(\mathbf{r}_m) | \mathbf{m} \in \mathcal{M}\}$ are in R_{II} then the observer rules in favor of hypothesis H_{II} and otherwise in favor of H_I , then the probability of mistakenly favoring hypothesis H_{II} when H_I is correct is

$$P(\text{ChII|I}) = \int \int \dots \int_{R_{II}} d^{\Delta M_1 \Delta M_2} \{X_m\} P_I(\{X_m\}), \quad (66)$$

and, as under either hypothesis the total probability must be unity,

$$P(\text{ChI|II}) = 1 - \int \int \dots \int_{R_{II}} d^{\Delta M_1 \Delta M_2} \{X_m\} P_{II}(\{X_m\}) \quad (67)$$

gives the probability of making the error in the other direction. Combining Eqs. (65)–(67),

$$\begin{aligned} \langle \text{Cost} \rangle &= P(H_{II}) C_{II \rightarrow I} \\ &+ \int \int \dots \int_{R_{II}} d^{\Delta M_1 \Delta M_2} \{X_m\} DC(\{X_m\}), \quad (68) \end{aligned}$$

where

$$\begin{aligned} DC(\{X_m\}) &= P(H_I) C_{I \rightarrow II} P_I(\{X_m\}) \\ &- P(H_{II}) C_{II \rightarrow I} P_{II}(\{X_m\}) \quad (69) \end{aligned}$$

is the differential cost which, if the experiment were repeated sufficiently often, would be attributed to those experiments which gave data $\{D(\mathbf{r}_m) | \mathbf{m} \in \mathcal{M}\}$. Clearly the expected cost given by Eq. (68) is minimized by choosing the region R_{II} to be precisely the region where the differential cost DC is negative, so that the ideal observer's decision rule is to choose hypothesis H_{II} if and only if the likelihood ratio

$$\Lambda = \frac{P_{II}(\{D(\mathbf{r}_m) | \mathbf{m} \in \mathcal{M}\})}{P_I(\{D(\mathbf{r}_m) | \mathbf{m} \in \mathcal{M}\})} \quad (70)$$

exceeds the threshold value

$$\Lambda_o = \frac{P(H_I) C_{I \rightarrow II}}{P(H_{II}) C_{II \rightarrow I}}. \quad (71)$$

By adjusting the operating point Λ_o one makes trade-offs in the rates of the two possible error types, as can be shown graphically in terms of receiver operator curves (ROC analysis).³⁷ Equivalently one can place the cutoff on $\log \Lambda$, and from Eq. (63),

$$\begin{aligned} \log \Lambda &= \sum_{\mathbf{m}, \mathbf{n} \in \mathcal{M}} (\langle D(\mathbf{r}_m) \rangle_{II} - \langle D(\mathbf{r}_m) \rangle_I) (\mathbf{C}^{-1})_{\mathbf{m}\mathbf{n}} D(\mathbf{r}_n) \\ &+ \text{const}, \quad (72) \end{aligned}$$

where the constant term does not depend upon the observed data. Thus an ideal observer, viewing a finite region \mathcal{M} of the detector array, uses a linear statistic $\theta_{\mathcal{M}}$ defined by

$$\theta_{\mathcal{M}} = \sum_{\mathbf{m} \in \mathcal{M}} g_{\mathcal{M}}(\mathbf{r}_m) D(\mathbf{r}_m), \quad (73)$$

where $g_{\mathcal{M}}$ is given implicitly by

$$\sum_{\mathbf{m} \in \mathcal{M}} g_{\mathcal{M}}(\mathbf{r}_m) C(\mathbf{r}_m, \mathbf{r}_n) = (\langle D(\mathbf{r}_n) \rangle_{II} - \langle D(\mathbf{r}_n) \rangle_I), \quad (74)$$

for all $\mathbf{n} \in \mathcal{M}$. On physical grounds, the values of the mask function $g_{\mathcal{M}}(\mathbf{r}_m)$ will be significant only in the region near where $\langle I(\mathbf{r}) \rangle_{II} - \langle I(\mathbf{r}) \rangle_I$ is nonzero. Further from this region, the values of $g_{\mathcal{M}}(\mathbf{r}_m)$ will tend to zero, so that for sufficiently large $\Delta M_1 \Delta M_2$ the ability of the detector to discriminate between the two hypotheses should not depend upon the exact value of $\Delta M_1 \Delta M_2$. In that limit, the efficacy of the detector for the SKE/BKE task should be set by the linear statistic θ_g for the ideal observer's mask function $g_{\mathcal{I}}$. This mask function is defined implicitly by

$$|A| \sum_{\mathbf{m} \in \mathcal{M}} g_{\mathcal{I}}(\mathbf{r}_m) C(\mathbf{r}_m, \mathbf{r}_n) = (\langle D(\mathbf{r}_n) \rangle_{II} - \langle D(\mathbf{r}_n) \rangle_I), \quad (75)$$

where a factor of $|A|$ is introduced to simplify the form of the solution which in the Fourier domain is given by

$$\hat{g}_{\mathcal{I}}(\mathbf{f}) = \frac{\langle \hat{D}(\mathbf{f}) \rangle_{II} - \langle \hat{D}(\mathbf{f}) \rangle_I}{W(\mathbf{f})} \quad (76)$$

$$= \Gamma \frac{\sum_{\mathbf{f}_k} (\langle \hat{I}(\mathbf{f} + \mathbf{f}_k) \rangle_{II} - \langle \hat{I}(\mathbf{f} + \mathbf{f}_k) \rangle_I) T(\mathbf{f} + \mathbf{f}_k)}{W(\mathbf{f})}. \quad (77)$$

The statistic θ_g is itself a Gaussian variable whose variance can be computed using Eq. (52), so that

$$\text{SNR}_{\mathcal{I}}^2 = \Gamma^2 \int_K d^2 \mathbf{f} \frac{|\sum_{\mathbf{f}_k} \langle \Delta I(\mathbf{f} + \mathbf{f}_k) \rangle T(\mathbf{f} + \mathbf{f}_k)|^2}{W(\mathbf{f})} \quad (78)$$

gives the SNR corresponding to the use of the statistic, as defined in Eq. (8). Thus the limiting case of a detector array of infinite extent is well defined, for pixels "far away" from the region of interest do not significantly contribute to the decision. Physically, it is clear that the "tails" of the PSF and autocovariance functions set the relevant scale by which distance from the edge of the array is measured, so that when the projected images of objects appear at a distance from the boundary of several times the lengths of these tails the detector can be treated as essentially infinite and Eq. (78) is valid.

It is acknowledged that there are mathematical subtleties related to a truly infinite detector which are not addressed here. For example,³⁸ the data set for such a detector would represent an infinite set of random variables, so it is not possible to write down a probability density distribution like Eq. (63) in the infinite case. The nature of the physical limit is sufficiently clear that a study of these mathematical subtleties could not change the results. In any case, the fact that the linear statistic θ_g with $g = g_{\mathcal{I}}$ gives the optimal SNR of any linear statistic can be proven directly. More precisely, if $g(\mathbf{r}_m)$ is used to define a linear statistic θ_g , then letting $\Delta D = \langle D \rangle_{II} - \langle D \rangle_I$,

$$\begin{aligned} \left| \int \int_K d^2\mathbf{f} g(\mathbf{f}) \Delta \hat{D}(\mathbf{f}) \right|^2 &= \left| \int \int_K d^2\mathbf{f} (g(\mathbf{f}) \sqrt{W(\mathbf{f})}) \right. \\ &\quad \times \left. \left(\frac{\Delta \hat{D}(\mathbf{f})}{\sqrt{W(\mathbf{f})}} \right) \right|^2 \\ &\leq \int \int_K d^2\mathbf{f} |g(\mathbf{f})|^2 W(\mathbf{f}) \\ &\quad \times \int \int_K d^2\mathbf{f} \frac{|\Delta \hat{D}(\mathbf{f})|^2}{W(\mathbf{f})}, \end{aligned} \quad (79)$$

where the second step is an application of the Schwarz inequality. Dividing both sides of Eq. (79) by the first factor on the right, one obtains

$$\frac{\left| \int \int_K d^2\mathbf{f} g(\mathbf{f}) \Delta \hat{D}(\mathbf{f}) \right|^2}{\int \int_K d^2\mathbf{f} |g(\mathbf{f})|^2 W(\mathbf{f})} \leq \int \int_K d^2\mathbf{f} \frac{|\Delta \hat{D}(\mathbf{f})|^2}{W(\mathbf{f})}, \quad (80)$$

where the quantity on the left is the SNR^2 for the statistic θ_g [Eqs. (8) and (52)] and the quantity on the right, proven to be larger, is the SNR^2 of the ideal observer as given by Eq. (78) [with Eq. (38)].

As a slightly less subtle point, the construction of the ideal observer involves dividing by $W(\mathbf{f})$, which is problematic if $W(\mathbf{f})=0$ at some frequency. For physical detectors, the Wiener spectrum never vanishes as there is always some residual noise. Even for highly idealized detectors, the Wiener spectrum must reflect the noise in the incident x-ray fluence so that it can only disappear at frequencies where the OTF vanishes, and at these frequencies the Wiener spectrum will vanish no faster than $\text{OTF}^2(\mathbf{f})$ (discussed in more detail in the next section), so that even in this case the SNR as given by Eq. (78) is a well-defined limit.

The SNR given by Eq. (78) corresponds to the SKE/BKE decision task using a discrete-array detector, as Eq. (13) gives the SNR for the SKE/BKE decision task for screen-film. Strictly, these formulas do not apply to the task of detection when the observer does not know the position of the object being imaged. For detecting a signal of unknown location, one can calculate the ideal observer's SKE/BKE $\theta_{\mathcal{I}}(\mathbf{r})$ for each possible position \mathbf{r} of the object. A common strategy is then to apply a threshold to $\theta_{\mathcal{I}}(\mathbf{r})$. Under the assumption of Gaussian statistics with complete knowledge except for position, the likelihood ratio computed by the ideal observer uses $\theta_{\mathcal{I}}(\mathbf{r})$ in a nonlinear manner^{35,39,40} that is sensitive to peaks in $\theta_{\mathcal{I}}(\mathbf{r})$. In either case, the values of SNR given by Eqs. (13) and (78) are indicative of the efficacy of the ideal observer in the more general case of the position being unknown.

For the discrete-array detector, however, the value of the SNR for the SKE/BKE case will depend upon exactly where the object is relative to the lattice. While this variation can be significant (for example detectors could have interstitial spaces where objects completely disappear), the magnitude of the effect decreases for objects large relative to the lattice spacing. Examples of this for several simple model detectors will be given in the next section. If the variation in SNR^2

with position is not too great, then the spatially averaged value of SNR^2 will be of use.¹ This spatial average can be computed exactly by noting that if an object is shifted by a displacement \mathbf{r} , the Fourier transform is multiplied by $e^{2\pi i \mathbf{f} \cdot \mathbf{r}}$ so that in Eq. (78) the sum over elements of the reciprocal lattice becomes

$$\left| \sum_{\mathbf{f}_k} \langle \Delta \hat{I}(\mathbf{f} + \mathbf{f}_k) \rangle T(\mathbf{f} + \mathbf{f}_k) e^{2\pi i \mathbf{f}_k \cdot \mathbf{r}} \right|^2, \quad (81)$$

where a common factor independent of \mathbf{k} ($|e^{2\pi i \mathbf{f} \cdot \mathbf{r}}|=1$) has been removed. In averaging over positions \mathbf{r} in Eq. (78), the denominator of the integrand does not depend upon \mathbf{r} , and the numerator is the square of the magnitude of a Fourier series in \mathbf{r} , so that in integrating over \mathbf{r} to obtain the average over all displacements one can apply Parseval's theorem to obtain

$$\begin{aligned} \langle \text{SNR}^2 \rangle &= \Gamma^2 \int \int_K d^2\mathbf{f} \frac{\sum_{\mathbf{f}_k} |\Delta \hat{I}(\mathbf{f} + \mathbf{f}_k)|^2 |T(\mathbf{f} + \mathbf{f}_k)|^2}{W(\mathbf{f})} \\ &= \Gamma^2 \int \int d^2\mathbf{f} \left(\frac{|T(\mathbf{f})|^2}{W(\mathbf{f})} \right) |\Delta \hat{I}(\mathbf{f})|^2, \end{aligned} \quad (82)$$

where the second step follows from noting that the sum of the integrals over each unit cell is equivalent to the integral over the entire plane.

As for the OTF and NPS, the film-screen result, Eq. (13), can be recovered from the discrete-array result [Eq. (78)] by going to the limit of a sufficiently fine lattice, in which case the distance to the first aliased frequency is so large that only the unaliased term contributes to Eq. (78). Similarly, for a sufficiently fine lattice all objects are large relative to the lattice spacing, so that SNR^2 does not vary appreciably as the object is moved relative to the lattice spacing. These facts prompt the identification¹ of

$$\text{GNEQ}(\mathbf{f}) = \Gamma^2 |T(\mathbf{f})|^2 \Phi^2 / W(\mathbf{f}), \quad (83)$$

as a generalization of the concept of noise equivalent quantum flux (NEQ), where Φ is the incident x-ray flux, and

$$\text{GDQE}(\mathbf{f}) = \Gamma^2 |T(\mathbf{f})|^2 \Phi / W(\mathbf{f}), \quad (84)$$

as a generalized detective quantum efficiency (DQE). These results parallel the screen-film theory, except that factors of fluence appear in the numerator as the response of digital detectors is linear with fluence [Eq. (33)] while film density is linear with respect to the log of fluence [Eq. (1)]. While Eq. (82) is exact in the context of the assumptions we have made about the detector, SNR^2 enters nonlinearly into other quantities such as the various probabilities of misclassification for a given operating point (sometimes called the false positive fraction and the false negative fraction in ROC methodology). However, when the variation in SNR^2 is not too large, perhaps as measured by the rms (root-mean-square variation in SNR^2), then the GNEQ and spatially averaged SNR^2 can be considered a useful summary of the efficacy of the detector.

In this paper we have applied the concept of an ideal observer directly to the digital data. The results obtained are

implicit in the work of Giger *et al.*,^{13,25,41,42} but Giger *et al.* concentrates on issues of display and models of human visual response to the displayed data. As these tasks are decoupled from image acquisition for digital systems, it is worth considering figures of merit for the data acquisition system independent of the display, as done here. The results of this section also follow as limiting cases of the work of Barrett *et al.*¹ Of particular note, Sec. V A¹ discusses a simple binning detector and obtains

$$\text{SNR}^2 = \sum_{m=1}^M \frac{\Delta \bar{g}_m^{-2}}{\sigma_m^2}, \quad (85)$$

where σ_m is the uncorrelated noise in the m th detector and $\Delta \bar{g}_m$ is the expected change in the data value at the m th detector which would be caused by the signal. This particular result can be obtained directly from first principles based on counting statistics in each detector element. In the stationary case, $\sigma_m = \sigma$ is a constant, so in Eq. (78) $W(\mathbf{f}) = \sigma^2 |A|$ and the numerator [using Eq. (38) and Parseval's identity] becomes $|A| \sum_m |\Delta \langle D(\mathbf{r}_m) \rangle|^2$, again recovering the result [Eq. (85)] based on counting statistics for uncorrelated noise. It is worth noting that if one does not include the aliased terms in the numerator of Eq. (78) (perhaps on the grounds that aliased signals are not useful), the value of SNR^2 will be underestimated. The aliased response is part of the physical response of the detector, and in this case the aliased terms will add coherently in such a manner as to bring the calculated value of the SNR^2 up to the value in Eq. (85) obtained from counting statistics.

VII. MODEL DETECTORS

To give a feel for the implications of the above theory, the capabilities of detectors with reasonably realistic parameters will now be investigated. The modeling is somewhat simplistic, but sufficient to demonstrate several interesting properties, such as the dependence of SNR on the position of the object being imaged, and certain trade-offs inherent in such detectors, particularly those trade-offs related to the possible suppression of input spatial frequencies above the frequencies supported by the lattice. The incident x-ray fluence Φ has a white Wiener spectrum, $W_i(\mathbf{f}) = \Phi$. Among other simplifications, which will be discussed in more detail at the end of the section, we assume 100% of the x-rays interact. Each x-ray undergoes a stochastic amplification, characterized by an average of m secondary quanta per x-ray with $\sigma_m = \sqrt{m}$ for a Poisson process, and the secondary quanta undergo a stochastic scattering process, with a spread function P_s and transfer function T_s , before being "binned" by the detector elements. The result is an average of $m\Phi$ secondary quanta per unit area on the detector with a pre-sampled Wiener spectrum given by⁴³

$$W_s(\mathbf{f}) = [m^2 W_i(\mathbf{f}) + \Phi \sigma_m^2 - m\Phi] |T_s(\mathbf{f})|^2 + m\Phi. \quad (86)$$

For a square lattice with spacing L , binning can be considered as a deterministic convolution with rect functions representing the detector regions, so that with

$$T_b(\mathbf{f}) = \left(\frac{\sin(\pi L f_x)}{\pi L f_x} \right) \left(\frac{\sin(\pi L f_y)}{\pi L f_y} \right), \quad (87)$$

the digital noise power spectrum can be written

$$W(\mathbf{f}) = \frac{1}{m^2} \sum_{\mathbf{f}_k} |A|^2 \Phi (m^2 |T_s(\mathbf{f} + \mathbf{f}_k)|^2 + m) |T_b(\mathbf{f} + \mathbf{f}_k)|^2 + W_E, \quad (88)$$

where the factor of $1/m^2$ is introduced so that digital values will correspond to x-ray count and W_E is the electronic noise. With the present conventions the gray-scale characteristic is set to $\Gamma = |A|$. A simplification can be achieved⁴⁴ using

$$\sum_{n=-\infty}^{\infty} \left(\frac{\sin(\pi(x+n))}{\pi(x+n)} \right)^2 = 1 \quad (89)$$

for any x , which can be proven by applying Parseval's theorem to the Fourier series for $e^{2\pi ixy}$ for $y \in [-0.5, 0.5]$. The experimentally observable transfer function (as obtained, for example, by the slanted-edge technique, cf. Sec. IV) contains the effects of stochastic scatter and binning, thus $T(\mathbf{f}) = T_s(\mathbf{f}) T_b(\mathbf{f})$, so that

$$W(\mathbf{f})/|A| = \Phi |A| \sum_{\mathbf{f}_k} |T(\mathbf{f} + \mathbf{f}_k)|^2 + \frac{\Phi |A|}{m} + W_E/|A| \quad (90)$$

is the Wiener spectrum of the model detector, with the average number of x-rays per pixel being $\Phi |A|$. The summation over aliases in Eq. (88) is often referred to as "noise aliasing." The division into aliased and unaliased components is useful for modeling a variety of detectors, but it should be noted that this division is generally not directly experimentally accessible, at least not without modifying the detectors, and that in principle there could be devices which are stationary, and therefore have Wiener spectra, but for which the division of the NPS into aliased and unaliased components is not useful.

It is useful to choose values of the parameters in the model which are representative of detectors of current clinical interest, as this can help in the understanding of the physics which determines the performance of these devices, but detailed modeling for quantitative comparison to actual devices is beyond the scope of this article. We assume a square lattice with spacing of $L = 0.143$ mm, operation at an exposure corresponding to $|A| \Phi = 1400$ x-rays per pixel, and an amplification factor of $m = 1000$. For the stochastic transfer function T_s we consider three possibilities: a "blur-free" detector for which $T_s(\mathbf{f}) = 1$, typical of photoconductive arrays,⁴⁵ and two "alias-free" detectors whose stochastic transfer functions are of the form $T_s(\mathbf{f}) = e^{-\lambda|\mathbf{f}|}$ with $\lambda = 0.463$ and $\lambda = 0.34$ mm, which approximates the transfer function for evaporated CsI.⁴⁶⁻⁴⁸ Typically electronic noise $\sqrt{(W_E)/|A|}$ is on the order of 3-5 x-rays, so values of 0, 4², and 8² cover the range of values for $\Phi |A|/m + W_E/|A|$.

The transfer functions for these models are shown in Fig. 2. As the pixels are symmetric with respect to inversion through their centers [i.e., for the PSF, $P(\mathbf{r}) = P(-\mathbf{r})$], and

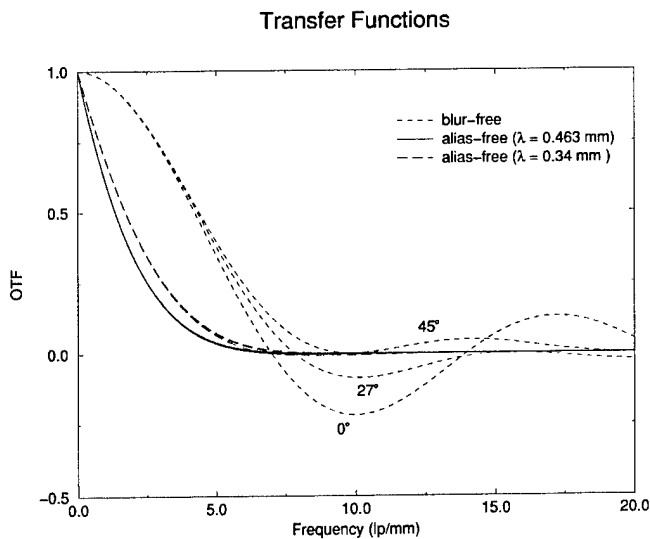


FIG. 2. The optical transfer functions of three model detectors. The “blur-free” detector bins the secondary quanta without smoothing, while for the “alias-free” detectors the distribution of secondary quanta is smoothed by an exponential MTF ($e^{-\lambda|f|}$) before binning. Data are shown as a function of the magnitude of the spatial frequency for several angles.

$P(r)$ is a real number], the imaginary part of the transfer function is identically zero, so only the real part need be graphed. The OTF is, of course, a function of two variables, f_x and f_y . To show this, we plot the OTF as a function of the magnitude of the frequency vector for three angles relative to an axis of the detector. For the blur-free detector, the transfer function is simply the product of the sincs in the two directions induced by the binning operation. The OTF of the blur-free detector is nonzero well beyond the highest frequency supported by the lattice. Any component of an input signal at these higher frequencies will contribute to a lower frequency alias in the output, as per Eq. (38), and while it is not obvious from the point of view of frequency space the sum over aliases in Eq. (38) will be precisely equivalent to the detector

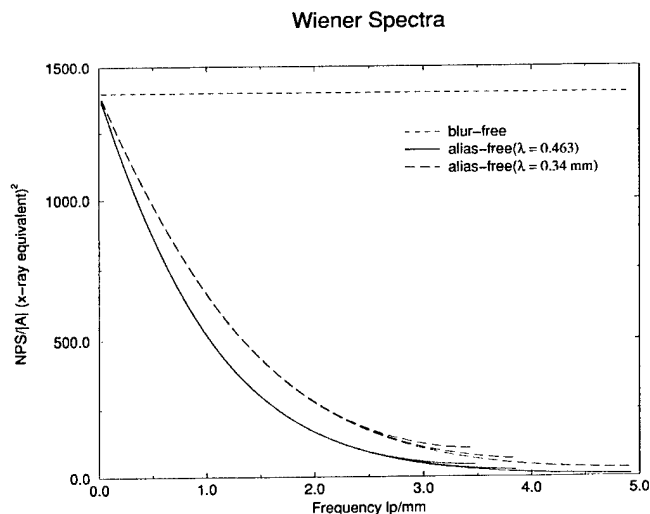


FIG. 3. The Wiener spectra $W(f)/|A|^2$ for the three model detectors as in Fig. 2. The residual additive white noise $\Phi|A|/m + W_E/|A|^2$ has been set to 0.

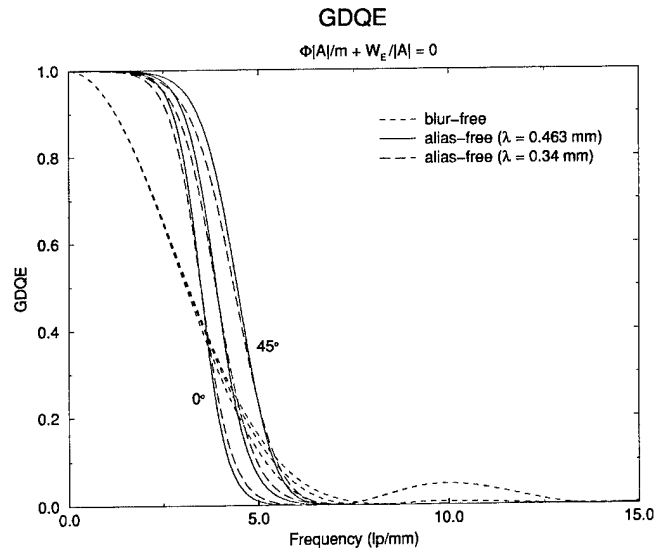


FIG. 4. GDQE as a function of frequency for the three model detectors as in Fig. 2, with the residual white noise $\Phi|A|/m + W_E/|A|^2$ set to 0.

simply binning each incident x-ray. For the alias-free detectors, there is very little response to frequencies beyond those supported by the lattice. For each detector, three angles are plotted, but the angular dependence for the alias-free detectors is small enough to not be apparent on the graph.

The Wiener spectra are shown in Fig. 3. Again, instead of plotting a function of two variables, f_x and f_y , we plot the NPS as a function of the magnitude of the frequency vector for three angles, $\theta=0, 27,$ and 45° (27° corresponds to a slope of 1:2 relative to the lattice). However, the NPS shows little angular dependence. For the Wiener spectrum one only needs to look at frequency values supported by the lattice, i.e., $f_x \in [-1/2L, 1/2L]$ and $f_y \in [-1/2L, 1/2L]$ (for convenience one can consider W to be periodic in the frequency plane). Thus, at $\theta=0^\circ$ one only needs to graph up to $1/2L = 3.5 \text{ mm}^{-1}$, but at $\theta=45^\circ$ the frequencies are on the diagonal of the square, so one goes up to $\sqrt{2}/2L = 4.9 \text{ mm}^{-1}$. At $\theta=27^\circ$, one goes up to $1/(2L \cos \theta) = 4 \text{ mm}^{-1}$. For this graph the constant offset $\Phi|A|/m + W_E/|A|^2$ has been set to zero. For the blur-free detector, the NPS is flat, which follows mathematically from Eq. (89) and the fact that $T(f)$ for these detectors is simply related to sinc functions, or more physically by noting that for a detector which simply bins incident x-rays adjacent cells will be uncorrelated so the NPS is flat. For the alias-free detectors, the NPS is suppressed by factors of the square of the transfer function.

The GDQE as a function of frequency are shown in Figs. 4–6 for a range of values of the residual white noise $\Phi|A|/m + W_E/|A|^2$. For each graph, values are plotted as a function of the magnitude of the spatial frequency for angles 0, 27, and 45° relative to an axis. In each case, the GDQE falls off most quickly at $\theta=0^\circ$ and least quickly at $\theta=45^\circ$, which represents the fact that on the diagonal the sampling rate is increased by a factor of $\sqrt{2}$. In the case where the residual white noise is zero (Fig. 4), the GDQE of the blur-free detector drops like the square of a sinc function. For the

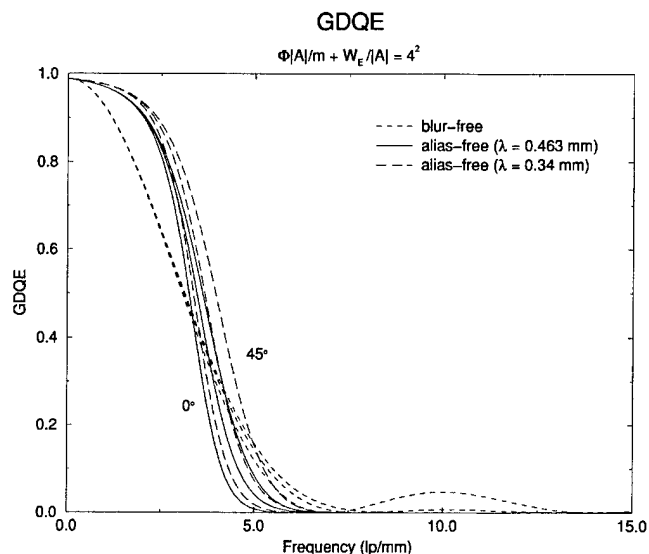


FIG. 5. GDQE as a function of frequency for the three model detectors as in Fig. 2, with the residual white noise $\Phi|A|/m + W_E/|A|$ set to 4^2 .

alias-free detectors, the GDQE remains at nearly unity up to the lattice cutoff, the factor of $T^2(f)$ canceling the same factor in the colored part of the noise. The GDQE of the blur-free detector shows some response beyond the lattice cutoff. Though small, this portion of the GDQE is physical and it will be shown that the responses to the aliased frequencies can not be trivially dismissed. With the addition of residual white noise the GDQE of all three models is reduced, as shown in Fig. 5 ($\Phi|A|/m + W_E/|A| = 4^2$) and Fig. 6 ($\Phi|A|/m + W_E/|A| = 8^2$). These figures illustrate that the alias-free detectors are more sensitive to sources of residual white noise than blur-free detectors. Indeed, in Fig. 6 the blur-free detector now has higher GDQE than the $\lambda = 0.463$ mm detector even at low spatial frequencies. From the spatial point of view this is quite reasonable. A detector

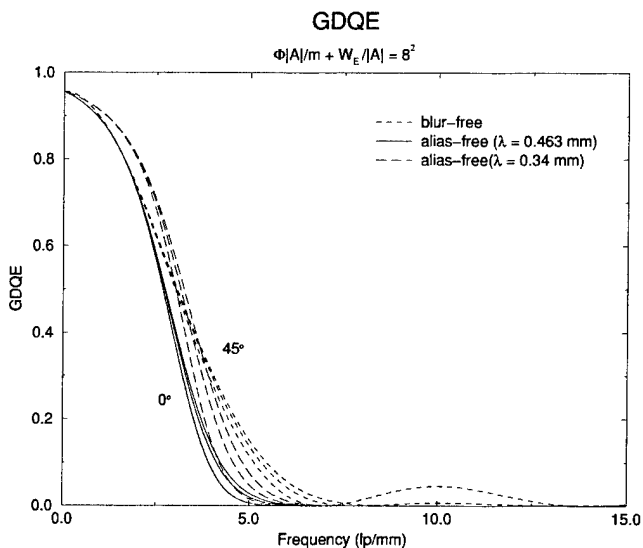


FIG. 6. GDQE as a function of frequency for the three model detectors as in Fig. 2, with the residual white noise $\Phi|A|/m + W_E/|A|$ set to 8^2 .

SNR² as a function of displacement

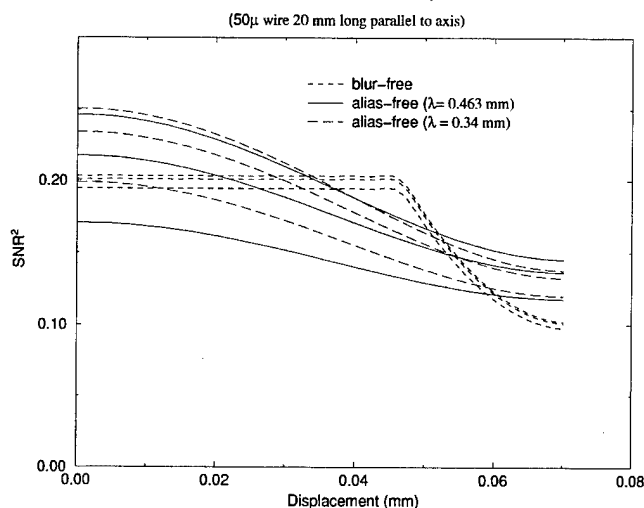


FIG. 7. Relative SNR² as a function of position for a 50 μm wide, 20 mm long wirelike object parallel to one axis of the detector. The horizontal axis of the graph gives the displacement of the wire, so that at 0 mm the wire is over a single column of sensitive elements, while at 0.07 mm the wire straddles two columns. The vertical scale is arbitrary (dependent upon the contrast of the wire).

whose transfer function is designed to remove aliases has a relatively wide point spread function, and therefore a relatively wide autocovariance function. The ideal observer makes use of digital values in array elements whose distance from the position of the signal is up to several times the lengths of the tails of these functions, so for the same input signal the ideal observer will have to integrate over a larger region on an alias-free detector and thus will be more sensitive to any residual uncolored noise.

While GDQE is directly related to the average value of SNR² by Eq. (82), high-frequency signals (i.e., x-ray projection images of small objects or objects whose projected density varies quickly with position) can demonstrate significant changes in SNR² with position. To explore this, consider the SKE/BKE task associated with an object 50 μm wide and 20 mm long. Wires of this width have been used in neurological and cardiovascular stents.⁴⁹ Figure 7 shows the SNR² for such an object, oriented parallel to an axis of the detector, as a function of displacement in the direction of the shorter (50 μm) axis. The scale of the vertical axis is arbitrary as we won't set the inherent contrast of the signal. In Fig. 7, the 0 mm displacement corresponds to the signal being centered over the sensitive elements of the detectors. For the blur-free detector, at 0 mm displacement the signal falls into a single column of detectors, so the SNR² corresponds to counting statistics for one column of elements 20 mm long. The SNR² is constant until the 0.05 mm mark, after which the signal is shared between two columns of detectors, resulting in a drop in SNR². Physically, the number of x-rays attenuated by the object is independent of its position, but at a displacement of 0.7 mm the signal is shared equally between two columns, and since the noise is assumed to be uncorrelated, the variance in the total counts in the two columns is twice that of one column, so the SNR² is

TABLE I. SNR² averaged over position and orientation for the projection image of an object 0.05 by 20 mm. As the SNR² scales with the square of the contrast of the image, only relative values are meaningful. The \pm represent the rms (root-mean-square) fluctuations in the SNR² with position, not the statistical uncertainties.

SNR ² for 50 μ m wide, 20 mm long object			
	$\Phi A /m + W_E/ A =0$	$=4^2$	$=8^2$
Blur-free	1.81 \pm 0.02	1.79 \pm 0.02	1.73 \pm 0.02
Alias-free ($\lambda=0.463$ mm)	2.16 \pm 0.16	1.87 \pm 0.07	1.48 \pm 0.02
Alias-free ($\lambda=0.34$ mm)	2.15 \pm 0.15	1.99 \pm 0.10	1.68 \pm 0.05

reduced by half. The alias-free detectors show less sensitivity to position, as the signal is always shared between multiple columns. As before, curves are shown for three values of the residual white noise $\Phi|A|/m + W_E/|A|$ ($0^2, 4^2$, and 8^2). For all models, the SNR² drops as the residual white noise increases, but this effect is greater for the alias-free models. Table I gives the average SNR² for detection of the 0.05 wide, 20 mm long wire, now averaged over both position and orientation. Additionally, the root-mean-square variation in SNR² is given, to indicate the degree to which the detectability of the wire would vary. Again, the alias-free detectors give a higher SNR² if the residual white noise is kept sufficiently low. In calculating the SNR² of the projection of the wire using Eq. (78), if the summation over aliases is dropped, the resulting integral decreases by about 10%. Thus the contributions of the aliased signal to the SNR are not always negligible.

Somewhat speculatively one can consider tasks which depend upon higher frequency components of the signal.⁵⁰ Consider a 5 mm square with 10% contrast, and a second square whose edges have been smoothed by convolving with a 0.15 mm rect function, so that the resulting signal "ramps up" over a distance of 0.3 mm. The SNR² for the SKE/BKE task of distinguishing between these two objects is given in Table II. It is interesting to note that, mathematically, the SNR² is sufficiently large that the ideal observer can perform this task efficiently, although whether a human could do this is questionable. On the other hand, edge detection is important both computationally and probably as part of the strategy of human observers, so the ability to perform this task is not *a priori* irrelevant. Again, the alias-free detectors have a higher SNR² if the residual white noise is zero, but as the task now depends more heavily on the higher frequency

TABLE II. SNR² averaged over position and orientation for distinguishing between the projection of a 5 mm square with sharp boundaries and a square whose boundaries ramp up over a 0.3 mm region. Normalization corresponds to a 10% contrast with an x-ray flux corresponding to 1400 x-rays/pixel. The \pm represents the rms fluctuations in the SNR² with position, not the statistical uncertainties.

SNR ² for discontinuity vs slope			
	$\Phi A /m + W_E/ A =0$	$=4^2$	$=8^2$
Blur-free	14 \pm 2	14 \pm 2	13 \pm 2
Alias-free ($\lambda=0.463$ mm)	16 \pm 3	12 \pm 1	7.6 \pm 0.5
Alias-free ($\lambda=0.34$ mm)	16 \pm 3	14 \pm 2	10 \pm 1

TABLE III. SNR² averaged over position and orientation for detecting the projection of a 0.5 mm square. Normalization is arbitrary. The \pm represents the rms fluctuations in the SNR² with position, not the statistical uncertainties.

SNR ² for 0.5 mm square			
	$\Phi A /m + W_E/ A =0$	$=4^2$	$=8^2$
Blur-free	1.91 \pm 0.01	1.89 \pm 0.01	1.83 \pm 0.01
Alias-free ($\lambda=0.463$ mm)	2.08 \pm 0.01	1.99 \pm 0.01	1.789 \pm 0.003
Alias-free ($\lambda=0.34$ mm)	2.07 \pm 0.01	2.01 \pm 0.01	1.855 \pm 0.006

components of the signal, the alias-free detectors are more sensitive to residual white noise, with the crossover at $\Phi|A|/m + W_E/|A|=4^2$. The detection of a 0.5 mm square is shown in Table III. Here, the lower (but nonzero) frequencies dominate the response of the detector, so that in general the antialiasing detectors gain from the removal of the aliased noise without losing any signal.

It is interesting to note that the SNRs for the tasks and models described above do not vary greatly. Many factors not considered here will greatly effect the performance of real detectors, beginning with the fact that less than 100% of the incident x-rays will produce secondary quanta. The color of the Wiener spectrum need not be the same as the transfer function, due to, for example, x-rays interacting at various depths in the detector.⁵¹ The efficiency of collection of the secondary quanta can also have significant effects.⁵² For CsI detectors, of which our "alias-free" detector is a rough model, the fill factor is a minor effect so long as the amplification m is sufficiently large.⁴⁸ For selenium detectors, of which our "blur-free" detector is an approximation, it is possible to have an effective fill factor significantly greater than the geometric fill factor of the TFT array.^{53,54} In any case, our purpose here is merely to indicate some of the issues which must be faced in quantifying digital detectors of these types. In addition, we did not consider geometric factors such as x-ray focal spot size and x-ray parallax⁴⁸ which reduce the high-frequency content of the incoming signals.

VIII. DISCUSSION AND CONCLUSION

The results of this paper set up a framework for quantitative measurements of digital systems in a manner analogous to the now common analysis of screen-film systems in terms of the gray-scale transfer characteristic, the optical transfer function, the Wiener spectrum, and signal-to-noise ratio. The logic of this framework is by design close to the classic work on film-screen systems. While many pieces of this argument have appeared in the work of others, as noted throughout the text, it seemed desirable to produce a coherent systematic exposition. The results can be seen as appropriate limits of those of Barrett *et al.*, but the theoretical construction here emphasizes the parallels with the classic results on screen-film systems. While detectors consisting of discrete elements do not have continuous translational symmetry, the remaining discrete symmetry allows one to use the appropriate Fourier technique. The advantage of this, as in the screen-film

case, is that one can explicitly solve for the mask function of the ideal observer [see Eq. (75)] and thereby obtain the optimal SNR. As for screen-film, this formula can be interpreted as the ratio of the square of the signal in each frequency bin to the noise in each frequency bin, as measured by the Wiener spectrum, integrated over bins.

We have investigated several highly idealized, but not completely unrealistic, models of detectors, and illustrated some of the issues inherent in various design decisions. This analysis is incomplete and intended to point toward issues which could be addressed in other work. However, our results suggest that for typical tasks the detectability of objects as determined by SNR^2 is not drastically affected by the decision, in and of itself, to suppress or not to suppress aliases. In any real device, of course, this design decision is linked to many other parameters. This article should be of use in clarifying what is actually experimentally measured in testing such devices.

The results presented here are exact for the SKE/BKE task as approached by the ideal observer under the assumptions of linearity, homogeneity, and stationarity. However, each of these assumptions is only approximately true in practice. The finite extent of real detectors trivially shows that they are not homogeneous, but for a variety of tasks edge effects are negligible. More importantly, many digital detectors in practice show significant inhomogeneity and nonstationarity. The work of Barrett *et al.* is sufficiently general to cover these cases. Further, the inhomogeneity and nonstationarity of a given instrument often occur in ways which are different for each individual device, so that while the extra information is relevant to the particular device one has measured, the extra information is often not generalizable to other devices of the same manufacture. This extra information is useful for optimizing certain tasks using the particular device, but of less use in understanding a class of devices. Additionally, while the signal detection task of the ideal observer under SKE/BKE conditions certainly shares some features with the task which human observers face, and has under many conditions been shown to correlate well with the ability of human observers (for example, screen-film images of nylon beads⁵⁵), it is still a very idealized task. For example, if edge-detection is important, then higher frequency parts of the incoming signal become more important than would be expected given simply the signal detection task. From the point of view of a radiologist, a clear edge might be used to identify and distinguish the existence of a lesion from a variation in projected density of the underlying organ, particularly in the presence of the "structured noise" of other anatomical features.

Clearly these are issues for further study, but while OTF, W, SNR, and GDQE are certainly useful because they are objectively measurable and in a mathematically precise manner are related to tasks which approximate those of the human observer, it is worth remembering that measurement of these quantities does not obviate the need for observer studies, particularly with practicing radiologists.

ACKNOWLEDGMENTS

The authors wish to thank Dr. Robert Wagner and Dr. Robert Gagne of the FDA for helping us to gain insight into the literature. The authors also wish to extend their thanks to Dr. Ian Cunningham for making them aware of his and others' work on cyclostationary processes.

^{a)} Author to whom correspondence should be addressed; electronic mail: Andrew.Maidment@mail.tju.edu

¹ H. H. Barrett, J. L. Denny, R. F. Wagner, and K. J. Myers, "Objective assessment of image quality. II. Fisher information, Fourier crosstalk, and figures of merit for task performance," *J. Opt. Soc. Am. A* **12**(5), 834–852 (1995).

² H. H. Barrett and H. C. Gifford, "Cone-beam tomography with discrete data sets," *Phys. Med. Biol.* **39**, 451–476 (1994).

³ J. M. Boone, "X-ray imaging concepts: Mathematics and modeling," in *Specification, Acceptance Testing and Quality Control of Diagnostic X-ray Imaging Equipment*, edited by J. A. Seibert, G. T. Barnes, and R. G. Gould, Medical Physics Monograph (AIP, Woodbury, NY, 1994), pp. 75–107.

⁴ M. J. Yaffe and R. M. Nishikawa, "X-ray imaging concepts: Noise, SNR and DQE," in *Specification, Acceptance Testing and Quality Control of Diagnostic X-ray Imaging Equipment*, edited by J. A. Seibert, G. T. Barnes, and R. G. Gould, Medical Physics Monograph (AIP, Woodbury, NY, 1994), pp. 109–144.

⁵ J. C. Dainty and R. Shaw, *Image Science* (Academic, New York, 1974).

⁶ H. H. Barrett and W. Swindell, *Radiological Imaging* (Academic, New York, 1981).

⁷ ICRU, "Medical imaging—The assessment of image quality," Technical Report No. 54, International Commission on Radiation Units and Measurements, Bethesda, Maryland, 1996.

⁸ R. S. Strichartz, *A Guide to Distribution Theory and Fourier Transforms* (CRC, Boca Raton, 1994).

⁹ H. L. van Trees, *Detection, Estimation, and Modulation Theory (Part I)* (Wiley, New York, 1968).

¹⁰ J. B. Thomas, *An Introduction to Statistical Communication Theory* (Wiley, New York, 1969).

¹¹ R. F. Wagner and D. G. Brown, "Unified SNR analysis of medical imaging systems," *Phys. Med. Biol.* **30**, 489–518 (1985).

¹² A. V. Oppenheim, R. W. Schaffer, and J. R. Buck, *Discrete-Time Signal Processing*, 2nd ed. (Prentice Hall, Upper Saddle River, NJ, 1999).

¹³ M. L. Giger, K. Doi, and C. E. Metz, "Investigation of basic imaging properties in digital radiography. II. Noise Wiener spectrum," *Med. Phys.* **11**, 797–805 (1984).

¹⁴ J. W. Cooley, P. A. W. Lewis, and P. D. Welch, *The Fast Fourier Transform Algorithm and Its Applications, RC-1743* (IBM Watson Research Center, Yorktown Heights, NY, 1967).

¹⁵ A. Papoulis, *Probability, Random Variables, and Stochastic Processes*, 3rd ed. (McGraw-Hill, New York, 1991).

¹⁶ G. B. Folland, *Fourier Analysis and its Applications* (Brooks/Cole, Pacific Grove, CA, 1992).

¹⁷ J. J. Benedetto, *Harmonic Analysis and Applications* (CRC, Boca Raton, 1997).

¹⁸ F. O. Huck, N. Halyo, and S. K. Park, "Aliasing and blurring in 2-D sampled imagery," *Appl. Opt.* **19**, 2174–2181 (1980).

¹⁹ S. K. Park, R. Schowengerdt, and M.-A. Kaczynski, "Modulation-transfer-function analysis for sampled image systems," *Appl. Opt.* **23**, 2572–2582 (1984).

²⁰ P. F. Judy, "The line spread function and modulation transfer function of a computed tomographic scanner," *Med. Phys.* **3**, 233–236 (1976).

²¹ S. E. Reichenbach, S. K. Park, and R. Narayanswamy, "Characterizing digital image acquisition devices," *Opt. Eng.* **30**, 170–177 (1991).

²² I. A. Cunningham and A. Fenster, "A method for modulation transfer function determination from edge profiles with correction for finite-element differentiation," *Med. Phys.* **14**, 533–537 (1987).

²³ H. Fujita *et al.*, "A simple method for determining the modulation transfer function in digital radiography," *IEEE Trans. Med. Imaging* **11**, 34–39 (1992).

²⁴ J. T. Dobbins III, "Effects of undersampling on the proper interpretation of modulation transfer function, noise power spectra, and noise equivalent quanta of digital imaging system," *Med. Phys.* **22**, 171–181 (1995).

- ²⁵M. L. Giger and K. Doi, "Investigation of basic imaging properties in digital radiography. I. Modulation transfer function." *Med. Phys.* **11**, 287–295 (1984).
- ²⁶C. E. Metz, "Basic imaging theory," in *Recent Developments in Digital Imaging* (1984 Summer School), edited by K. Doi *et al.*, Medical Physics Monograph (AIP, New York, 1985), pp. 1–15.
- ²⁷R. A. Sones and G. T. Barnes, "A method to measure the MTF of digital x-ray systems," *Med. Phys.* **11**, 166–171 (1984).
- ²⁸H. Fujita, K. Doi, and M. L. Giger, "Investigation of basic imaging properties in digital radiography. 6. MTFs of II-TV digital imaging systems," *Med. Phys.* **12**, 713–720 (1985).
- ²⁹F. J. Harris, "On the use of windows for harmonic analysis with the discrete Fourier transform," *Proc. IEEE* **66**, 51–83 (1978).
- ³⁰R. F. Wagner and J. M. Sandrik, "An introduction to digital noise analysis," in *The Physics of Medical Imaging: Recording System Measurements and Techniques* (1979 Summer School), edited by A. G. Haus, Medical Physics Monograph (AIP, New York, 1979), pp. 524–545.
- ³¹I. A. Cunningham, "Analyzing system performance," in *The Expanding Role of Medical Physics in Diagnostic Imaging*, Proceedings of the 1997 Summer School, edited by G. D. Frey and P. Sprawls (Advanced Medical Publishing, Madison, Wisconsin, 1997), pp. 231–263.
- ³²I. A. Cunningham, in *Handbook of Medical Imaging*, edited by J. Beutel, H. L. Kundel, and R. L. van Metter (SPIE, Bellingham, WA, 2000), Vol. 1, Chap. 2.
- ³³W. A. Gardner and L. E. Franks, "Characterization of cyclostationary random signal processes," *IEEE Trans. Inf. Theory* **IT-21**, 4–14 (1975).
- ³⁴J. S. Bendat and A. G. Piersol, *Random Data* (Wiley, New York, 1986).
- ³⁵H. H. Barrett and C. K. Abbey, in *Lecture Notes in Computer Science*, edited by J. Duncan and G. Gindi (Springer, Berlin, 1997), Vol. 1230, pp. 155–166.
- ³⁶H. H. Barrett, C. K. Abbey, and E. Clarkson, "Objective assessment of image quality. III. ROC metrics, ideal observers, and likelihood-generating functions," *J. Opt. Soc. Am. A* **15**(6), 1520–1535 (1998).
- ³⁷D. M. Green and J. A. Swets, *Signal Detection Theory and Psychophysics* (Wiley, New York, 1966).
- ³⁸I. Karatzas and S. E. Shreve, *Brownian Motion and Stochastic Calculus*, 2nd ed. (Springer, New York, 1991).
- ³⁹E. Clarkson and H. Barrett, in *Lecture Notes in Computer Science*, edited by J. Duncan and G. Gindi (Springer, New York, 1997), Vol. 1230, pp. 549–554.
- ⁴⁰D. G. Brown, M. F. Insana, and M. Tapiovaara, "Detection performance of the ideal decision function and its McLaurin expansion: Signal position unknown," *J. Acoust. Soc. Am.* **97**, 379–398 (1995).
- ⁴¹M. L. Giger and K. Doi, "Effect of pixel size on detectability of low-contrast signals in digital radiography," *J. Opt. Soc. Am. A* **4**(5), 966–975 (1987).
- ⁴²M. L. Giger and K. Doi, "Investigation of basic imaging properties in digital radiography. 3. Effect of pixel size on SNR and threshold contrast," *Med. Phys.* **12**, 201–208 (1985).
- ⁴³M. Rabbani, R. Shaw, and R. van Metter, "Detective quantum efficiency of imaging systems with amplifying and scattering mechanisms," *J. Opt. Soc. Am. A* **4**(5), 895–901 (1987).
- ⁴⁴K. M. Hanson, "The detective quantum efficiency of CT reconstruction: The detection of small objects," in *Application of Optical Instruments in Medicine VII*, edited by J. E. Gray, *Proc. SPIE* **173**, 291–298 (1979).
- ⁴⁵D. L. Lee, L. K. Cheung, B. Rodricks, and G. F. Powell, "Improved imaging performance of a 14×17-inch Direct Radiography (TM) System using Se/TFT detector," in *SPIE Conference on Physics of Medical Imaging* [*Proc. SPIE* **3336**, 14–23 (1998)].
- ⁴⁶J.-P. Moy, "Image quality of scintillator based X-ray electronic imagers," in *SPIE Conference on Physics of Medical Imaging* [*Proc. SPIE* **3336**, 187–194 (1998)].
- ⁴⁷C. Chaussat, J. Chabbal, T. Ducourant, V. Spinnler, G. Vieux, and R. Neyret, "New CsI/a-Si 17"×17" X-ray flat panel detector provides superior detectivity and immediate direct digital output for General Radiography systems," in *SPIE Conference on Physics of Medical Imaging* [*Proc. SPIE* **3336**, 45–55 (1998)].
- ⁴⁸J.-P. Moy, "Signal-to-noise ratio and spatial resolution in x-ray electronic imagers: Is the MTF a relevant parameter?," *Med. Phys.* **27**, 86–93 (2000).
- ⁴⁹J. J. Connors III, J. C. Wojak, and Z. Qian, in *Interventional Neuroradiology: Strategies and Practical Techniques*, edited by J. J. Connors III, and J. C. Wojak (W. B. Saunders, Philadelphia, 1999), Chap. 1.
- ⁵⁰K. M. Hanson, "Variations in task and the ideal observer," *Proc. SPIE* **419**, 60–67 (1983).
- ⁵¹G. Lubberts, "Random noise produced by x-ray fluorescent screens," *J. Opt. Soc. Am.* **58**, 1475–1483 (1968).
- ⁵²I. A. Cunningham, "Degradation of the detective quantum efficiency due to a non-unity detector fill factor," in *Phys. Med. Imaging* **3032**, 22–31 (1997).
- ⁵³J. A. Rowlands and J. Yorkston, in *Handbook of Medical Imaging*, edited by J. Beutel, H. L. Kundel, and R. L. van Metter (SPIE, Bellingham, WA, 2000), Vol. 1, Chap. 4.
- ⁵⁴G. Pang, W. Zhao, and J. A. Rowlands, "Digital radiology using active matrix readout of amorphous selenium: Geometrical and effective fill factors," *Med. Phys.* **25**, 1636–1646 (1998).
- ⁵⁵L.-N. D. Loo, K. Doi, and C. E. Metz, "A comparison of physical image quality indices and observer performance in the radiographic detection of nylon beads," *Phys. Med. Biol.* **29**, 837–856 (1984).

Medical Physics

AVAILABLE ONLINE—See <http://www.medphys.org>

September 2002

Volume 29, Number 9

Mammogram synthesis using a 3D simulation. I. Breast tissue model and image acquisition simulation

Predrag R. Bakic and Michael Albert

Department of Radiology, Thomas Jefferson University, Suite 3390, Gibbon Building, 111 South 11th Street, Philadelphia, Pennsylvania 19107-5563

Dragana Brzakovic

Office of Integrative Activities, National Science Foundation, Arlington, Virginia 22230

Andrew D. A. Maidment

Department of Radiology, Thomas Jefferson University, Suite 3390, Gibbon Building, 111 South 11th Street, Philadelphia, Pennsylvania 19107-5563

pp. 2131-2139

Mammogram synthesis using a 3D simulation.

I. Breast tissue model and image acquisition simulation

Predrag R. Bakic and Michael Albert

Department of Radiology, Thomas Jefferson University, Suite 3390, Gibbon Building, 111 South 11th Street, Philadelphia, Pennsylvania 19107-5563

Dragana Brzakovic

Office of Integrative Activities, National Science Foundation, Arlington, Virginia 22230

Andrew D. A. Maidment^{a)}

Department of Radiology, Thomas Jefferson University, Suite 3390, Gibbon Building, 111 South 11th Street, Philadelphia, Pennsylvania 19107-5563

(Received 25 February 2002; accepted for publication 14 June 2002; published 27 August 2002)

A method is proposed for generating synthetic mammograms based upon simulations of breast tissue and the mammographic imaging process. A computer breast model has been designed with a realistic distribution of large and medium scale tissue structures. Parameters controlling the size and placement of simulated structures (adipose compartments and ducts) provide a method for consistently modeling images of the same simulated breast with modified position or acquisition parameters. The mammographic imaging process is simulated using a compression model and a model of the x-ray image acquisition process. The compression model estimates breast deformation using tissue elasticity parameters found in the literature and clinical force values. The synthetic mammograms were generated by a mammogram acquisition model using a monoenergetic parallel beam approximation applied to the synthetically compressed breast phantom. © 2002 American Association of Physicists in Medicine. [DOI: 10.1118/1.1501143]

Key words: mammography simulation, 3D, breast tissue, mammographic compression, x-ray image acquisition

I. INTRODUCTION

Visibility of breast lesions in mammography is compromised by overlapping projections of normal anatomic structures that generate a background texture, which can mask existing abnormalities or introduce false ones. Several authors¹⁻³ have shown that these parenchymal patterns are often the limiting factor in detection tasks. A 3D simulation of mammography is proposed to provide insight into the formation of such patterns. The simulation allows one to analyze the correlation between the 3D composition of the breast and its 2D mammographic appearance. By identifying the dominant anatomical structures found in an average breast, this model can help analyze the deformation of those structures during the exam and their appearance in mammograms. A 3D mammography simulation can also serve as a complement to experiments with respect to positioning, compression, and acquisition. Optimization of imaging parameters (such as compression angle and force, x-ray tube kVp and mAs, etc.) cannot be achieved by repeatedly imaging the same patient, due to concerns about the radiation dose. Such simulations can also be useful in training medical personnel by demonstrating the effects of technique selection on image quality or by determining 3D lesion position from two or more projections. Finally, a 3D breast model can provide a theoretical framework for testing new breast imaging modalities. Many new modalities are being developed today, including stereoscopy,⁴⁻⁶ tomosynthesis,⁷ and 3D image reconstruction,⁸ which are expected to provide more diagnostic information about normal and abnormal tissue structure. It is

essential in the development of such systems to have a tool that can be used to test the visibility of breast structures and help select optimal views for 3D reconstruction, since the number of views is limited by the amount of radiation received.

Historically, mammography simulation started with the design of the first mathematical breast models for computing the dose received by a patient during an examination using Monte Carlo simulation of x-ray interactions.⁹ These simulations have used fairly crude models of breast anatomy, lacking internal structures. More recent analytical models of mammographic image acquisition have related the average values of the incident x-ray flux, linear attenuation coefficients of breast tissue, and the film density or pixel digital values in the obtained mammograms.¹⁰

There are two approaches to modeling the image content of mammograms. In a 2D approach, mammograms are modeled based upon the analysis of spatial correlation between image pixel values, using various random field methods.¹¹⁻¹³ Such models can match some of the statistical properties of real mammograms, but they cannot reveal the relationship between the 3D structures of the breast, nor they can consistently produce images of the same breast with modified position or acquisition parameters.

In this paper we propose a second approach, whereby mammograms are modeled by projection of simulated 3D anatomic structures, based upon the size and the distribution of large and medium scale tissue regions found in the breast. It is our hypothesis that the distribution of the 2D structures seen in mammograms reflects the distribution of the 3D tis-

Mammography Simulation

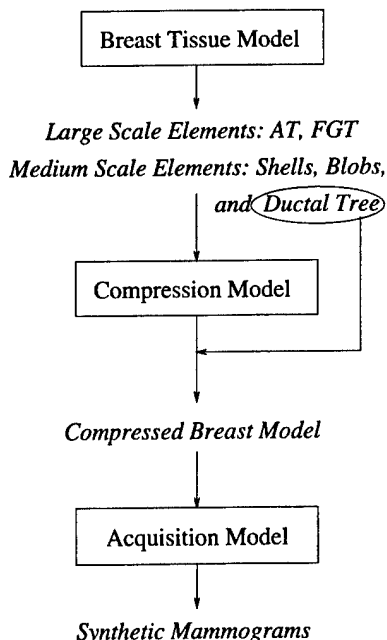


FIG. 1. Components of a system for mammography simulation. The flowchart shows the order (top-to-bottom) in which the model components are simulated.

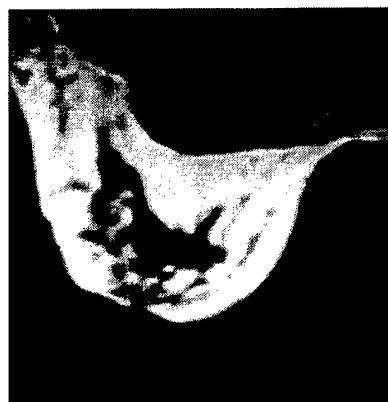
sue structures of the breast. Thus, the background texture in the synthetic mammograms so generated, should have similar properties to those found in clinical images.

Positioning and compression significantly affect the appearance of mammograms. Until recently^{14–16} there were no models of breast deformation, due to the complex anatomy of the different types of interwoven breast tissue, whose mechanical properties are difficult to analyze. We have approximated breast compression by separate deformations of tissue layers positioned normal to the compression plates.

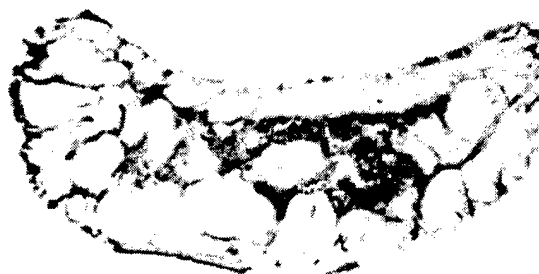
The objective of this work is to generate synthetic mammograms. A method for achieving this goal is described in Sec. II, while the results of the simulation are shown in Sec. III. An accompanying paper details an analysis of the quality of the model.¹⁷

II. MAMMOGRAPHY SIMULATION

The proposed mammography simulation consists of three major components: a 3D software breast phantom, a compression model, and an x-ray image acquisition model (see Fig. 1). The breast phantom is a software tissue model containing two ellipsoidal regions of large scale tissue elements: predominantly adipose tissue (AT) and predominantly fibroglandular tissue (FGT). The internal tissue structures of these regions, namely the adipose compartments and the breast ductal network, are approximated by realistically distributed medium scale phantom elements: shells, blobs, and the simulated ductal tree. The compression model is based upon tissue elasticity properties and a breast deformation model. Deformation is simulated separately for tissue slices (or layers)



(a)



(b)

FIG. 2. Anatomic structures of the breast included in the tissue model. (a) Large scale regions seen in MRI images as predominantly adipose tissue region, AT (bright), and predominantly fibroglandular region, FGT (dark surrounded by the AT). (b) Subgross (thick) histologic slice showing large scale regions: AT and FGT, and medium scale tissue structures: compartments surrounded by Cooper's ligaments in the AT and small adipose cavities and ducts within the FGT. (Subgross breast histology image provided courtesy of Dr. R. D. Cardiff.)

positioned normal to the compression plates. Each slice is approximated by a beam composed of two different tissues. Deformed slices are stacked to produce a model of the compressed breast. The mammogram acquisition model was adopted from the literature,¹⁰ assuming monoenergetic x rays and a parallel beam geometry without scatter. Presently, the synthetic mammograms are generated with a spatial resolution of $200 \mu\text{m}/\text{pixel}$ because the current model version does not include fine tissue details. This resolution is comparable to the resolution of digitized mammograms in the Mini MIAS database (obtained by averaging 4×4 pixels in the original MIAS database¹⁸).

A. Software breast phantom

1. Modeling large scale tissue regions

Figure 2 illustrates the types of anatomic structures of the breast which are included in the breast phantom. Figure 2(a) is an MRI breast section, showing the shape and position of

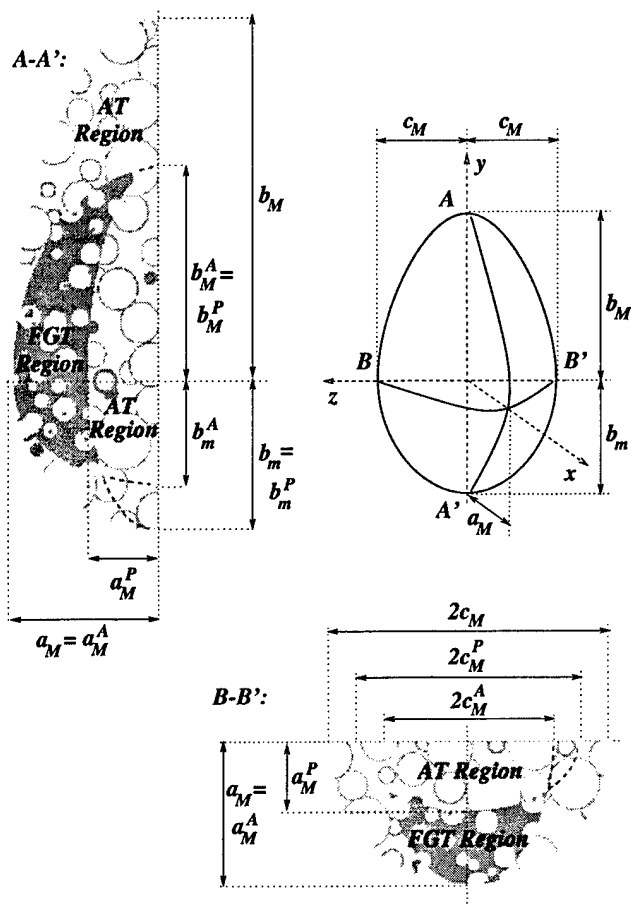


FIG. 3. Orthogonal sections of the uncompressed breast model. Parameters without subscripts correspond to the semi-axes of the ellipsoidal approximation of the breast outline; superscripts *A* and *P* correspond to the anterior and posterior border of the FGT model region, respectively.

the large scale tissue regions. The MRI shows the predominantly fibroglandular tissue, appearing as a dark region in the central part of the breast, and the predominantly adipose tissue, a brighter region surrounding the fibroglandular tissue. Internal structures of these tissue regions are less clearly visible, due to the relatively low MRI resolution of approximately 1 mm/pixel. Figure 2(b) shows a subgross histologic slice of the breast, obtained after mastectomy. The predominantly fibroglandular region in the slice is represented by a darker image region in the center, surrounded by brighter, predominantly adipose tissue. Adipose tissue is organized into round compartments, formed by fibrous Cooper's ligaments. The FGT region also contains adipose compartments, but they are smaller in size than the compartments in the AT region. Analysis of subgross histologic slices of the breast and the corresponding mammograms showed that projections of these compartments dominantly contribute to the formation of parenchymal patterns. Therefore, simulated adipose compartments were included as medium scale breast model elements.

2. Modeling adipose tissue compartments

The adipose compartments are approximated by thin shells in the AT region and small blobs in the FGT region.

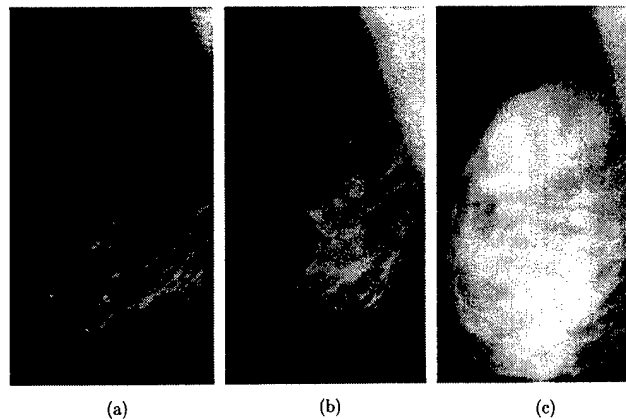


FIG. 4. Examples of different tissue distributions in real breasts, illustrated with clinical mammograms from the MIAS database. The amount of adipose tissue affects the size and visibility of compartments seen in the AT and FGT regions.

The interiors of the shells and blobs have the elastic and x-ray attenuation properties of adipose tissue. As a first approximation, the adipose compartments are represented by spheres. The size of the spheres can vary to allow for normal breast anatomic variations.

Figure 3 shows two orthogonal cross sections of a breast tissue phantom. Simulated regions of predominantly adipose and predominantly fibroglandular tissue are seen, together with the spherical approximation of adipose compartments in those regions. Note that the size of the simulated compartments in the AT and FGT regions differ. The size of the adipose compartments varies in different women, depending upon the amount of adipose tissue in the breast, as seen in

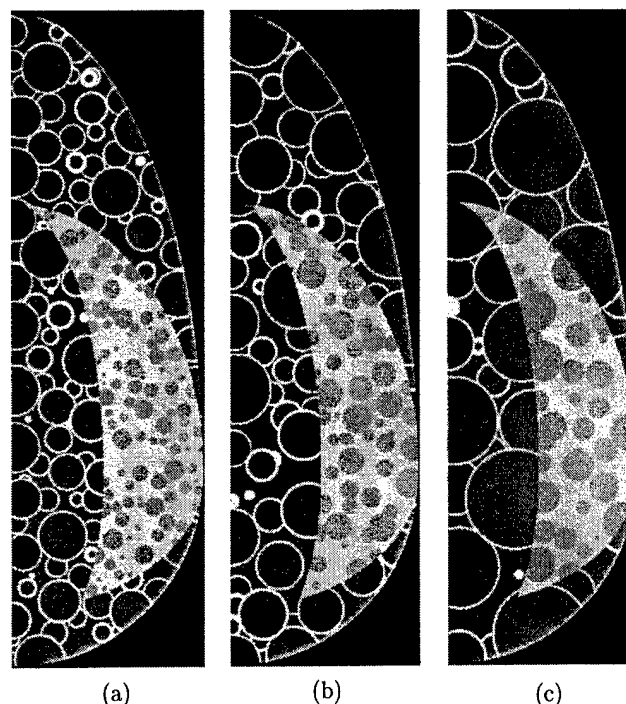


FIG. 5. Sections of breast models with different sized tissue elements labeled according to Table I as: (a) "Small," (b) "Medium," and (c) "Large."

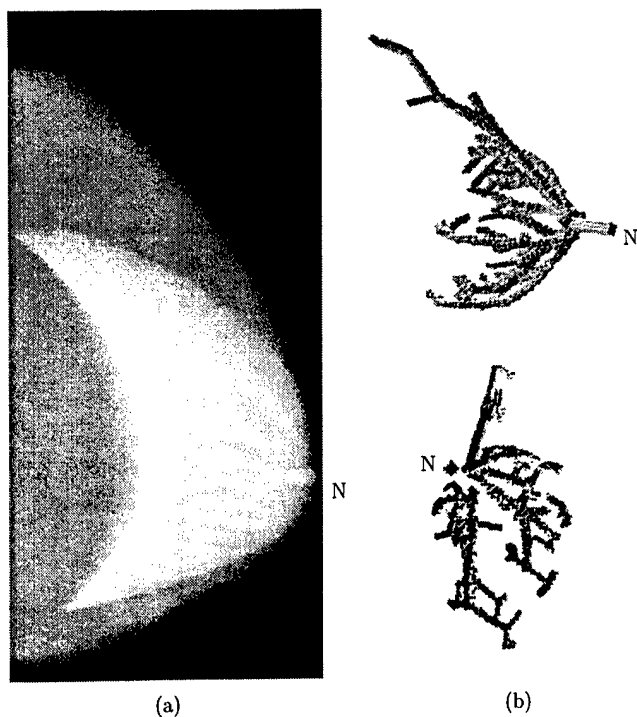


FIG. 6. Examples of computer generated ductal lobes. (a) A simulated mammogram with five duct lobes. For the purpose of this illustration, other medium scale image elements have been suppressed. (b) Two views of the same simulated ductal network, used to generate image in (a). (The letter "N" indicates position of the nipple.)

Fig. 4. Adipose compartments are more easily identified in a histologic slice than in a mammogram, since the latter image contains the superimposed projections of many tissue layers. Simulations of breasts with different sized adipose compartments are illustrated in Fig. 5. The procedure for generating simulated tissue compartments starts by filling the 3D breast phantom with compartments of the largest selected size until they start to intersect each other. The compartment size is then reduced and the procedure continued until the smallest selected size has been reached.

3. Modeling breast ductal network

To achieve a sufficiently realistic tissue phantom it is also necessary to model the breast ductal network. Ducts can be visualized by galactography, a clinical x-ray imaging procedure whereby the ducts are enhanced by injection of a contrast agent. The breast ductal system consists of about 15–20 ductal lobes, each corresponding to a major duct branching from the nipple into a network of smaller ducts. In galactograms, usually a single lobe is enhanced. Larger ducts are more visible than the smaller ones, since they attenuate more x rays.

The main focus of our model is on the pattern of duct branching. This pattern can be expressed by a ramification matrix, representing probabilities of branching at different levels of a tree structure.¹⁹ There are no previous reports in the literature on analyzing the breast ductal network by ramification matrices. The class of random binary trees was cho-

sen for modeling the ducts since it offers the least constrained branching pattern.¹⁹ The ductal model consists of 15 lobes and each lobe is simulated by a different random binary tree. Different trees are generated by using different random number generator seeds. A simulated ductal network is shown in Fig. 6. For clarity, only 5 out of 15 lobes are visible.

B. Mammographic compression model

The mammographic compression simulation is based upon a deformation model including realistic tissue elasticity properties. Elasticity parameters of the tissue found in the literature vary significantly.^{20–22} One of the reasons for these variations is that the experiments for determining the elastic properties have been performed using small samples taken from a particular tissue type (e.g., adipose, fibroglandular, or cancerous). However, the breast is comprised of a complicated admixture of different tissues which affect the elastic behavior of the whole organ.

The parameters most often used for description of elastic properties are the Young's linear elasticity modulus, E , and the Poisson's ratio, ν , defined by

$$E = \frac{\sigma}{\epsilon} = \frac{F/A}{\Delta l/l}, \quad \nu = \frac{\Delta w}{\Delta l}. \quad (1)$$

The Young's modulus relates the strain, ϵ , as a measure of deformation (i.e., the fractional change in length $\Delta l/l$) and the stress, σ (the force F applied to the surface area A of the deformed object). The Poisson ratio, ν , is equal to the ratio of transverse contraction, Δw , to the elongation, Δl , of a deformed bar. It is usually assumed that human tissue can be approximated as an incompressible material, whose volume does not change during deformation.²⁰ For incompressible materials $\nu \approx 0.5$.

The other elasticity moduli used to describe the behavior of material are the bulk modulus, K , and shear modulus, G , which can be expressed using the values of E and ν :

$$K = \frac{E}{3(1-2\nu)}, \quad G = \frac{E}{2(1+\nu)}. \quad (2)$$

There is a relationship between the bulk elasticity modulus, K , material density, ρ , and the speed of sound through the material, v , given by

$$v \approx \sqrt{K/\rho}. \quad (3)$$

In the compression model, the elasticity parameter values of adipose and fibroglandular tissues were computed using the values of ultrasound velocity through various tissues found in the literature.²³

The Mammography Quality Standards Act²⁴ regulates the minimum and maximum breast compression to be used in mammography. In general, the mammography technician will apply the maximum force tolerated by the patient to achieve optimum quality mammograms. Sullivan *et al.*²⁵ reported a statistical analysis of the compression force and compressed breast thickness, measured during 560 exams. Simulated force values were selected to address these considerations.

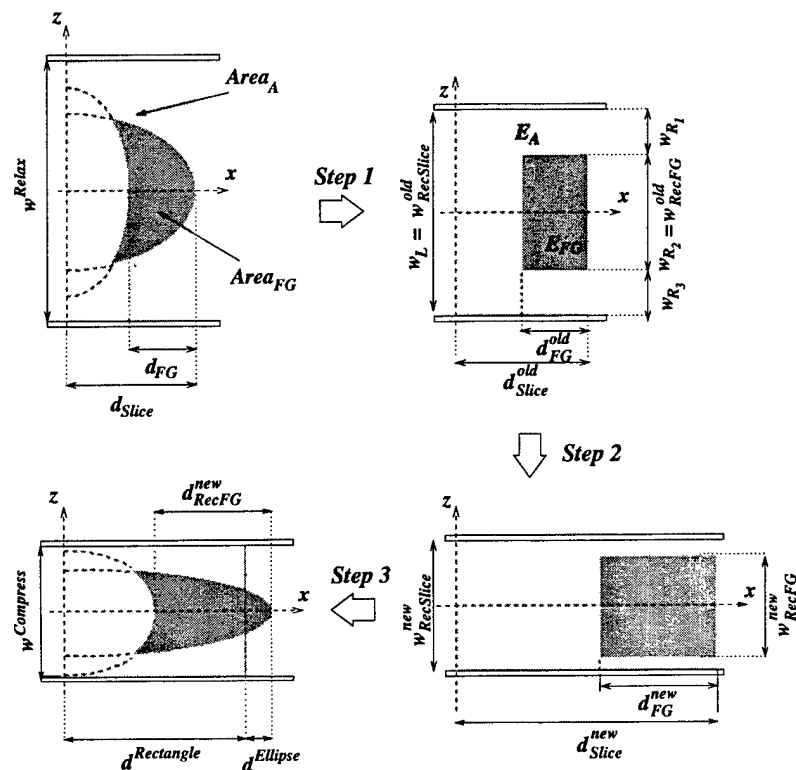


FIG. 7. Separate deformation of breast model slices. Illustrated are the steps of rectangular slice approximation, deformation of the approximated slice, and generation of the final shape of the deformed slice. These steps are followed by stacking all compressed slices together to generate the compressed breast shape (not shown).

There are very few published results about deformation of breast tissue structures during mammography. One reason is that it is hard to provide 3D visualization of such deformations. Clinically available 3D breast imaging techniques, ultrasound and MRI, have lower resolution and poorer quality than mammography. In addition, both methods use much less compression and are not applicable for analyzing tissue deformation during mammography. In our compression model, tissue deformation is estimated in two phases. First, the large scale model elements, the AT and FGT regions, are deformed to determine the shape of the compressed breast. Second, the medium scale model elements are deformed by transforming the shells and spheres into ellipsoids. After compression and x-ray image acquisition, the medium scale elements appear as elliptical structures in synthetic mammograms corresponding to the oval shaped lucencies seen in real mammograms.

The compression of large scale model elements is simulated in the form of separate deformations of the breast tissue slices, positioned normal to the compression plates. In this paper, the medio-lateral oblique (MLO) mammographic view is modeled since it provides visualization of more breast tissue than other views.²⁶ Moreover, in a number of countries, e.g., UK, the Netherlands, and Sweden, it is the only view obtained by breast screening.²⁷ Compression for other views, e.g., cranio-caudal (CC), can be simulated by a modification of the described model. In the case of MLO compression, tissue slices are positioned normal to the MLO view plane. In this case, a slice appears as a semiellipse, and the FGT portion of the slice appears as the intersection of two semiellipses, as shown in Fig. 3. Slice thickness corresponds to the model resolution specified at the beginning of the simulation.

Deformation of each slice is computed in three steps. First, a rectangular slice approximation is computed. Second, slice deformations are estimated using a composite beam model. Third, the compressed slice shape is computed from the deformed rectangular approximation. Compressed slices are stacked together to form the compressed breast model shape. A detailed description of the processing steps is given in the following.

1. Rectangular slice approximation

A slice of the breast model is replaced by its rectangular approximation. The whole slice region and its FGT portion are approximated by rectangles, satisfying the following constraints: (i) the area of the rectangular slice approximation, A_{Slice} , and area of the rectangular FGT approximation, A_{FG} , are the same as the corresponding areas in the original slice; (ii) the side of the rectangular slice approximation in the chest-nipple direction, d_{Slice} , and the side of the rectangular FGT approximation in the same direction, d_{FG} , are equal to the corresponding dimensions in the original slice; and (iii) the distance between the centers of gravity of the rectangular slice approximation and the rectangular FGT approximation is the same as the corresponding distance in the original slice. This constraint is not used for deformation of the slice through the nipple, because it may produce a rectangular approximation of the FGT region protruding outside of the slice. Instead, the FGT region is positioned so that it touches the nipple side of the rectangular approximation of the whole slice.

Using these constraints, the dimensions and relative positions of the rectangular slice and FGT approximation are

computed. An example of a slice through the nipple is illustrated in Fig. 7.

2. Slice deformation via a composite beam model

The approximating rectangles preserve the elastic properties of the corresponding slice regions. The elastic properties of the AT and FGT regions are modeled by linear Young's moduli, E_A and E_{FG} , respectively. This rectangular slice approximation can be treated as a composite 2D elastic beam, positioned between two bars corresponding to slices through the compression plates. Deformation is estimated by applying a force to the compression plates which in turn deforms the composite beam. It is assumed that (i) the slice thickness is much smaller than the sides of the approximating rectangles and (ii) during the compression, the slice stays in the same plane as before compression. The latter assumption is based on the fact that in reality slices of tissue are not compressed independently; the neighboring tissue (above or below) partially confine the slice to a plane. Slices in the planes above or below the nipple level do not have initial contact with the compression plates. It is assumed that all slices deform with the same strain value which is equal to the strain of the slice in the nipple level:

$$\epsilon_{\text{Slice}} = \epsilon_{\text{Slice}}^{\text{Nipple}} = \frac{\Delta w_{\text{RecSlice}}}{w_{\text{RecSlice}}} = 1 - \frac{w_{\text{RecSlice}}^{\text{new}}}{w_{\text{RecSlice}}^{\text{old}}} = 1 - \frac{w^{\text{Compress}}}{w^{\text{Relax}}}, \quad (4)$$

where ϵ_{Slice} and $\epsilon_{\text{Slice}}^{\text{Nipple}}$ represent strain for any slice and strain for the slice in the nipple level, respectively; $w_{\text{RecSlice}}^{\text{old}}$ and $w_{\text{RecSlice}}^{\text{new}}$ represent size of the rectangular approximation normal to the compression plates, before and after compression, respectively; w^{Relax} and w^{Compress} represent breast thickness before and after compression, respectively. The intensity of the compression force is included indirectly, by specifying the thickness of the compressed breast. Since a linear model of tissue elasticity is used, only the ratio of Young's moduli for the AT and FGT region is needed to estimate slice deformation.

The stress in the rectangular FGT region, σ_{R_2} , is the same as the stresses σ_{R_1} and σ_{R_3} in the parts of the rectangular AT region with thickness w_{R_1} and w_{R_3} ,

$$\sigma_{R_1} = \sigma_{R_2} = \sigma_{R_3}. \quad (5)$$

Replacing σ_i by $E_i \epsilon_i$, from Eq. (1), the strain in the rectangular FGT approximation is calculated as:

$$\epsilon_{R_2} = \frac{E_A}{E_{FG}} \epsilon_{R_1}. \quad (6)$$

The ratio E_A/E_{FG} is computed based upon the relationship between the bulk elastic moduli, tissue density, and velocity of sound propagation through the tissue. Measured values of the velocity of sound in samples of adipose and fibroglandular tissue are $v_A=1470$ m/s and $v_{FG}=1545$ m/s, respectively.²³ Densities of the adipose and fibroglandular tissue are $\rho_A=930$ kg/m³ and $\rho_{FG}=1040$ kg/m³, respectively.²⁸ Using Eq. (3), gives

$$\frac{E_A}{E_{FG}} \approx \frac{K_A}{K_{FG}} \approx \frac{\rho_A v_A^2}{\rho_{FG} v_{FG}^2} = 0.81. \quad (7)$$

Finally, there is a relationship between the strains in different parts of the rectangular slice approximation, since:

$$\Delta w_L = \Delta w_{R_1} + \Delta w_{R_2} + \Delta w_{R_3}, \quad (8)$$

which after dividing by w_L and using the fact that $\epsilon_{R_1} = \epsilon_{R_3}$ due to symmetry, yields

$$\epsilon_L = \epsilon_{R_1} \frac{w_{R_1} + w_{R_3}}{w_L} + \epsilon_{R_2} \frac{w_{R_2}}{w_L}. \quad (9)$$

Equations (4), (6), and (9) yield dimensions of the rectangular slice and FGT region normal to the compression plates after the compression, $w_{\text{RecSlice}}^{\text{new}}$ and $w_{\text{RecFG}}^{\text{new}}$, respectively:

$$w_{\text{RecSlice}}^{\text{new}} = w_L(1 - \epsilon_L), \quad w_{\text{RecFG}}^{\text{new}} = w_{R_2}(1 - \epsilon_{R_2}). \quad (10)$$

Assuming that the areas of the rectangular slice and FGT region, A_{Slice} and A_{FG} , stay the same before and after compression, we can compute the dimension of the rectangular slice and FGT approximation in the chest-nipple direction after compression, $d_{\text{RecSlice}}^{\text{new}}$ and $d_{\text{RecFG}}^{\text{new}}$, respectively:

$$d_{\text{RecSlice}}^{\text{new}} = \frac{A_{\text{Slice}}}{w_{\text{RecSlice}}^{\text{new}}}, \quad d_{\text{RecFG}}^{\text{new}} = \frac{A_{FG}}{w_{\text{RecFG}}^{\text{new}}}. \quad (11)$$

3. Compressed slice from the deformed rectangular approximation

The final step of the slice deformation modeling is the computation of the compressed breast slice from its deformed rectangular approximation. The compressed breast does not have an ellipsoidal but rather a flattened shape.^{26,29} The thickness of the compressed breast is constant and equal to the distance between the compression plates, w^{Compress} , everywhere except in a narrow region close to the front edge of the breast. Analysis of that region on a mammogram was used to estimate the breast thickness directly from mammograms.³⁰ To achieve a realistic shape of the compressed breast slice, a correction was applied to the model.³¹ This correction assumes that the deformed breast slice consists of a rectangle positioned at the chest wall side, and a semiellipse attached to the rectangle, extending forward to the nipple (see Fig. 7).

Parameters of the deformed rectangle and semiellipse are computed satisfying the following constraints: (i) the sum of the rectangular area, $A^{\text{Rectangle}}$, and the semielliptical area, A^{Ellipse} , is equal to the area of the whole uncompressed slice, A_{Slice} ; (ii) one side of the rectangle and one axis of the semiellipse are equal to the distance between the compression plates for the compressed breast, w^{Compress} ; and (iii) the slice region where the thickness is less than w^{Compress} contains 10% of the whole mammogram breast area.³⁰ The described correction for flattening the compressed breast is

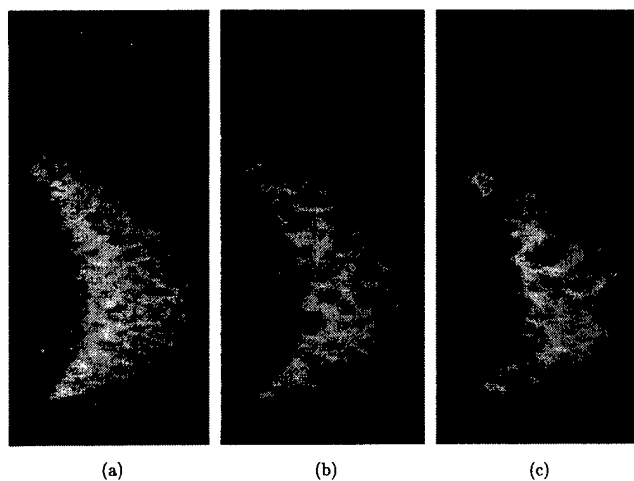


FIG. 8. Examples of synthetic images with different sizes of tissue model elements (i.e., simulated compartments in the AT and FGT), which are used for comparison with clinical mammograms. The images are labeled according to Table I as: (a) "Small," (b) "Medium," and (c) "Large."

only used to determine the border of the whole compressed slice. Deformation of the FGT region is still computed using the 2D composite beam approximation.

Separate processing of individual model slices is followed by stacking the deformed slices together to get the 3D compressed breast model. Slices whose relaxed (noncompressed) thickness is less than the compressed breast thickness are not processed at all; they are assumed to preserve their relaxed shape. The compressed breast thickness was used instead of the compression force to compute the deformation of the breast model slices. The compression force can be calculated from the difference of the relaxed and compressed breast thickness and tissue elastic moduli using Hooke's law. When computing the force, the values for both the elastic moduli of the adipose and fibroglandular tissue are needed.

C. X-ray mammogram acquisition model

The x-ray image acquisition model consists of an x-ray propagation model, which includes attenuation by the breast tissue and conversion of the x-ray energy into film density, and a model of mammographic film digitization. In the case of digital mammography, the film and digitization models should be replaced by a model of a solid-state x-ray detector array. The model is adopted from the literature,¹⁰ and for simplicity assumes a monoenergetic x-ray spectrum and a parallel beam geometry, without scatter.

The mammogram acquisition model relates the spatial distribution of the x-ray energy imparted to the intensifying screen, E_I , to the mammogram digital values (after digitization), DV, and the linear x-ray attenuation coefficient of tissue, μ_t :

$$E_I(x,y) = \eta \phi E C \exp \left\{ - \int_{z=0}^{z=w^{\text{Compress}}} \mu_t(x,y,z) dz \right\}, \quad (12)$$

$$DV(x,y) = a - b \gamma \log_{10} \{ \beta E_I(x,y) \}, \quad (13)$$

TABLE I. Radii of simulated adipose compartments in the AT and FGT, used to generate the synthetic mammograms.

Structure radii	Model regions	
	AT (mm)	FGT (mm)
Small	2.7–6.7	1.3–2.7
Medium	4–10	2–4
Large	5.3–13.3	2.7–5.3

where η represents the quantum efficiency of the screen, ϕ is the fluence at the entrance to the breast, E the x-ray photon energy, C is the attenuation factor due to the compression paddle and grid, w^{Compress} is the compressed breast thickness, a and b are digitization coefficients, and γ and β are the film gamma and the speed coefficient, respectively. It is assumed that the digitization output is proportional to optical density, thus Eqs. (12) and (13) can be simplified so that DV is linearly proportional to the ray sum. The linear x-ray attenuation coefficients of the AT and FGT tissue, taken from the literature,³² are $\mu_{\text{AT}} = 0.456 \text{ cm}^{-1}$ and $\mu_{\text{FGT}} = 0.802 \text{ cm}^{-1}$, at 20 keV. Further details of the acquisition model are given in the literature.³³

III. SIMULATION RESULTS AND DISCUSSION

Figure 8 shows three synthetic mammograms generated by our simulation. These three images differ in the size of the simulated medium scale tissue structures. The ranges of adipose compartments radii simulated in the mammograms (shown in Fig. 8) are given in Table I.

It can be noted that the proportions of the breast model, i.e., vertical to horizontal dimension ratio after compression, agree with the "standard breast" from Novak,²⁹ defined by averaging dimensions of 27 compressed breasts. Dimensions of the breast model are smaller than the "standard breast" by approximately 15%.

The synthetic mammograms were printed on film (AGFA LR5200, AGFA-Gevaert, Belgium) lifesizes, and were shown to radiologists in the Breast Imaging Center of Thomas Jefferson University. Qualitatively, subregions of synthetic and clinical images were reported to have similar appearance when viewed at a distance of 1–2 m. When examined closely, it was observed that the synthetic images lack blood vessels and other organized fine tissue structures. In addition, the borders between the AT and FGT regions in the synthetic mammograms appeared as a clear, geometrically regular separation degrading the subjective perception of reality. For the latter reason, the model was modified by addition of small random variations to the position of the borders between the compressed AT and FGT phantom regions. This correction is included in Fig. 8.

As stated in Sec. I, the model for producing the synthetic mammograms was based upon the hypotheses that the size and the distribution of simulated 3D tissue elements are similar to those found in the real breasts, and that the 3D tissue distribution is reflected in the distribution of 2D mammographic structures. In order to evaluate the synthetic images,

we performed statistical comparisons of several texture descriptors computed in synthetic and clinical mammograms, including: average size of image objects, texture energy, and fractal dimension. These descriptors have been previously used in the literature for the analysis of parenchymal patterns in mammograms.^{34–36} The image objects' size, analyzed using mathematical morphology, can be related to the size of the simulated 3D tissue structures. Texture energy and fractal dimension are sensitive to small scale changes in image intensities, corresponding to fine tissue detail. Details about the texture analysis of synthetic and clinical mammograms are given in the accompanying paper.¹⁷ Quantitatively, the synthetic mammograms have a similar distribution of values averaged over a large number of clinical mammograms. The best matching was observed for the synthetic images generated using the simulated adipose compartments with radii of 4–13.3 mm in the AT regions, and radii of 2.7–5.33 mm and 1.3–2.7 mm in the retroareolar and dense FGT regions, respectively.¹⁷ It is expected that the introduction of detailed tissue structures in the breast model will enhance the local variations of synthetic mammograms and the variations in feature distribution needed to better match real images. In addition, the simulated ducts and the compression model were separately evaluated and compared with clinically acquired data.^{33,37}

IV. CONCLUSIONS

A method is described for generating synthetic mammograms using simulations of breast tissue and the mammographic imaging process. A software breast phantom was developed, which contains realistic large and medium scale tissue structures, derived from an understanding of the macroscopic anatomic tissue organization. Parameters controlling the size and placement of the tissue simulating structures provide flexibility to generate a large database of synthetic images with different characteristics. Mammographic imaging is simulated using a compression model and a model of the x-ray image acquisition. The compression model estimates breast deformation using tissue elasticity parameters found in the literature and realistic values of compression force. The synthetic mammograms were generated by a mammogram acquisition model using a monoenergetic parallel beam approximation, applied to the synthetically compressed breast phantom.

The proposed simulation can be used in analysis of breast positioning, compression, and image acquisition parameters. The software breast phantom can be used as a test object for optimizing mammographic systems or testing novel systems for 3D reconstruction of breast images. The simulation can be used for analyzing the correlation between the 3D breast composition and 2D mammogram characteristics, e.g., the parenchymal patterns, which can be used for estimation of the cancer risk.³⁸ Computer algorithms for characterization of normal breast tissue could be tested on large databases of normal images with random variations of tissue structures, generated by the model. Synthetic mammograms with simulated abnormalities or abnormalities extracted from clinical

mammograms could be used for testing algorithms for cancer detection.

ACKNOWLEDGMENTS

This work was supported in part by NSF Grant No. IRI-9504363 and by US Army Breast Cancer Research Program Grant Nos. DAMD 17-96-1-6128 and DAMD 17-98-1-8169. The authors would like to thank Dr. Robert D. Cardiff, University of California, Davis, for providing the images of breast subgross histology specimens.

^{a)} Author to whom all correspondence should be addressed; electronic mail: Andrew.Maidment@mail.tju.edu

¹ J. P. Rolland and H. H. Barrett, "Effect of random background inhomogeneity on observer detection performance," *J. Opt. Soc. Am. A* **9**, 649–658 (1992).

² F. O. Bochud, J.-F. Valley, F. R. Verdun, C. Hessler, and P. Schnyder, "Estimation of the noisy component of anatomical background," *Med. Phys.* **26**, 1365–1370 (1999).

³ A. E. Burgess, F. L. Jacobson, and P. F. Judy, "Human observer detection experiments with mammograms and power-law noise," *Med. Phys.* **28**, 419–437 (2001).

⁴ J. Hsu, D. M. Chelberg, C. F. Babbs, Z. Pizlo, and E. Delp, "Preclinical ROC studies of digital stereomammography," *IEEE Trans. Med. Imaging* **14**, 318–327 (1995).

⁵ M. M. Goodsitt, H.-P. Chan, and L. Hadjiiski, "Stereomammography: Evaluation of depth perception using a virtual 3D cursor," *Med. Phys.* **27**, 1305–1310 (2000).

⁶ P. R. Bakic, M. Albert, and A. D. A. Maidment, "Dose requirements in stereoradiography," in *Physics of Medical Imaging*, edited by L. E. Antonuk and M. J. Yaffe [Proc. SPIE **4682**, 126–137 (2002)].

⁷ L. T. Niklason et al., "Digital tomosynthesis in breast imaging," *Radiology* **205**, 399–406 (1997).

⁸ A. D. A. Maidment, M. Albert, and E. F. Conant, "Three-dimensional imaging of breast classifications," in *Exploiting New Image Sources and Sensors*, edited by J. M. Selander [Proc. SPIE **3240**, 200–208 (1997)].

⁹ K. Doi and H.-P. Chan, "Evaluation of absorbed dose in mammography," *Radiology* **135**, 199–208 (1980).

¹⁰ R. P. Highnam, J. M. Brady, and B. J. Shepstone, "Computing the scatter component of mammographic images," *IEEE Trans. Med. Imaging* **13**, 301–313 (1994).

¹¹ F. O. Bochud, C. K. Abbey, and M. P. Eckstein, "Statistical texture synthesis of mammographic images with clustered lumpy backgrounds," *Opt. Express* **4**, 33–43 (1999).

¹² H. D. Li, M. Kallergi, L. P. Clarke, V. K. Jain, and R. A. Clark, "Markov random field for tumor detection in digital mammography," *IEEE Trans. Med. Imaging* **14**, 565–576 (1995).

¹³ J. J. Heine, S. R. Deans, R. P. Velthuisen, and L. P. Clarke, "On the statistical nature of mammograms," *Med. Phys.* **26**, 2254–2265 (1999).

¹⁴ P. Bakic, D. Brzakovic, and Z. Zhu, "Anatomic segmentation of mammograms via breast model," in *Digital Mammography Nijmegen, 1998*, Proceedings of the Fourth International Workshop on Digital Mammography, Nijmegen, The Netherlands, June 1998, edited by N. Karssemeijer, M. Thijssen, J. Hendriks, and L. van Erning (Kluwer Academic, Dordrecht, 1998), pp. 291–294.

¹⁵ Y. Kita, R. Highnam, and M. Brady, "Correspondence between different view breast x-rays using a simulation of breast deformation," Proceedings of the IEEE Computer Vision and Pattern Recognition Conference, Santa Barbara, CA, June 1998, pp. 700–707.

¹⁶ A. Samani, J. Bishop, E. Ramsey, and D. B. Plewes, "A 3-D contact problem finite element model for breast shape deformation derived from MRI data," Proceedings of the 23rd Annual Meeting of the American Society of Biomechanics, Pittsburgh, October 1999.

¹⁷ P. R. Bakic, M. Albert, D. Brzakovic, and A. D. A. Maidment, "Mammogram synthesis using 3D simulation. II. Evaluation of synthetic mammogram texture," *Med. Phys.* **29**, 2140–2151 (2002).

¹⁸ J. Suckling et al., "The Mammographic Image Analysis Society Digital Mammogram Database," in *Digital Mammography*, Proceedings of the Second International Workshop on Digital Mammography, York,

- England, 10–12 July 1994, edited by A. G. Gale, S. M. Astley, D. R. Dance, and A. Y. Cairns (Elsevier Science, Amsterdam, 1994), p. 375–378 (<http://www.wiau.man.ac.uk/services/MIAS/MIASmini.html>)
- ¹⁹X. G. Viennot, G. Eyrolles, N. Janey, and D. Arques, “Combinatorial analysis of ramified patterns and computer imagery of trees,” *Comput. Graph.* **23**, 31–40 (1989).
- ²⁰A. P. Sarvazyan, A. R. Skorovoda, S. Y. Emelianov, J. B. Fowlkes, J. G. Pipe, R. S. Adler, R. B. Buxton, and P. L. Carson, “Biophysical bases of elasticity imaging,” in *Acoustic Imaging*, edited by J. P. Jones (Plenum, New York, 1995), pp. 223–240.
- ²¹F. S. Azar, D. Metaxas, and M. D. Schnall, “A finite model of the breast for predicting mechanical deformations during interventional procedures,” Proceedings of the International Symposium on Magnetic Resonance in Medicine, Philadelphia, PA, May 1999.
- ²²A. Samani, J. Bishop, E. Ramsey, and D. B. Plewes, “Breast tissue deformation finite element modeling for MRI/x-ray mammography data fusion,” in *Digital Mammography, IWDM 2000, Toronto, Canada*, Proceedings of the Fifth International Workshop on Digital Mammography, edited by M. J. Yaffe (Medical Physics Publishing, Madison, WI, 2001), pp. 763–769.
- ²³G. Kossoff, E. K. Fry, and J. Jellins, “Average velocity of ultrasound in the human female breast,” *J. Acoust. Soc. Am.* **53**, 1730–1736 (1973).
- ²⁴ACR Committee on Quality Assurance in Mammography, *Mammography Quality Control Manual* (American College of Radiology, Reston, VA, 1999).
- ²⁵D. C. Sullivan, C. A. Beam, S. M. Goodman, and D. L. Watt, “Measurement of force applied during mammography,” *Radiology* **181**, 355–357 (1991).
- ²⁶G. W. Eklund and G. Cardenosa, “The art of mammographic positioning,” *Radiol. Clin. North Am.* **30**, 21–53 (1992).
- ²⁷B. Lundgren and S. Jakobsson, “Single view mammography,” *Cancer* **38**, 1124–1129 (1976).
- ²⁸G. R. Hammerstein et al., “Absorbed radiation dose in mammography,” *Radiology* **130**, 485–491 (1979).
- ²⁹R. Novak, “Transformation of the female breast during compression at mammography with special reference to the importance for localization of a lesion,” *Acta Radiol., Suppl.* **371**, 7–46 (1988).
- ³⁰R. Highnam, M. Brady, and B. Shepstone, “Estimating compressed breast thickness,” in *Digital Mammography Nijmegen, 1998*, Proceedings of the Fourth International Workshop on Digital Mammography, Nijmegen, The Netherlands, June 1998, edited by N. Karssemeijer, M. Thijssen, J. Hendriks, and L. van Erning (Kluwer Academic, Dordrecht, 1998), pp. 275–278.
- ³¹P. Bakic and D. Brzakovic, “Simulation of digital mammogram acquisition,” in *Physics of Medical Imaging*, edited by J. M. Boone and J. T. Dobbins III [Proc. SPIE **3659**, 866–877 (1999)].
- ³²P. C. Johns and M. Yaffe, “X-ray characterization of normal and neoplastic breast tissue,” *Phys. Med. Biol.* **32**, 675–695 (1987).
- ³³P. R. Bakic, “Breast tissue description and modeling in mammography,” Ph.D. dissertation, Lehigh University, Bethlehem, PA, 2000.
- ³⁴S. Behrens and J. Dengler, “Analyzing the structure of medical images with morphological size distributions,” Proceedings of the Tenth International Conference on Pattern Recognition, Atlantic City, NJ, June 1990, pp. 886–890.
- ³⁵P. I. Miller and S. M. Astley, “Classification of breast tissue by texture analysis,” *Image Vis. Comput.* **10**, 277–282 (1992).
- ³⁶C. B. Caldwell, S. J. Stapleton, D. W. Holdsworth, R. A. Jong, W. J. Weiser, G. Cooke, and M. J. Yaffe, “Characterization of mammographic parenchymal pattern by fractal dimension,” *Phys. Med. Biol.* **35**, 235–247 (1990).
- ³⁷P. R. Bakic, M. Albert, and A. D. A. Maidment, “Evaluation of breast ductal networks using ramification matrices,” in *IWDM 2002*, Proceedings of the Sixth International Workshop on Digital Mammography, Bremen, Germany, June 2002.
- ³⁸J. W. Byng, M. J. Yaffe, R. A. Jong, R. S. Shumak, G. A. Lockwood, D. L. Trichler, and N. F. Boyd, “Analysis of mammographic density and breast cancer risk from digitized mammograms,” *Radiographics* **18**, 1587–1598 (1998).

Medical Physics

AVAILABLE ONLINE—See <http://www.medphys.org>

September 2002

Volume 29, Number 9

Mammogram synthesis using a 3D simulation. II. Evaluation of synthetic mammogram texture

Predrag R. Bakic and Michael Albert

Department of Radiology, Thomas Jefferson University, Suite 3390, Gibbon Building, 111 South 11th Street, Philadelphia, Pennsylvania 19107-5563

Dragana Brzakovic

Office of Integrative Activities, National Science Foundation, Arlington, Virginia 22230

Andrew D. A. Maidment^{a)}

Department of Radiology, Thomas Jefferson University, Suite 3390, Gibbon Building, 111 South 11th Street, Philadelphia, Pennsylvania 19107-5563

pp. 2140-2151

Mammogram synthesis using a 3D simulation.

II. Evaluation of synthetic mammogram texture

Predrag R. Bakic and Michael Albert

Department of Radiology, Thomas Jefferson University, Suite 3390, Gibbon Building, 111 South 11th Street, Philadelphia, Pennsylvania 19107-5563

Dragana Brzakovic

Office of Integrative Activities, National Science Foundation, Arlington, Virginia 22230

Andrew D. A. Maidment^{a)}

Department of Radiology, Thomas Jefferson University, Suite 3390, Gibbon Building, 111 South 11th Street, Philadelphia, Pennsylvania 19107-5563

(Received 25 February 2002; accepted for publication 14 June 2002; published 27 August 2002)

We have evaluated a method for synthesizing mammograms by comparing the texture of clinical and synthetic mammograms. The synthesis algorithm is based upon simulations of breast tissue and the mammographic imaging process. Mammogram texture was synthesized by projections of simulated adipose tissue compartments. It was hypothesized that the synthetic and clinical texture have similar properties, assuming that the mammogram texture reflects the 3D tissue distribution. The size of the projected compartments was computed by mathematical morphology. The texture energy and fractal dimension were also computed and analyzed in terms of the distribution of texture features within four different tissue regions in clinical and synthetic mammograms. Comparison of the cumulative distributions of the mean features computed from 95 mammograms showed that the synthetic images simulate the mean features of the texture of clinical mammograms. Correlation of clinical and synthetic texture feature histograms, averaged over all images, showed that the synthetic images can simulate the range of features seen over a large group of mammograms. The best agreement with clinical texture was achieved for simulated compartments with radii of 4–13.3 mm in predominantly adipose tissue regions, and radii of 2.7–5.33 and 1.3–2.7 mm in retroareolar and dense fibroglandular tissue regions, respectively. © 2002 American Association of Physicists in Medicine. [DOI: 10.1118/1.1501144]

Key words: mammography simulation, 3D, synthetic mammograms, texture analysis

I. INTRODUCTION

We have proposed an approach to generate synthetic mammograms based upon a 3D simulation of mammography.¹ Synthetic mammographic texture is produced by projecting simulated 3D breast anatomic structures. In clinical images, the overlapped projections of normal anatomic tissue structures generate a background texture in mammograms which can mask the existing abnormalities or introduce false ones. The simulation can be used to optimize positioning, compression and acquisition in order to improve the visibility of the breast tissue, and to test new breast imaging modalities.

The proposed mammography simulation consists of three major components. First, a 3D software breast phantom contains two ellipsoidal regions of large scale tissue elements: predominantly adipose tissue (AT) and predominantly fibroglandular tissue (FGT) regions. Internal structures of these regions, namely the adipose compartments and breast ductal network, are approximated by realistically distributed medium scale phantom elements: shells filled with simulated adipose tissue and a synthetic ductal tree. Second, a compression model of the breast deformation occurring during a mammographic exam is based upon tissue elasticity properties. Deformation is simulated separately for layers of tissue positioned normal to the compression plates. Each slice is

approximated by a rectangular beam composed of AT and FGT regions. The slices are computationally deformed, assuming clinical values of the compression force. Deformed slices are stacked together to produce a model of the compressed breast. Third, mammogram image acquisition is modeled assuming monoenergetic x rays and a parallel beam geometry without scatter. Details of the simulation are given in the accompanying paper.¹

Ideally, each of the three components of the simulation should be evaluated separately by a 3D imaging technique. There is, however, a significant difference in tissue properties captured by the clinically available 3D breast imaging modalities (ultrasound and MRI) and mammography which is the focus of our simulation. Breast ultrasound and MRI also have different resolution and compression than mammography. With these issues in mind we have evaluated the tissue model indirectly, assuming that a relationship exists between the distribution of 3D breast tissue structures and the 2D parenchymal pattern. It is our hypothesis that the texture properties computed in synthetic and clinical images have similar distributions.

There are two approaches to mammogram synthesis found in the literature: (i) direct modeling of 2D distribution of pixels and (ii) simulation of 3D tissue distribution and the

mammographic imaging. Bochud *et al.*² modeled mammogram texture as a “clustered lumpy background” by random placement of “blob” clusters, visually resembling tissue appearance in mammograms. Synthetic images were evaluated by comparing their power spectra and statistical moments with the values from 32 clinical mammograms. Good agreement of the first and the second moments in clinical and synthetic images were observed, with similar statistical properties overall. Heine *et al.*³ modeled a mammogram as evolving from a process of passing a random field (colored noise) through a linear filter with a self-similar characteristic, based upon the analysis of 60 clinical mammograms. Such an approach can match some of the statistical properties of clinical images but cannot relate the 3D tissue structures and their mammographic appearance. Both papers do not model breast ducts or the large scale tissue regions. Consequently, the images of the same simulated breast, with modified positioning, compression, or x-ray parameters cannot be consistently synthesized.

Taylor *et al.*⁴ generated synthetic images by mammography simulation, in an approach similar to our work. The focus of their simulation is on modeling breast ducts based upon the fractal properties of the duct length and diameter. They have evaluated the synthetic images so obtained by comparing the Fourier spectrum with that computed in images of tissue slices with contrast enhanced ducts. Good agreement using a small number of samples was observed.

Separate evaluations were performed for the simulation of the ductal network, the compression model, and the synthetic parenchymal pattern. Initial feasibility tests of the ductal model and compression simulation are presented elsewhere.^{5,6} This paper describes the analysis of the synthetic mammogram texture.

Synthetic images were generated by simulating the x-ray image acquisition on a computationally compressed phantom. Images of the phantoms were generated containing different sizes of simulated medium scale elements: spherical shells and blobs. The synthetic mammograms, so obtained, were evaluated by comparing them with clinical images taken from the MIAS database of digitized mammograms.⁷ Subimages taken from regions corresponding to different tissues were compared separately, including the subcutaneous AT, retromammary AT, retroareolar FGT, and dense FGT regions. Three texture features were used for description of the parenchymal pattern: (i) the average size of image structures

computed using mathematical morphology, (ii) the texture energy, and (iii) the fractal dimension. Feature values were computed over each clinical and synthetic subimage and statistically compared using the Kolmogorov–Smirnov test and histogram correlation. Details of the analysis of synthetic and clinical mammographic texture are given in Sec. II and the results of the comparison are discussed in Sec. III.

II. TEXTURE ANALYSIS OF SYNTHETIC MAMMOGRAMS

A. Texture descriptors

The following texture descriptors were used for the evaluation of synthetic mammogram texture. First, size analysis was performed by a sequence of morphological closings with disks of increasing size as structuring elements.⁸ Average image brightness increases after the closing operation. The change in brightness as a function of the disk radius is related to the size distribution of radiolucent (adipose) areas in the mammograms. Second, texture energy analysis was performed by convolving each image with a small mask.⁹ Treating gray scale image intensity as the height of a 3D object, this mask is sensitive to local roughness of the image surface. Third, fractal dimension was computed by the blanket box counting method of self-similarity analysis.¹⁰

1. Morphological analysis of image structure size

Morphological image analysis is based upon the shape of image objects and is used to simplify image data while preserving shape characteristics. The theory of mathematical morphology is discussed in the books of Matheron¹¹ and Serra.⁸ An application oriented tutorial of morphological image processing is given by Haralick.¹²

Morphological operations are performed on a set of image pixels using a second set of pixels called the structuring element. Definitions of the basic operations are given in the Appendix. The opening operation is used for size analysis of bright objects, and closing for the analysis of dark objects. This analysis is sensitive to the radiolucent areas of the mammogram, corresponding to the adipose tissue which appears darker than the surrounding tissue. X rays are less attenuated by adipose tissue, producing greater film density than connective tissue.

The gray scale closing first replaces each pixel with the maximum from its neighborhood defined by the structuring element (a disk). The original values are then recovered for all of the pixels, except for those from regions which are both darker than their surroundings and smaller than the structuring element. As an illustration, Fig. 1(a) shows an image with several objects of different size. After the closing operation with the structuring element from Fig. 1(b), the resulting image is given in Fig. 1(c). It can be seen that dark objects smaller than the structuring element have been eliminated; the resulting image is thus brighter than the original.

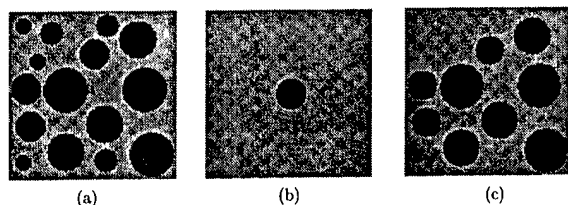


FIG. 1. Illustration of morphological closing. (a) The original image with objects of different size. (b) The image of the structuring element. (c) The resulting image obtained by the morphological closing with the structuring element from (b) applied to the image from (a).

This is the basis for morphological size analysis, whereby the change in average image brightness (i.e., the total pixel sum after the closing) is used to describe the size distribution of the image objects. The derivative of the brightness as a function of size shows the contribution of the objects equal in size to the structuring element.

Morphological size analysis of mammograms has been reported previously in the literature.^{13,14} Behrens and Dengler¹³ reported examples of applying morphological size analysis at global, regional, and local image levels; analysis of calcifications was presented as a local processing. Miller and Astley¹⁴ used morphological size analysis to segment the FGT region from mammograms. They used the opening operation which is dual to closing; it replaces the bright regions smaller than the structuring element by their dark surrounding pixels. The overall image brightness is, thus, reduced. However, the authors did not analyze the relationship between morphological feature values and the physical properties of the anatomic structures. Our research represents a novel application of morphological image analysis as a result of using the simulated 3D tissue structures to synthesize parenchymal patterns.

2. Texture energy analysis

Texture energy features are the statistical estimates of the outputs from a filter bank implemented in the form of local linear transformations. They were introduced with the goal of achieving texture segmentation and description at each image pixel, corresponding to a hypothetical low level function of the human visual system.⁹ The filter bank consists of small 2D convolution masks whose coefficients are computed as the product of 1D masks with different numbers of zero crossings. Contrast invariance of the filter outputs is achieved by the normalization with the output of the filter sensitive to the average local image intensity. The absolute values or variances of the convolved images are used for analysis. A generalization of this approach can include a larger set of local linear transformations, and the estimation of higher order moments of the output channel histograms.¹⁵

In mammogram processing applications^{14,16} texture energy was usually computed using a single or a few convolution masks. The mask sensitive to image "ripple" was found to be the most efficient in segmenting potentially abnormal regions in mammograms, a task which is related to the local roughness of the image surface. Texture energy features have also been used in mammogram registration.^{17,18}

The mask coefficients are given in the Appendix. A 5×5 "ripple" convolution mask, R5R5 [Eq. (A2)], was used, capturing local roughness of the image surface. The absolute values of the convolved data were averaged on a 15×15 window and normalized by the "level" mask, L5L5 [Eq. (A2)], providing contrast invariance.

3. Fractal analysis

Fractal dimension describes self-similarity of image properties at different spatial scales. It is common to perform fractal analysis on the area of the image surface, obtained by

considering the pixel values as local surface heights. This area is related to the roughness of the image texture. A complete definition of the fractal dimension of image surface area is given in the Appendix.

There are numerous reports in the literature on fractal analysis of mammograms.^{19–22} Caldwell et al.¹⁹ analyzed the fractal dimension of various parenchymal patterns and the difference between the fractal dimensions computed over the whole image and within a region near the nipple. A feature space defined by these two fractal features was segmented and a relatively good agreement with the original Wolfe classification²³ was observed. Mammographic calcifications have been segmented using a variety of methods for computing fractal dimension, including box counting,²⁰ iterated function systems,²¹ and fractal Brownian motion.²²

We computed fractal dimension by the blanket algorithm.¹⁰ This method has been used previously in the detection of calcifications in mammograms.²⁰ The fractal dimension is computed for each pixel by analyzing the local image surface around the pixel. A 15×15 window was selected, centered on each pixel. This corresponds to the nonlinear averaging window size used in the texture energy method. A log-log plot of $A_{\text{local}}(\epsilon)$ is generated for the local surface around each pixel. The local fractal dimension value D_{local} is computed as the slope through three points on the log-log plot, corresponding to the scale parameter values of $\epsilon=2, 3,$ and 4 pixels.

B. Image selection

The following criteria were used for selection of the clinical and synthetic mammograms to be used for comparison. First, the clinical images had to represent normal breast tissue. Second, the glandularity seen in the mammograms should approximately represent the average breast glandularity (not too dense and not predominantly adipose). Third, spatial resolution of the clinical and synthetic mammograms should be matched. The clinical images were selected from the MIAS database⁷ of digitized mammograms and the synthetic mammograms were generated for varying properties of the medium scale elements, i.e., different sizes of simulated adipose compartments in the AT and FGT regions. In addition, the comparison was repeated for the same set of clinical and synthetic mammograms at a reduced resolution. The images with reduced resolution were generated by averaging 2×2 blocks of pixels from the original mammograms.

1. Clinical mammograms

Sixty-five mammograms from the Mini-MIAS database of clinical mammograms were used, having a spatial resolution of $200 \mu\text{m}/\text{pixel}$. The Mini-MIAS database was obtained by averaging 4×4 pixel blocks in the original MIAS mammogram database.⁷ This resolution is sufficient for the evaluation of our synthetic mammograms since presently they do not include fine, small scale tissue detail. The selected images represent normal cases in the MIAS database with the background tissue classified as "fatty-glandular." As the sizes of adipose compartments differ for various tissue regions, up to four $25 \text{ mm} \times 25 \text{ mm}$ subimages per mammo-

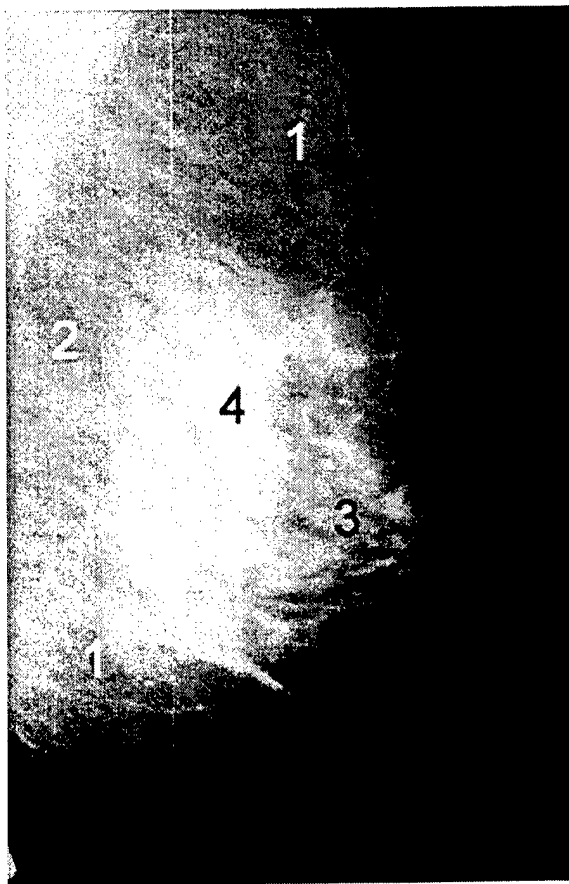


FIG. 2. Tissue regions used in texture analysis, illustrated on a clinical mammogram from the MIAS database: (1) subcutaneous adipose tissue, (2) retromammary adipose tissue, (3) retroareolar fibroglandular tissue (immediately posterior to the nipple), and (4) dense fibroglandular tissue.

gram were selected manually, giving a total of 219 subimages, from the following regions (see Fig. 2): (1) subcutaneous fat; (2) retromammary fat; (3) retroareolar glandular tissue, immediately posterior to the nipple; and (4) dense glandular tissue. If the extent of a tissue region could not be unambiguously determined, or if it was too small for a subimage window, the corresponding tissue sample was excluded from analysis.

2. Synthetic mammograms

Synthetic images were generated at a spatial resolution of 200 $\mu\text{m}/\text{pixel}$, matching that of the database. Four subimages per synthetic mammogram were selected from different regions in the same manner as for the clinical images. The positions of the subimages were determined from the known extent of the large scale model elements, the AT and FGT regions. Model parameters controlling the distribution of medium scale tissue structures, modeled by shells in the AT and spheres in the FGT regions, were varied to match the statistical properties of real images. Three groups of synthetic mammograms were tested. The groups consisted of ten synthetic mammograms each, generated randomly using the same range of size of simulated adipose tissue compart-

ments. The ranges of compartment sizes differed between the groups by 30% (see Table I and Fig. 8 in the accompanying paper¹).

C. Statistical comparison

Two methods were used for statistical comparison of the texture features. First, feature histograms were computed for each subimage. Synthetic histograms were then averaged over all subimages of the same tissue type and were compared with similarly computed clinical histograms. The correlation between the corresponding clinical and synthetic averaged histograms was used to measure how well the synthetic images approximated the clinical images. Next, mean feature values (i.e., the histogram first moments) were computed for each subimage. Distributions of these means for all subimages of the same tissue type were then analyzed and compared with the distributions of means of the clinical images, using the Kolmogorov–Smirnov (KS) test.²⁴ The maximum difference between the cumulative distribution functions (CDFs) of the clinical and synthetic mean feature values was used as another measure of quality of mammogram synthesis. In both methods the average texture features were compared, thereby testing the ability of the simulation to match the average properties of a large set of clinical mammograms, rather than simulating an image of a particular breast.

1. Analysis of feature histograms

As a measure of similarity between the real and synthetic feature distributions, the correlation between the feature histograms was calculated for each of the clinical and synthetic subimages, and averaged over all subimages of the same tissue type. In the case of size analysis, the correlation was computed between the brightness gradient (as a function of the structuring element radius) of clinical and synthetic images. In the following text, these derivative values are referred to as the “average histogram of the size analysis feature.”

The coefficient of correlation, R , between the real, h_R , and synthetic, h_S , histograms averaged over all subimages (in a given category) is computed as:

$$R(h_R, h_S) = \frac{\sum_i h_R(i) h_S(i)}{\sqrt{\sum_i [h_R(i)]^2 \sum_i [h_S(i)]^2}}, \quad (1)$$

where the summation runs over histogram bins i .

2. Kolmogorov–Smirnov (KS) test

The KS test compares two random distributions based upon the maximum difference between their CDFs.²⁴ It belongs to a group of nonparametric methods which make no assumptions about the types of distributions used. The maximum difference between two CDFs, D , is a measure of the discrepancy between the two sets of samples. Kolmogorov showed that for two sets of samples with the same parent distribution, the CDF of D is given asymptotically by:²⁴

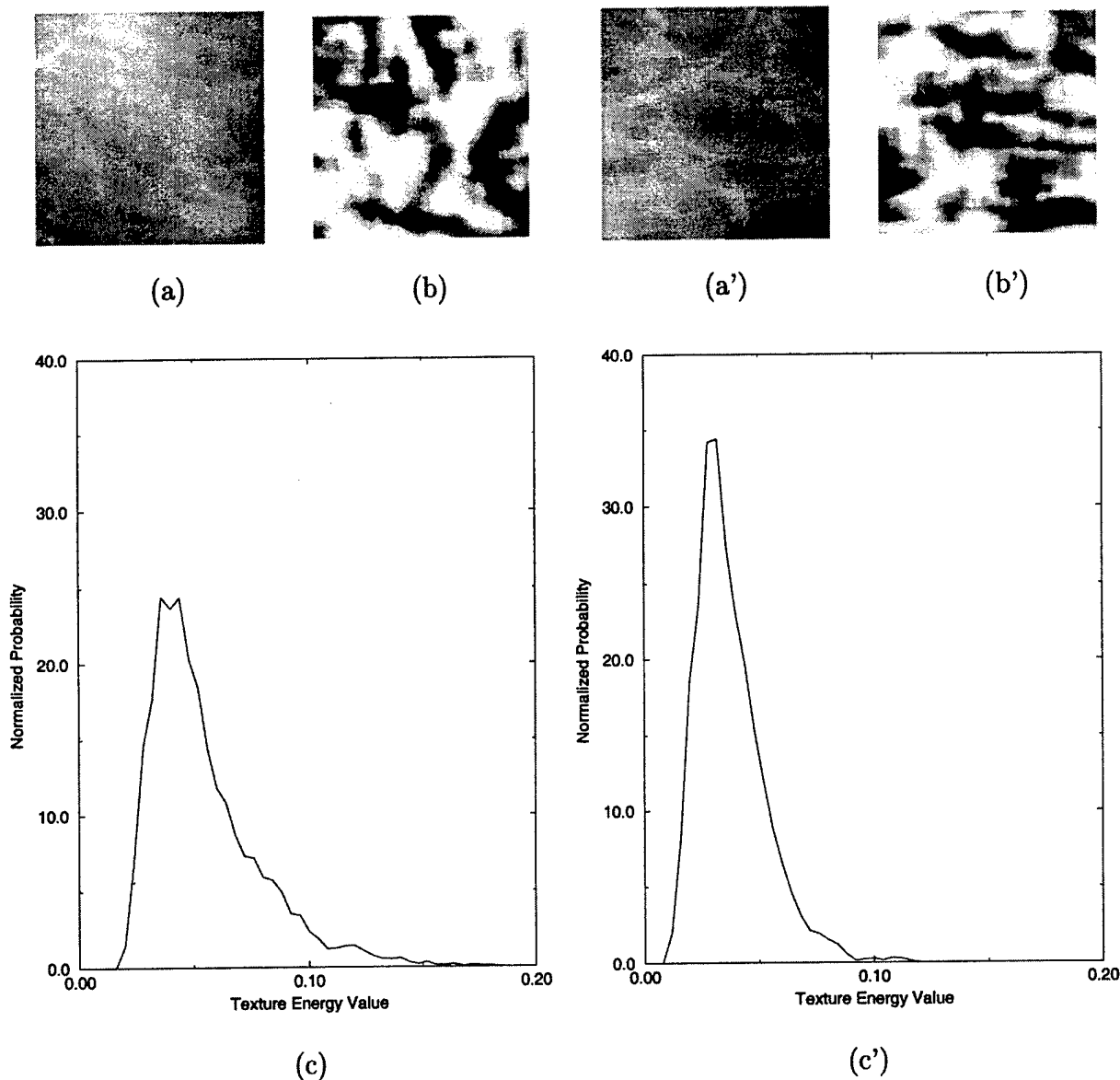


FIG. 3. Texture energy histograms of the FGT from clinical (left) and synthetic (right, primed) mammograms. (a) Sample subimage. (b) Image of texture energy values. (c) Texture energy histogram (normalized for the range of feature values).

$$\lim_{m,n \rightarrow \infty} P(D_{m,n} \leq z) = 1 - 2 \sum_{r=1}^{\infty} (-1)^{r-1} \times \exp\left[-2r^2 z^2 \left(\frac{1}{m} + \frac{1}{n}\right)\right], \quad (2)$$

where m and n are the numbers of samples in the two sets, $D_{m,n}$ is the maximum CDF difference for the given number of samples, and P is the probability that $D_{m,n}$ is less than a given value z . The level of significance, α , is defined as

$$P(D_{m,n} > d_\alpha) = \alpha, \quad (3)$$

where d_α is the critical value of $D_{m,n}$ corresponding to the significance α . Thus, the observed discrepancy between a CDF drawn from clinical mammograms and a CDF drawn from simulated mammograms can be quantified in terms of

the significance, α , which is the probability that a greater discrepancy than observed would occur due to chance alone. The relationship between α and d_α for various sample sizes is tabulated in several textbooks.^{24,25}

The CDFs of statistics for each subimage from the clinical and synthetic mammograms were compared. In the texture energy analysis and the fractal analysis, for each subimage the appropriate feature value was averaged over all of the pixels in the subimage, and this average was used as a sample for the KS test. In the morphological analysis, for each subimage the first moment of the brightness gradient was used as a sample value.

Both the KS test and the histogram correlation show how well, *on average*, the synthetic images can approximate the properties of the clinical mammographic texture. The differ-

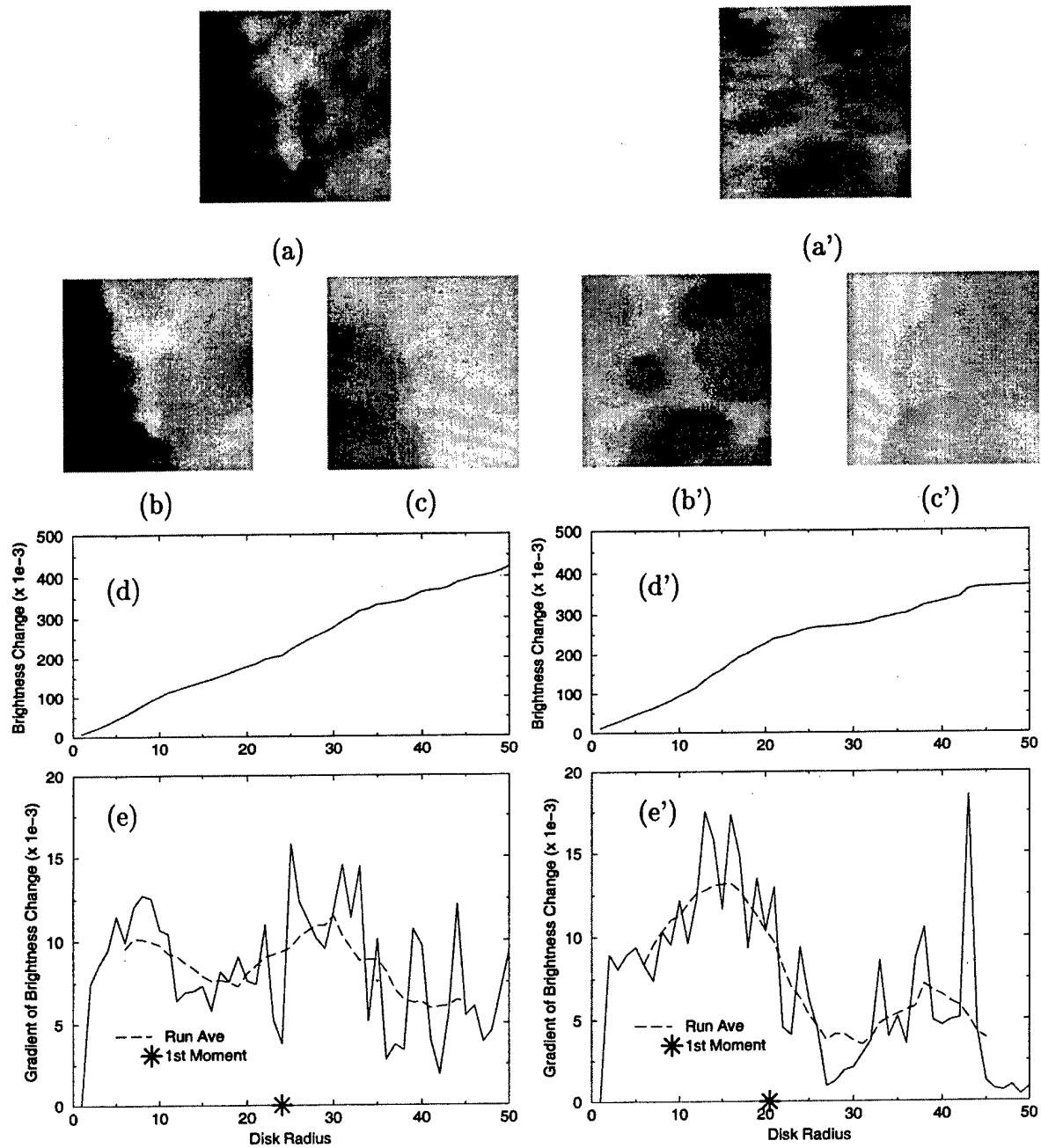


FIG. 4. Size analysis of the FGT from clinical (left) and synthetic (right, primed) mammograms. (a) Sample subimage. (b) Result of closing with a 10 pixel disk structuring element. (c) Result of closing with a 40 pixel disk. (d) Change in brightness (sum of all pixels) before and after closing. (e) Gradient of the brightness.

ence between the two methods is that the KS test compares the mean feature values averaged over each subimage, while the histogram correlation takes into account the range of feature values computed locally at each pixel.

3. Illustration of the analysis

An illustration of the histogram analysis is given in Fig. 3 by the texture energy features computed on subimages of retroareolar glandular tissue. The histogram of a clinical FGT subimage is shown on the left and of a synthetic subimage on the right. Histograms averaged over all clinical and over all

synthetic subimages are shown in Fig. 5(c). Figure 4 illustrates the analysis of object size distribution for the retroareolar glandular tissue. The left-hand side shows the results for the clinical FGT and the right-hand side for the synthetic FGT. The upper graphs show the average brightness (offset for the brightness of the original image) after each morphological closing as a function of structuring element (disk) size in pixels. Note that the output images get brighter with increasing disk size, as seen in the examples of the images obtained for the disk radii of 10 and 40 pixels. The graph in Fig. 4(e) shows the gradient of the features graphed in Fig.

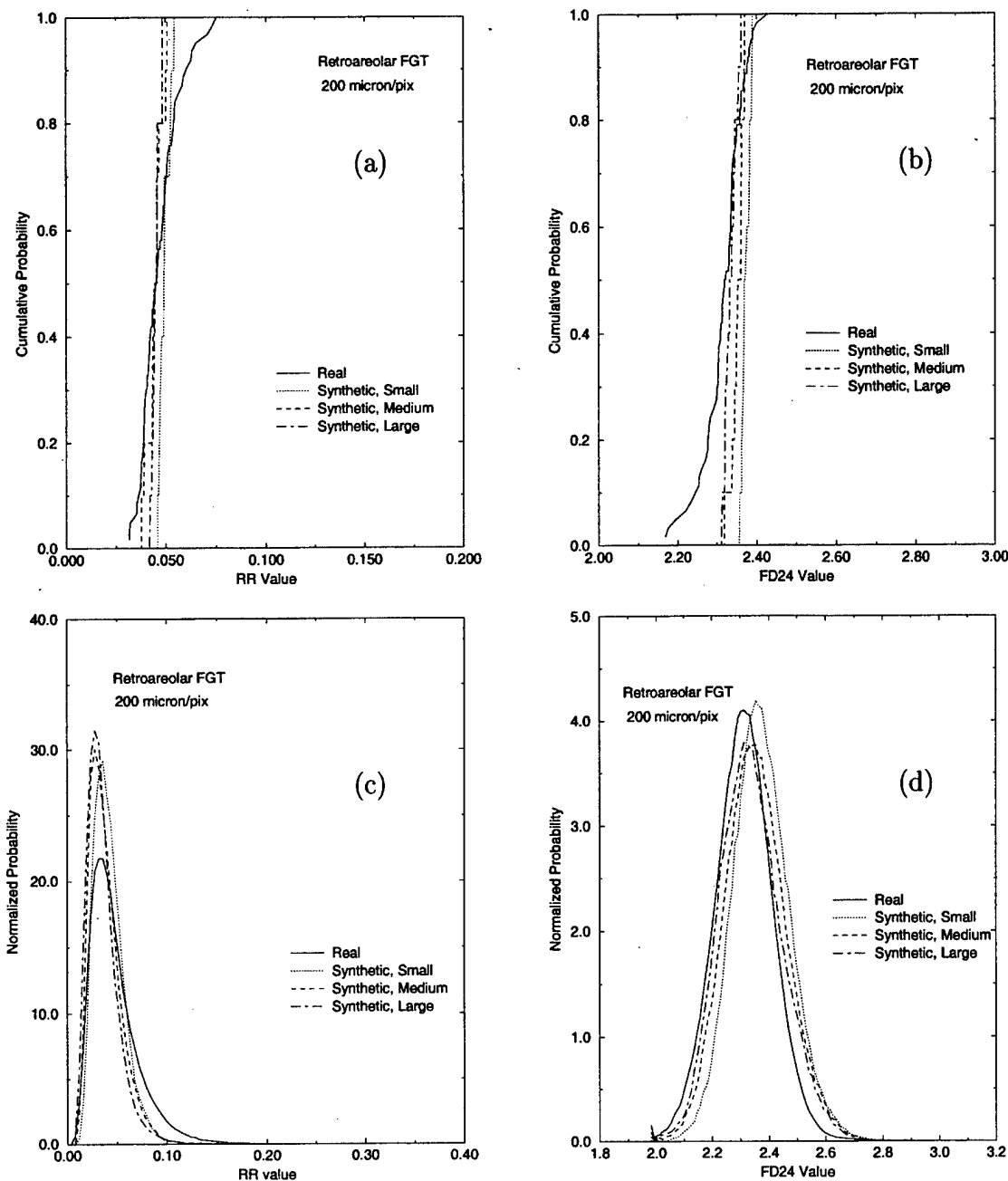


FIG. 5. Comparison between clinical and synthetic images of retroareolar fibroglandular tissue: CDFs of the (a) mean texture energy feature and (b) mean fractal analysis feature: average histograms of the (c) mean texture energy feature and (d) mean fractal analysis feature.

4(d). The gradient is used in place of the feature histogram for the size analysis. (Running averages of the gradients are shown for clarity.) Mean feature values, whose distributions were analyzed by the KS test, are also indicated on the graphs in Fig. 4(e). For texture energy and fractal dimension, the mean feature values were computed as the first moments of the feature histograms of each subimage. CDFs for all clinical and three groups of synthetic subimage means are shown in Fig. 6(b).

Figure 5 shows the CDF of the mean feature values and the average histograms for texture energy and fractal dimension computed for the samples of retroareolar glandular tissue regions in clinical and synthetic mammograms. Figure 6

gives the cumulative distributions of the first moments of the brightness gradients and the average brightness gradients for the size analysis of the clinical and synthetic samples of the subcutaneous adipose tissue (left) and the retroareolar glandular tissue (right).

III. RESULTS AND DISCUSSION

Results of the synthetic texture evaluation are presented in the form of graphs of the histogram correlation coefficients and maximum CDF differences computed for several texture features. Simulations were performed for three ranges of compartment size and for two spatial resolutions. Figures

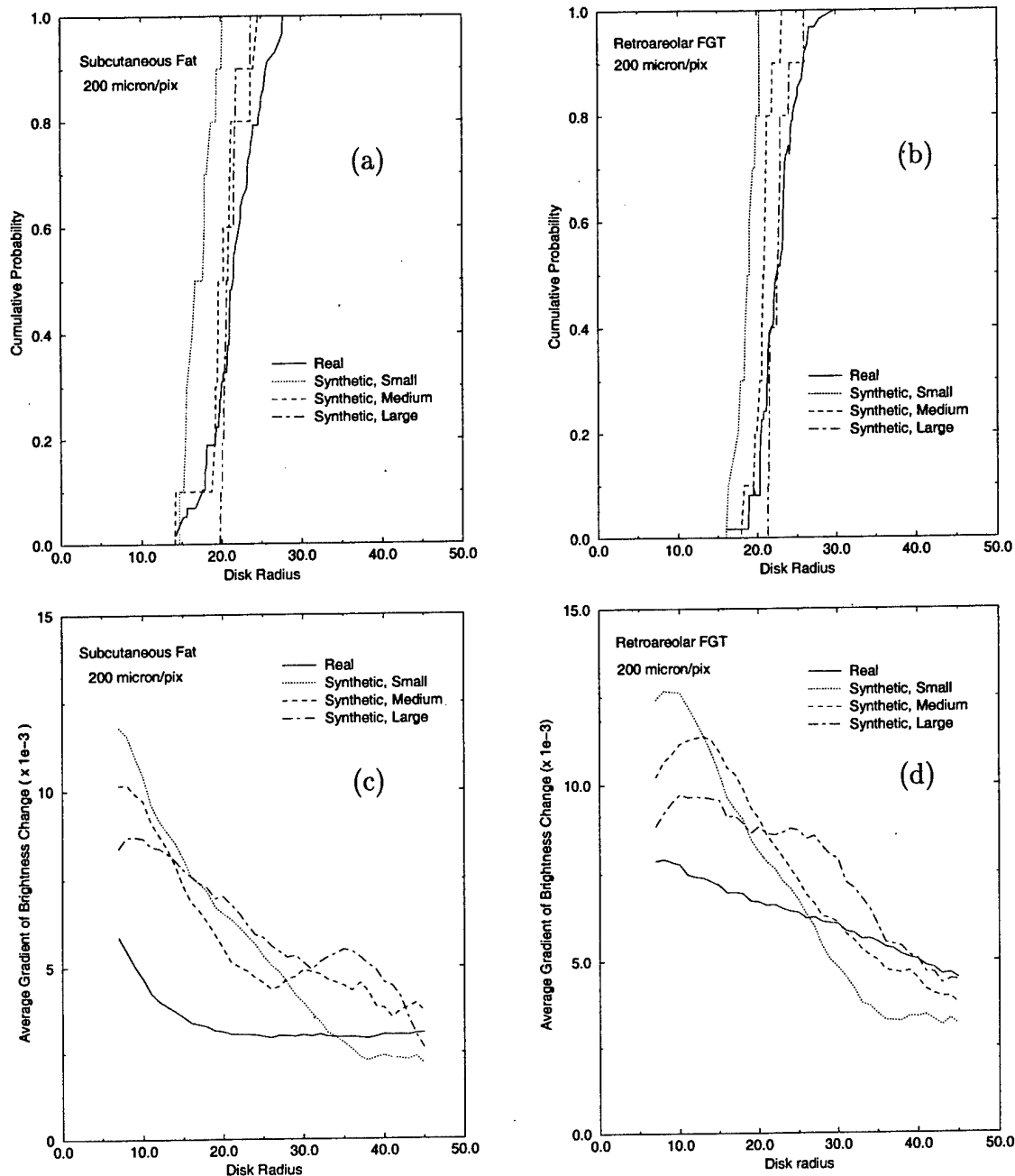


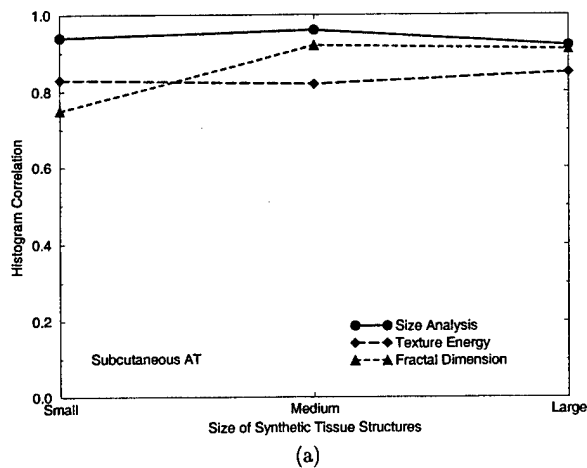
FIG. 6. Comparison between clinical and synthetic images using size analysis: CDFs of the mean features for (a) subcutaneous adipose tissue and (b) retroareolar fibroglandular tissue; average histograms for (c) subcutaneous adipose tissue and (d) retroareolar fibroglandular tissue.

7–10 show the results for subcutaneous adipose tissue, retromammary adipose tissue, retroareolar glandular and dense glandular tissue regions, respectively. The abscissa in these graphs is not a continuous variable, but indicates the size range of the simulated breast anatomic structures (adipose compartments). Texture features are labeled by different symbols: circle=average structure size, diamond=texture energy, and triangle=fractal dimension.

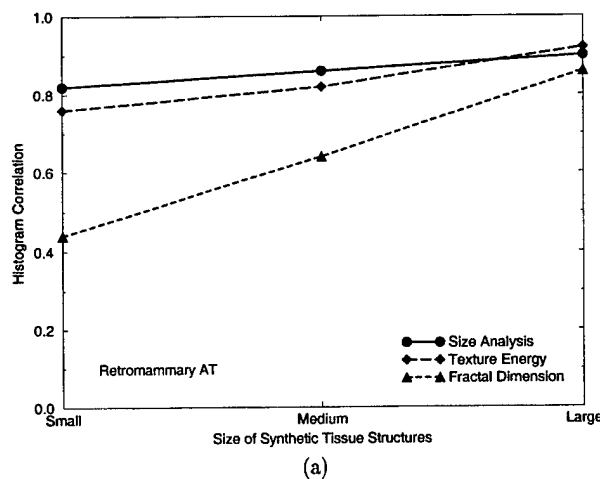
The graphs labeled (a) in Figs. 7–10 show the values of histogram correlation. Higher values indicate better correlation, with a maximum possible value of unity. A boot-strap analysis of the histogram correlation (averaged over all tissue

types, texture measures, and synthetic structure sizes) was used to calculate a standard deviation of approximately 0.003. In the CDF difference graphs [labeled (b)], the maximum difference between the CDFs is equal to one. Thus, the lower the value, the better the agreement between the clinical and synthetic textures. The CDF difference is translated into a significance level, as explained previously, on the vertical axis at the right of the graphs. Values of the CDF difference corresponding to significance levels of 1%, 5%, and 20% are shown.

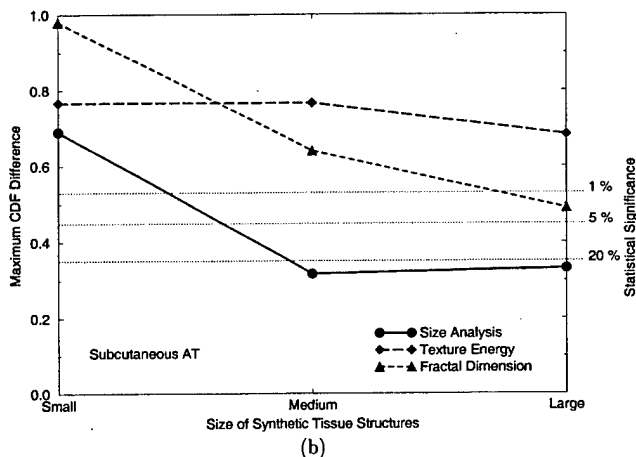
It can be seen that the size analysis (represented by circles) shows better agreement between the clinical and syn-



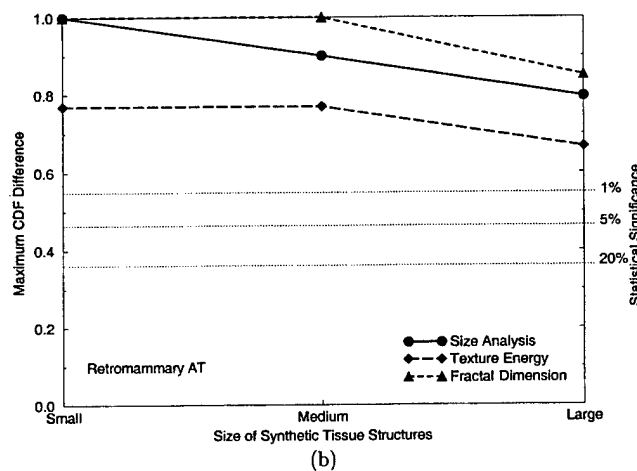
(a)



(a)



(b)



(b)

FIG. 7. Summary of (a) histogram correlation and (b) the results of the KS test, for subcutaneous adipose tissue. The data are presented for three ranges of size of synthetic tissue structures and for the three texture analysis methods.

FIG. 8. Summary of (a) histogram correlation and (b) the results of the KS test, for retromammary adipose tissue. The data are presented for three ranges of size of synthetic tissue structures and for the three texture analysis methods.

thetic texture, than the other two features. This is expected as the size of the radiolucencies is related to the size of the adipose compartments, while the other features are more sensitive to local, small scale structure. The current version of our model does not include fine, local tissue detail.

Results for the retroareolar glandular tissue regions are shown in Fig. 9. Most of the feature values are concentrated very close to one in the histogram correlation graph, indicating good agreement between the simulation and the real mammograms. Also, the CDF difference for the retroareolar glandular tissue are lower than for the other tissue regions. The dense glandular region shows similarly good agreement (Fig. 10). By comparison, both glandular tissue regions are simulated better than the adipose regions (Figs. 7 and 8).

A repeated comparison between synthetic and real mammograms at a resolution of $400 \mu\text{m}/\text{pixel}$ (not plotted) showed that the simulation results were not affected significantly by the change of resolution. In addition, from Figs. 7 to 10 one can see that the analyzed features are sensitive to the size of simulated anatomical structures and that the agreement between the synthetic and clinical mammograms depends upon our selection of the simulated structure size. A

partial analysis of a larger set of synthetic mammograms was also performed and no significant changes in the comparison with the set of real images were found.

The agreement between distributions of mean texture features suggests that the synthetic images sufficiently well simulate mean features of the clinical texture. Similarity between the averaged histograms of real and synthetic texture features means that our synthetic images can simulate the range of features seen over a large group of mammograms, not necessarily matching the feature distribution of any particular mammogram.

By varying the parameters which control the sizes of breast tissue model elements, we were able to match the average statistical properties of clinical mammograms for all tissue types except the retromammary fat. The best match for clinical mammogram texture was achieved for the simulated compartments with radii of 4–13.3 mm ("Medium" and "Large," as labeled in Table I in the accompanying paper¹) in predominantly adipose tissue region, and with radii of 2.7–5.33 mm ("Large") and 1.3–2.7 mm ("Small") in the retroareolar and dense FGT region, respectively. These pa-

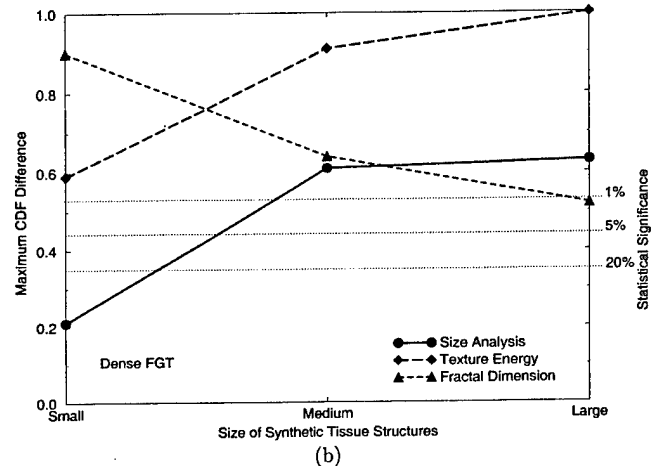
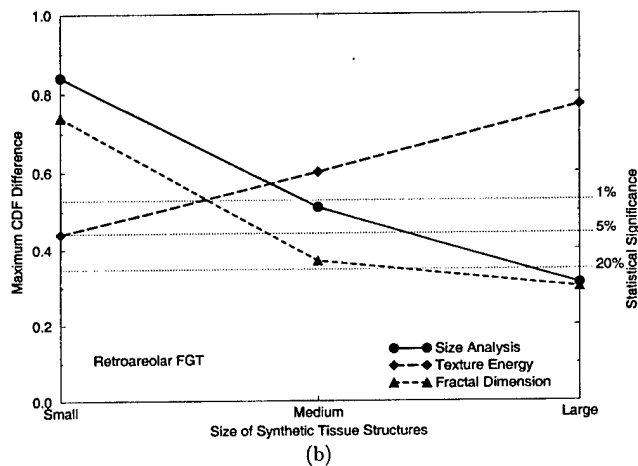
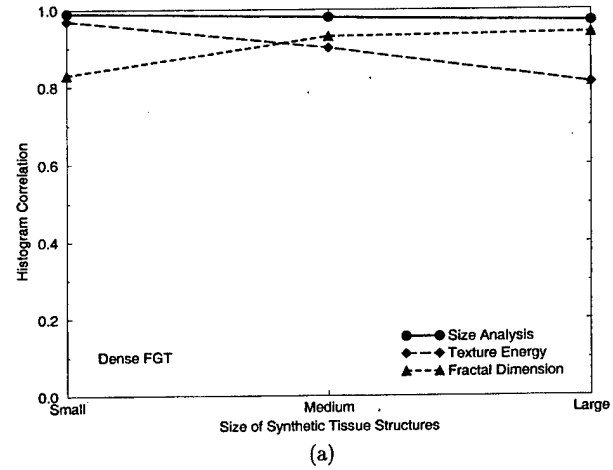
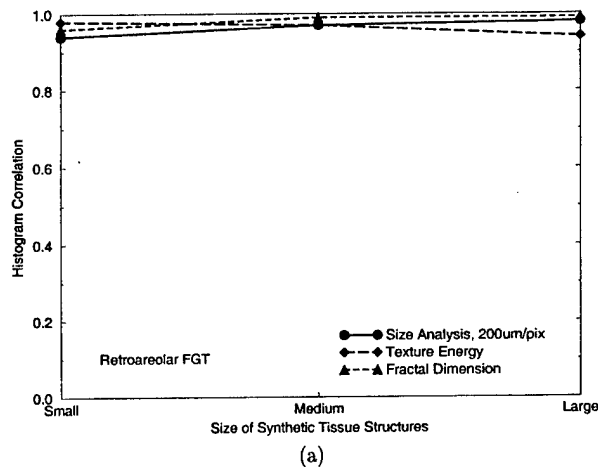


FIG. 9. Summary of (a) histogram correlation and (b) the results of the KS test, for retroareolar fibroglandular tissue. The data are presented for three ranges of size of synthetic tissue structures and for the three texture analysis methods.

FIG. 10. Summary of (a) histogram correlation and (b) the results of the KS test, for dense fibroglandular tissue. The data are presented for three ranges of size of synthetic tissue structures and for the three texture analysis methods.

rameters were chosen because of high histogram correlation values and low maximum CDF difference; the corresponding distribution of the size analysis features for real and synthetic images cannot be distinguished at the 5% level. A difference between the retroareolar and dense FGT region is expected, since the retroareolar region contains more fat clustered in larger compartments than in dense regions. Further understanding of the clinical retromammary adipose tissue structure is needed to improve the simulation.

IV. CONCLUSIONS

Evaluation of the synthetic mammograms was performed by texture analysis and comparison with normal clinical mammograms from the MIAS database. By varying the distribution of tissue structures in the model we have been able to match some of the statistical properties of clinical mammograms. Quantitatively, the synthetic mammograms have a similar distribution of the values averaged over a large number of mammograms for several texture features, namely the average size of image objects, the texture energy, and the fractal dimension. The analysis of mammogram object size is

closely related to the size analysis of the medium scale phantom elements, simulating adipose compartments in the breast, which are responsible for generation of the synthetic mammogram texture. This was the first such use of the morphological analysis of lucent mammogram regions, representing the projections of adipose compartments. Previous applications of morphology focused on the mammogram regions brighter than their surroundings, such as the fibrous structures and microcalcifications. The texture energy and the fractal dimension are more sensitive to the local variation of pixel intensities due to the small scale breast tissue structures.

Our model clearly captures the coarse tissue structures of the breast for all the tissue subregions except the retromammary fat. This exception is likely due to the fact that currently the retromammary adipose tissue is simulated in the same way as the subcutaneous tissue, although it is possible that the amount of fibroglandular tissue differs in these two regions. The model is less capable of capturing the small scale structures of the breast, e.g., blood and lymph vessels and fine tissue detail, which affect fine texture and give or-

ganized structure familiar to radiologists. The overly geometric appearance of the borders between the AT and FGT regions in the synthetic mammograms can be improved by small, random variations in the position of the borders in the compressed tissue model. Differences between the synthetic and clinical images are more evident for texture measures that emphasize smaller spatial scales, in agreement with the qualitative visual assessment. We expect that the introduction of detailed tissue structures in our breast model will enhance the local variations of synthetic mammograms and the variations in feature distribution needed to better match clinical images.

ACKNOWLEDGMENTS

This work was supported in part by NSF Grant No. IRI-9504363 and by US Army Breast Cancer Research Program Grant Nos. DAMD 17-96-1-6128 and DAMD 17-98-1-8169.

APPENDIX: BACKGROUND ON TEXTURE ANALYSIS

1. Mathematical morphology

Morphological operations are performed on an image, $f(x, y)$, using a second set of pixels, S , called the structuring element. The basic morphological operations, are defined by:¹³

$$\text{Dilation: } (f \oplus S)(x, y) = \max\{f(x+x', y+y') \mid (x', y') \in S\},$$

$$\text{Erosion: } (f \ominus S)(x, y) = \min\{f(x-x', y-y') \mid (x', y') \in S\},$$

$$\text{Opening: } f \circ S = (f \ominus S) \oplus S,$$

$$\text{Closing: } f \bullet S = (f \oplus S) \ominus S.$$

2. Texture energy analysis

2D convolution masks for texture energy analysis are derived using 1D masks with different number of zero-crossings, designed to detect different texture properties. For example, the five-element 1D masks are:⁹

$$\text{Level: } L5 = [1 \ 4 \ 6 \ 4 \ 1],$$

$$\text{Edge: } E5 = [-1 \ -2 \ 0 \ 2 \ 1],$$

$$\text{Spot: } S5 = [-1 \ 0 \ 2 \ 0 \ -1],$$

$$\text{Wave: } W5 = [-1 \ 2 \ 0 \ -2 \ 1],$$

$$\text{Ripple: } R5 = [1 \ -4 \ 6 \ -4 \ 1].$$

The most often used 2D masks in mammogram analysis are 5×5 "level" and "ripple" masks, obtained by the product of the corresponding 1D masks ($R5R5 = R5^T R5$ and $L5L5 = L5^T L5$):

$$R5R5 = \begin{bmatrix} 1 & -4 & 6 & -4 & 1 \\ -4 & 16 & -24 & 16 & -4 \\ 6 & -24 & 36 & -24 & 6 \\ -4 & 16 & -24 & 16 & -4 \\ 1 & -4 & 6 & -4 & 1 \end{bmatrix}, \quad (A2)$$

$$L5L5 = \begin{bmatrix} 1 & 4 & 6 & 4 & 1 \\ 4 & 16 & 24 & 16 & 4 \\ 6 & 24 & 36 & 24 & 6 \\ 4 & 16 & 24 & 16 & 4 \\ 1 & 4 & 6 & 4 & 1 \end{bmatrix}.$$

3. Fractal analysis

Image fractal dimension is usually defined using the area of the image surface. When the scale, ϵ , is increased (which corresponds to decreasing the resolution) the area of a fractal surface, $A(\epsilon)$, decreases. The fractal dimension, D , is related to the slope of decreasing area on a log-log plot, as

$$\log A(\epsilon) = \log \text{const} + (2 - D) \log \epsilon. \quad (A3)$$

There are several algorithms for computing fractal dimension based upon box counting, image power spectrum, or iterated function systems.²⁶ Any attempt at measuring fractal dimension must deal with the fact that self-similarity of real images holds only over a limited range of scales, due to actual structure and limitations of the imaging process.²⁷

^aAuthor to whom correspondence should be addressed; electronic mail: Andrew.Maidment@mail.tju.edu

¹P. R. Bakic, M. Albert, D. Brzakovic, and A. D. A. Maidment, "Mammogram synthesis using 3D simulation. I. Breast tissue model and image acquisition simulation," *Med. Phys.* **29**, 2131-2139 (2002).

²F. O. Bochud, C. K. Abbey, and M. P. Eckstein, "Statistical texture synthesis of mammographic images with clustered lumpy backgrounds," *Opt. Express* **4**, 33-43 (1999).

³J. J. Heine, S. R. Deans, R. P. Velthuis, and L. P. Clarke, "On the statistical nature of mammograms," *Med. Phys.* **26**, 2254-2265 (1999).

⁴P. Taylor, R. Owens, and D. Ingram, "Simulated mammography using synthetic 3D breasts," in *Digital Mammography Nijmegen, 1998*, Proceedings of the Fourth International Workshop on Digital Mammography, Nijmegen, The Netherlands, June 1998, edited by N. Karssemeijer, M. Thijssen, J. Hendriks, and L. van Erning (Kluwer Academic, Dordrecht, 1998), pp. 283-290.

⁵P. R. Bakic, "Breast tissue description and modeling in mammography," Ph.D. dissertation, Lehigh University, Bethlehem, PA, 2000.

⁶P. R. Bakic, M. Albert, and A. D. A. Maidment, "Evaluation of breast ductal networks using ramification matrices," in *IWDM 2002*, Proceedings of the Sixth International Workshop on Digital Mammography (Bremen, Germany, June 2002).

⁷J. Suckling et al., "The Mammographic Image Analysis Society Digital Mammogram Database," in *Digital Mammography*, Proceedings of the Second International Workshop on Digital Mammography, York, England, 10-12 July 1994, edited by A. G. Gale, S. M. Astley, D. R. Dance, and A. Y. Cairns (Elsevier Science, Amsterdam, 1994), pp. 375-378 (<http://www.wiau.man.ac.uk/services/MIAS/MIASmini.html>).

⁸J. Serra, *Image Analysis and Mathematical Morphology* (Academic, London, 1982).

⁹K. I. Laws, "Textured Image Segmentation," Ph.D. dissertation, University of Southern California, Los Angeles, CA, 1980.

¹⁰S. Peleg, J. Naor, R. Hartley, and D. Avnir, "Multiple resolution texture analysis and classification," *IEEE Trans. Pattern Anal. Mach. Intell.* **6**, 518-523 (1984).

- ¹¹G. Matheron, *Random Sets and Integral Geometry* (Wiley, New York, 1975).
- ¹²R. M. Haralick, S. R. Sternberg, and X. Zhuang, "Image analysis using mathematical morphology," *IEEE Trans. Pattern Anal. Mach. Intell.* **9**, 532–550 (1987).
- ¹³S. Behrens and J. Dengler, "Analyzing the structure of medical images with morphological size distributions," *Proceedings of the Tenth International Conference on Pattern Recognition*, Atlantic City, NJ, June 1990, pp. 886–890.
- ¹⁴P. I. Müller and S. M. Astley, "Classification of breast tissue by texture analysis," *Image Vis. Comput.* **10**, 277–282 (1992).
- ¹⁵M. Unser, "Local linear transforms for texture measurements," *Signal Process.* **11**, 61–79 (1986).
- ¹⁶W. P. Kegelmeyer, Jr. and M. C. Allmen, "Dense feature maps for detection of calcifications," in *Digital Mammography*, *Proceedings of the Second International Workshop on Digital Mammography*, York, England, 10–12 July 1994, edited by A. G. Gale, S. M. Astley, D. R. Dance, and A. Y. Cairns (Elsevier Science, Amsterdam, 1994), pp. 3–12.
- ¹⁷N. Vujovic and D. Brzakovic, "Establishing correspondence between control points in pairs of mammographic images," *IEEE Trans. Image Process.* **6**, 1388–1399 (1997).
- ¹⁸M. Sallam and K. Bowyer, "Registration time sequences of mammograms using a two-dimensional image unwarping technique," in *Digital Mammography*, *Proceedings of the Second International Workshop on Digital Mammography*, York, England, 10–12 July 1994, edited by A. G. Gale, S. M. Astley, D. R. Dance, and A. Y. Cairns (Elsevier Science, Amsterdam, 1994), pp. 121–130.
- ¹⁹C. B. Caldwell, S. J. Stapleton, D. W. Holdsworth, R. A. Jong, W. J. Weiser, G. Cooke, and M. J. Yaffe, "Characterization of mammographic parenchymal pattern by fractal dimension," *Phys. Med. Biol.* **35**, 235–247 (1990).
- ²⁰F. Lefebvre, H. Benali, R. Gilles, E. Kahn, and R. Di Paola, "A fractal approach to the segmentation of microcalcifications in digital mammograms," *Med. Phys.* **22**, 381–390 (1995).
- ²¹H. Li, K. J. R. Liu, and S.-C. B. Lo, "Fractal modeling and segmentation for the enhancement of microcalcifications in digital mammograms," *IEEE Trans. Med. Imaging* **16**, 785–798 (1997).
- ²²X. Liu, G. Zhang, and M. D. Fox, "Fractal description and classification of breast tumors," *Proceedings of the Annual International Conference of the IEEE Engineering in Medicine and Biology Society*, 1991, Vol. 13, pp. 112–113.
- ²³J. N. Wolfe, "Risk for breast cancer development determined by mammographic parenchymal patterns," *Cancer* **37**, 2486–2492 (1976).
- ²⁴A. G. Frodesen, O. Skjeggstad, and H. Tofte, *Probability and Statistics in Particle Physics* (Universitetsforlaget, Oslo, 1979).
- ²⁵G. K. Kanji, *100 Statistical Tests* (SAGE, London, 1999).
- ²⁶M. Barnsley, *Fractals Everywhere* (Academic, Boston, 1988).
- ²⁷A. I. Penn and M. H. Loew, "Estimating fractal dimensions with fractal interpolation function models," *IEEE Trans. Med. Imaging* **16**, 930–937 (1997).

Classification of Galactograms with Ramification Matrices: Preliminary Results¹

Predrag R. Bakic, PhD, Michael Albert, PhD, Andrew D. A. Maidment, PhD

Rationale and Objectives. The poor specificity of galactography, the imaging modality generally indicated in cases of nipple discharge, has led to a large number of biopsies with negative results. A quantitative scheme for classifying galactographic findings might help reduce the number of such biopsies in the future. As a first step toward that goal, the authors have studied one quantitative method for describing the branching of ducts by using ramification matrices (R matrices), and the correlation of the values of the matrix elements with clinical findings.

Materials and Methods. The ductal trees were manually segmented for 25 galactographic views from 15 patients, and corresponding R matrices were calculated. Patients were divided into two groups: those with no reported galactographic findings (NF) and those with reported findings (RF) of ductal ectasia, cysts, or papilloma. In a leave-one-out fashion, the authors evaluated a classification scheme that was based on R-matrix coefficients and used a Bayesian decision rule. The effects of segmentation were tested by successively removing each of the terminal ducts and computing the corresponding matrices of the pruned trees.

Results. With use of a single R-matrix element, 92% and 62% of NF and RF cases were correctly classified, respectively ($P = .007$). With use of two elements, 83% and 77% of NF and RF cases were correctly classified, but this result was not statistically significant ($P = .108$). In a test of robustness, an analysis of pruned trees yielded an average root-mean-square fractional difference of 9.7% between the elements of the original and the R matrix averaged over all pruned trees.

Conclusion. The preliminary analysis indicates that it may be possible to identify cases with reported galactographic findings by using R matrices.

Key Words. Breast, ducts; breast neoplasms, diagnosis; galactography.

© AUR, 2003

Virtually all breast cancers derive from epithelial tissue, with 90% of malignant lesions arising in the ductal epithelium (1, p 118). Most carcinomas spread initially along the lumen of the ducts or lobules. Evidence of this growth pattern is seen in the distribution of calcifications

associated with early breast cancer, which often follows the ductal pathway (2).

Major ducts of the breast extend from the nipple toward the chest wall in a branching network of smaller and smaller ducts, which defines a draining territory, or lobe (1,3-6). The adult breast contains 15-20 irregular lobes, which converge to the nipple. Each lobe is drained by its own major duct. Several major ducts merge to form an ampulla (or lactiferous sinus), a dilated segment beneath the nipple. Branching of the ducts toward the chest wall continues until a duct finally ends in blunt fingerlike ductules formed by the acini, the basic glandular secretory units. During lactation the ductal network drains milk

Acad Radiol 2003; 10:198-204

¹ From the Department of Radiology, Thomas Jefferson University, Suite 3390 Gibbon Bldg, 111 S 11th St, Philadelphia, PA 19107-5563. Received September 6, 2002; revision requested October 16; final revision received and accepted November 7. Supported by U.S. Department of Defense, grant DAMD-17-98-1-8169. Address correspondence to A.D.A.M.

© AUR, 2003

produced in the acini. Ductules surrounded by specialized connective tissue are called *lobules*. A lobule with its terminal duct is known as the *terminal ductal lobular unit*.

Some cancers are revealed by nipple discharge alone, with no palpable or mammographic lesions. Indicated in cases of nipple discharge, galactography is a procedure for imaging the contrast material-enhanced ductal network (7-9). It is performed by carefully identifying the discharging nipple orifice, introducing a blunt needle, and injecting a small amount of radiographic contrast material. Pre- and postcontrast mammograms are obtained with the needle in place, thereby revealing the breast lobe that contains the discharging duct. Various ductal patterns (eg, filling defects, ductal ectasia) can be recognized from galactograms (10). Galactography lacks specificity (1), a situation that results in a large number of biopsies with normal or benign results. A quantitative radiographic classification scheme for galactograms might help reduce the percentage of biopsies with negative results and the related psychological and economic effects.

The ductal origin of breast cancer is the physiological basis for various techniques of diagnosis and treatment. The analysis of nipple aspirate fluid (11) has been investigated for early cancer detection. Breast cancer risk has been estimated by analyzing the parenchymal pattern of projected fibrous and ductal structures (12). In surgical assessment of nipple discharge, preoperative staining of the ducts can minimize the amount of tissue excised (9). The breast ductal network has been modeled by tracing the points of duct entrance to and exit from a series of subgross histologic slices (13,14). The use of statistical analyses of ductal networks for breast modeling also has been reported (15,16).

Describing the normal ductal network is difficult because of anatomic variability and low radiographic contrast. Here, we report a method of analyzing ductal networks by using ramification matrices (R matrices), which describe the topologic shape of a treelike structure (17). The R-matrix elements represent branching probabilities at various levels of a tree and can be used to describe a given tree or to generate a family of trees. The probabilistic nature of R matrices makes them useful for generating many individual synthetic trees with matching statistical properties of branching. For this reason, R matrices have been used to generate ductal networks in breast modeling for mammographic simulation (16).

The morphology of the ductal network reflects the state of breast development and the healthy or pathologic state of the breast tissue, as has been shown by analyses

of the branching of murine mammary ducts in different phases of gland development (18,19) and by studies of epithelial cellular organization under the influence of hormones, growth factors, and carcinogens (20-22). We hypothesize that diseases of the breast, demonstrated through alterations of the normal ductal anatomy, can be quantified and classified from galactograms. In the present study, we manually segmented ductal trees from 25 galactograms, calculated the R matrices, and computed the probability of correct classification for a combination of R-matrix elements. We also tested the robustness of the R-matrix representation by analyzing pruned trees.

MATERIALS AND METHODS

Clinical galactograms for this analysis were obtained retrospectively from 15 patients with a mean age of 49.2 years (range, 29-75 years). These patients were selected from a group of 41 who had undergone galactography at the Thomas Jefferson University Breast Imaging Center, Philadelphia, Pa, during the 6½-year period from June 1994 through January 2001. Galactograms from 17 of the 41 patients were unavailable because they had been returned to the patients or the primary health care institutions, and galactograms from another nine patients were not used, because of obstruction or poor image quality (ie, the complete ductal tree could not be segmented). Of the 15 patients whose cases were analyzed, eight (mean age, 44.2 years; range, 29-74 years) had no reported galactographic findings (hereafter NF), and seven (mean age, 54.8 years; range, 43-75 years) had galactographic findings of ductal ectasia, cysts, or papilloma (hereafter RF). Twenty-five galactographic views of the 15 patients were analyzed (16 craniocaudal [CC] and nine mediolateral or mediolateral oblique [hereafter denoted in combination as ML/MLO]), of which 12 views (eight CC and four ML/MLO) were from NF cases and 13 (eight CC and five ML/MLO) were from RF cases. There were no reported findings of malignancy from these 25 galactograms. Furthermore, mammographic follow-up data were available for eight of the 15 patients for an average period of 4.75 years (range, 3.5-6.0 years), and no malignancies were reported. Patients' ages, available galactographic views, symptoms, and reported galactographic findings are listed in the Table.

To reconstruct the ductal topology, each branch in the ductal network was drawn by hand on a sheet of tracing paper placed over the galactogram displayed on a light box (Figure 1). The points where ducts branched were

Patient's Age, Available Views, Symptoms, and Galactographic Findings

Age (y)	View	Symptom	Galactographic Finding
29	LCC	Greenish discharge	None
30	LML, LCC	Clear/yellow discharge	None
32	LML(Mag), LCC	Bloody discharge	None
36	LCC	Bloody/yellow discharge	None
43	RML, RCC	Greenish discharge	Cysts
44	RCC	Bloody discharge	Cysts, ductal ectasia
45	RCC, LML	Bloody/milky discharge	None
45	LCC	Dilated ducts on mammogram and US image	None
47	RMLO, RCC	Greenish discharge, mastitis	Cysts, ductal ectasia
	RML, RCC		
50	RML, RCC	Greenish discharge	Cysts
55	RCC, RMLO	Clear discharge	Cysts
63	LMLO, LCC	Darkish discharge	None
70	RCC	Bloody discharge	Ductal ectasia
74	LCC	Clear/bloody discharge	None
75	RCC	Bloody discharge	Papilloma

Note.—LCC = left craniocaudal, LML = left mediolateral, RML = right mediolateral, RCC = right craniocaudal, RMLO = right mediolateral oblique, LMLO = left mediolateral oblique, and Mag = magnified.

distinguished from the points of overlap by the fact that the latter are galactographically brighter, due to superposition of the x-ray attenuation. Large ducts were reconstructed by connecting the marked points. In each of the segmented ductal trees, the root, internal and terminal nodes, and branches were labeled and the R-matrix elements were computed as described by Viennot et al (17). Simplified, the algorithm is given as follows: (a) all terminal branches have label 1, (b) a "parent" branch whose "children" have labels i and j will be labeled by $\max(i, j)$ if $i \neq j$ or by $(i + 1)$ if $i = j$, and (c) the labeling procedure continues until the root branch is reached whose label s is called the *Strahler number* of the tree structure.

The R matrix of a tree with Strahler number s is a lower triangular matrix, defined as

$$R_{(s-1),s} = [r_{k,j} = b_{k,j}/a_k, k \in (2, s), j \in (1, k)], \quad (1)$$

where a_k is equal to the number of branches with label k (17). For $j < k$, $b_{k,j}$ is the number of pairs of branches with labels k and j , while for $j = k$, $b_{k,j}$ is the number of pairs of branches both labeled $k - 1$, descending from a node. Therefore, $r_{k,j} = b_{k,j}/a_k = p(b_{k,j}|a_k)$ is the probability that a branch with label k will bifurcate into branches with the appropriate labels. Figure 1c shows the numerically labeled branches of the segmented ductal tree from Figure 1a. In Figure 1c, there are 14 branches with label 2, six of which bifurcate into pairs of branches with la-

nels 1 and 2, corresponding to the probability of $r_{2,1} = 6/14 = 0.43$. The other eight branches with label 2 bifurcate into pairs of branches both with label 1, corresponding to the probability of $r_{2,2} = 8/14 = 0.57$. In a similar manner, all the elements of the R matrix shown in Figure 1d were computed from the galactogram shown in Figure 1a. We computed R matrices with nine elements and Strahler number $s = 4$, corresponding to a root branch with label 4.

A linear Bayesian decision rule was used to classify the galactographic findings. In the design of the Bayesian classifier, we assumed that the data were normally distributed and that the population standard deviation was the same for both classes. These assumptions reduce the risk of overspecification due to the small sample size. We estimated the standard error of the classification results by means of a leave-one-out (jackknife) method, in which the percentages correctly classified are calculated for subsets of the data formed by leaving each sample out in turn. The standard error of the classification results is then the standard deviation of the values calculated for the jackknife subsamples (23).

A preliminary test of the robustness of the R-matrix approach was performed by analyzing pruned ductal trees derived from an original tree after removal of a single terminal branch. This test was proposed because of the observed ambiguity in tracing terminal branches, which can be easily overlooked due to their small size and low



Figure 1. Segmentation of a ductal tree, showing (a) part of a galactogram with a contrast-enhanced ductal network, (b) the manually traced network of larger ducts from the contrast-enhanced portion of the galactogram, (c) numeric labeling of branches in the ductal network, and (d) the R matrix computed from the branching pattern. The dots, triangles, and squares denote branching points of different levels of the tree.

$$R = \begin{bmatrix} r_{2,1} & r_{2,2} & \cdot & \cdot \\ r_{3,1} & r_{3,2} & r_{3,3} & \cdot \\ r_{4,1} & r_{4,2} & r_{4,3} & r_{4,4} \end{bmatrix} = \begin{bmatrix} 0.43 & 0.57 & \cdot & \cdot \\ 0 & 0.33 & 0.67 & \cdot \\ 0 & 0.75 & 0 & 0.25 \end{bmatrix}$$

d.

contrast. Consequently, some of the terminal branches might have been omitted, resulting in a pruned version of the original tree. The R matrix of a pruned tree was computed and the procedure was repeated for each of the terminal branches in the original tree. A comparison was performed by computing the root-mean-square fractional difference, as follows:

$$D = \sqrt{\sum_{k=2}^s \sum_{j=1}^k \left[\frac{r_{k,j} - r_{k,j}^{prun}}{r_{k,j}} \right]^2 / N_{el}} \quad (2)$$

where $r_{k,j}$ and $r_{k,j}^{prun}$ are the elements of the original R matrix and the matrix averaged over all pruned versions of the original tree, respectively. N_{el} is the number of non-zero R-matrix elements ($N_{el} \leq 9$ for $s = 4$, from Eq [1]).

RESULTS

The values of the R-matrix elements calculated from clinical galactograms and the averages over all NF and all

RF cases are plotted in Figure 2. Some matrix elements show a noticeable difference in mean value between the two classes (eg, $r_{3,2}$ and $r_{3,3}$), suggesting the possibility of classifying galactographic findings on the basis of R matrices. We evaluated a classification scheme that used either a single matrix element or a pair of them and a linear Bayesian decision rule in a leave-one-out fashion. The classification performance of a single R-matrix element was best (in terms of the sum of the correctly identified fractions in the two groups) for $r_{3,3}$, which correctly classified $92\% \pm 2$ of NF and $62\% \pm 3$ of RF cases. In a combination of two elements, $r_{3,2}$ and $r_{3,3}$ correctly classified $83\% \pm 4$ of NF cases and $77\% \pm 4$ of RF cases. Figure 3 illustrates the classification results.

To estimate the statistical significance of the classification results, we performed an additional experiment by using random numbers as descriptive parameters. Six numbers, corresponding to the linearly independent elements of the R matrix with nine elements, were randomly generated for each of the 25 galactograms. This procedure was repeated for 10,000 trials, and in each trial the ran-

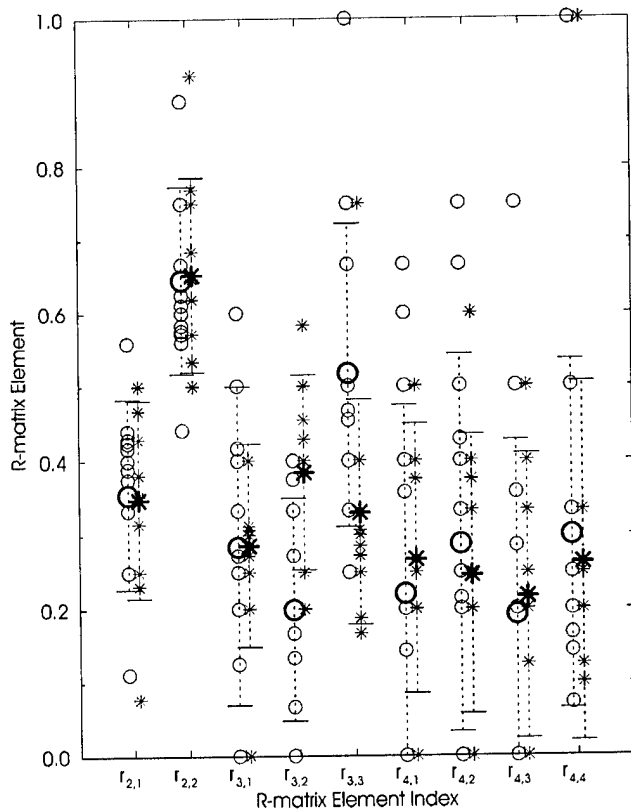


Figure 2. Values of the R-matrix elements. Bold symbols (○ = RF, * = NF) represent element values averaged over all RF and all NF cases, and light symbols represent the individual cases. Error bars correspond to the sample standard deviations.

domly generated data were used to classify galactograms by means of either one or two matrix elements, as was done for the real data. In 0.7% of trials, one of the parameters showed a classification power of at least 92% for one class and at least 62% for the other—comparable with the performance of element $r_{3,3}$ on the clinical galactograms. Thus, if the classification result observed for the clinical galactograms is by chance alone, it would be encountered in just 0.7% of repeated experiments, and the statistical significance for classification with $r_{3,3}$ is $P = .007$. The classification results achieved with the pair of elements $r_{3,2}$ and $r_{3,3}$ was not statistically significant ($P = .108$).

The analysis of the pruned versions of the clinical galactograms showed an average root-mean-square fractional difference between the original R-matrix elements and the elements averaged over all pruned trees of 9.7% for all NF and RF galactograms (6.5% for the NF cases and 12.6% for the RF cases). A similar analysis, which considered 1,000 synthetically generated random binary

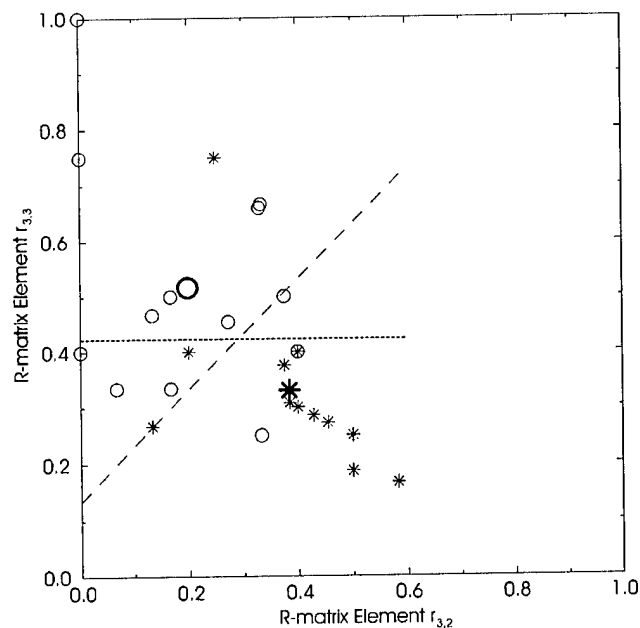


Figure 3. Classification of galactographic findings based on elements of the R matrix and a Bayesian linear decision rule. Bold symbols (○ = RF, * = NF) represent element values averaged over all RF and NF cases, and light symbols represent the individual cases. Short dashes indicate Bayesian decision line for $r_{3,3}$, and long dashes indicate Bayesian decision line for $r_{3,2}, r_{3,3}$.

trees pruned in the same fashion, yielded an average root-mean-square fractional difference of 6.8% (24).

DISCUSSION

We investigated the branching structure of ducts visualized on galactograms and evaluated the use of R matrices to classify galactographic findings. As an illustration of the classification results, Figure 4 shows two galactograms from the sets of NF and RF cases used in the study. The NF galactogram in Figure 4a corresponds to the values $r_{3,2} = 0.5$ and $r_{3,3} = 0.19$. The RF galactogram in Figure 4b corresponds to the values $r_{3,2} = 0.33$ and $r_{3,3} = 0.67$.

Results obtained in this study show that element $r_{3,2}$ is approximately 50% smaller and element $r_{3,3}$ is approximately 50% larger when averaged over all RF images, relative to the average over NF images: $\langle r_{3,2}^{RF} \rangle = 0.20$ whereas $\langle r_{3,2}^{NF} \rangle = 0.38$, and $\langle r_{3,3}^{RF} \rangle = 0.52$ whereas $\langle r_{3,3}^{NF} \rangle = 0.33$. These differences in the matrix elements may be due to long-term processes that alter the ductal branching pattern. Another explanation may be cutoff or dilation of the ducts, which affects the filling of the ductal network with contrast agent and the visibility of the

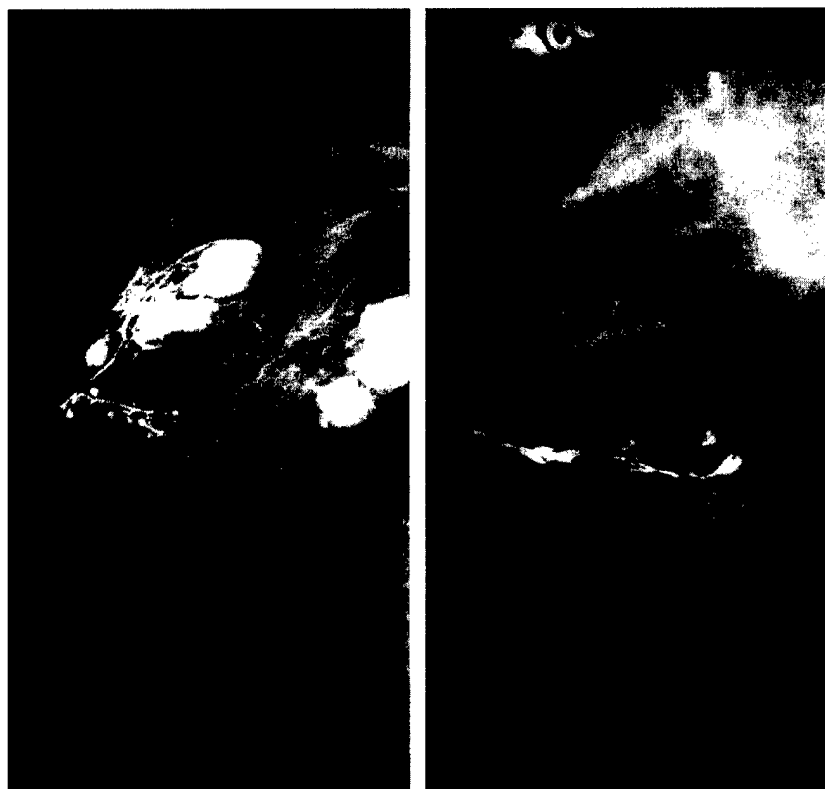


Figure 4. Two examples of galactograms that have been correctly classified by means of R matrices. **(a)** Galactogram with no reported findings (patient age, 45 years; right CC view; $r_{3,2} = 0.5$ and $r_{3,3} = 0.19$). (Large bright regions seen in this galactogram are due to extravasation, which did not affect the segmentation of the ductal tree.) **(b)** Galactogram with a reported finding of cysts (patient age, 55 years; right CC view; $r_{3,2} = 0.33$ and $r_{3,3} = 0.67$).

smaller ducts, thereby altering the calculated R matrix. Further research is needed to investigate the relationship between galactographic changes and R-matrix element values.

The root-mean-square fractional difference, estimated from analysis of the pruned ductal trees, is on average 9.7%, significantly smaller than the difference between the average values of matrix elements $r_{3,2}$ and $r_{3,3}$. Moreover, the sample standard deviation of these elements is significantly larger than the root-mean-square difference measured from pruning. The means and standard deviations of these elements are shown in Figure 2. These findings substantiate the robustness of the R-matrix representation of ductal networks, as the observed variation in the galactograms cannot be explained by the accuracy of the segmentation.

Evaluation with the simulated data showed that classification based on a single element, $r_{3,3}$, performs at a statistically significant level ($P = .007$). The performance of classification based on a pair of elements, $r_{3,2}$ and $r_{3,3}$, was not significant ($P = .108$). This reduction in significance is understandable given that the use of two matrix elements increases the probability that some

pair will give a spuriously efficacious classification and given that the classifier design assigned equal importance to each matrix element to avoid overspecification.

Several confounding factors should be considered in the interpretation of these results. Patient age distributions differ for the NF and RF cases (mean age, 44.2 years for NF vs 54.8 years for RF). We tested and found essentially no correlation between the age and the matrix element values, with Pearson correlation coefficient values of 0.18 and 0.01 for the elements $r_{3,2}$ and $r_{3,3}$, respectively. Another possible influence could be our combination of galactograms obtained with all views, CC and ML/MLO. In an ideal case, with all the branches visible and with perfect segmentation, the reconstructed ductal trees would be the same on both CC and ML/MLO views, as would the corresponding R matrices, which was not the case in this experiment. We compared the maximum difference between the mean element values computed over normal and benign galactograms with the maximum difference between the mean element values computed over CC and ML/MLO views and found the former difference approximately two times greater than

the latter. The most limiting factor in our study, however, was the small sample.

In summary, our preliminary analysis indicates that R matrices may be used to identify cases with reported galactographic findings. The performance of classification with a single matrix element was statistically significant in a set of eight NF cases (12 views) and seven RF cases (13 views) with findings of ductal ectasia, cysts, or papilloma. Further experiments should use more galactograms and a more sophisticated decision rule and should include malignant cases.

REFERENCES

- Kopans DB. Breast imaging. 2nd ed. Philadelphia, Pa: Lippincott-Raven, 1998.
- Lanyi M. Diagnosis and differential diagnosis of breast calcifications. Berlin, Germany: Springer-Verlag, 1988.
- Cooper AP. On the anatomy of the breast. London, England: Longman, 1840.
- Dabelow A. Die milchdruese. In: Bargmann W, ed. Handbuch der mikroskopischen anatomie des menschen: haut und sinnesorgane. Berlin, Germany: Springer-Verlag, 1957; 277-485.
- Egan RL. Breast imaging: diagnosis and morphology of breast diseases. Philadelphia, Pa: Saunders, 1988.
- Bland KI, Copeland EM III, eds. The breast: comprehensive management of benign and malignant diseases. 2nd ed. Philadelphia, Pa: Saunders, 1998.
- Gregl A. Color atlas of galactography: clinical and radiological symptomatology and therapy of the secreting breast. Stuttgart, Germany: Schautter, 1980.
- Tabar L, Dean PB, Pentek Z. Galactography: the diagnostic procedure of choice for nipple discharge. Radiology 1983; 149:31-38.
- Cardenosa G, Doudna C, Eklund GW. Ductography of the breast: technique and findings. AJR Am J Roentgenol 1994; 162:1081-1087.
- Dinkel HP, Trusen A, Gassel AM, et al. Predictive value of galactographic patterns in benign and malignant neoplasms of the breast in patients with nipple discharge. Br J Radiol 2000; 73:706-714.
- Sauter ER, Ehya H, Babb J, et al. Biologic markers of risk in nipple aspirate fluid are associated with residual cancer and tumor size. Br J Cancer 1999; 81:1222-1227.
- Wolfe JN. Risk for breast cancer development determined by mammographic parenchymal patterns. Cancer 1976; 37:2486-2492.
- Moffat DF, Going JJ. Three dimensional anatomy of complete duct systems in human breast: pathological and developmental implications. J Clin Pathol 1996; 49:48-52.
- Ohtake T, Abe R, Kimijima I, et al. Intraductal extension of primary invasive breast carcinoma treated by breast-conservative surgery: computer graphic three-dimensional reconstruction of the mammary ductolubular systems. Cancer 1996; 76:32-45.
- Taylor P, Owens R, Ingram D. Simulated mammography using synthetic 3D breasts. In: Karssemeijer N, Thijssen M, Hendriks J, van Erning L, eds. Digital mammography: Nijmegen, 1998. Dordrecht, the Netherlands: Kluwer Academic, 1998; 283-290.
- Bakic PR. Breast tissue description and modeling in mammography. Dissertation. Lehigh University, Bethlehem, Pa, 2000.
- Viennot XG, Eyrolles G, Janey N, Arques D. Combinatorial analysis of ramified patterns and computer imagery of trees. Comput Graph 1989; 23:31-40.
- Humphreys RC, Lydon J, O'Malley BW, Rosen JM. Mammary gland development is mediated by both stromal and epithelial progesterone receptors. Mol Endocrinol 1997; 11:801-807.
- Atwood CS, Hovey RC, Glover JP, et al. Progesterone induces side-branching of the ductal epithelium in the mammary glands of periparturient mice. J Endocrinol 2000; 167:39-52.
- Russo IH, Russo J. Role of hormones in mammary cancer initiation and progression. J Mammary Gland Biol Neoplasia 1998; 3:49-61.
- Hansen RK, Bissell MJ. Tissue architecture and breast cancer: the role of extracellular matrix and steroid hormones. Endocr Relat Cancer 2000; 7:95-113.
- Brisken C. Hormonal control of alveolar development and its implications for breast carcinogenesis. J Mammary Gland Biol Neoplasia 2002; 7:39-48.
- Efron B. The jackknife, the bootstrap and other resampling plans. Philadelphia, Pa: Society for Industrial and Applied Mathematics, 1982.
- Bakic PR, Albert M, Maidment ADA. Evaluation of breast ductal networks using ramification matrices. In: Peitgen, HO, ed. Digital mammography. Heidelberg, Germany: Springer-Verlag (in press).

Effects of quantum noise on dose and contrast sensitivity in
stereoradiography

Andrew D. A. Maidment*, Predrag R. Bakic, and Michael Albert

Department of Radiology, Thomas Jefferson University

Suite 3390 Gibbon Building, 111 South 11th Street

Philadelphia, PA 19107-5563

A Manuscript for Submission to Medical Physics

Research Article

Submitted: September 18, 2002

*corresponding author; e-mail: Andrew.Maidment@mail.tju.edu

I. INTRODUCTION

A significant limitation of projection radiography is that relevant findings are often obscured or mimicked by the x-ray shadows of other anatomical structures (summation artifacts). By comparison, stereoradiography allows superimposed structures to be spatially separated, reducing the confounding effects of overlap. Stereoradiography was first proposed by Thomson in 1896¹ and continued to be used for certain radiographic procedures until the 1980's. The first recorded use of stereomammography occurred in 1930.² The advantages and disadvantages of stereoradiographic techniques are discussed in several radiographic text books and articles, e.g. Curry *et al.*³ Improvements in image quality of conventional film-screen radiographic systems combined with the added effort, cost and patient dose led to a decline in the use of stereoradiography and stereomammography.³ Development of digital x-ray detectors and softcopy reading has resulted in a renewal of interest in stereoradiography as a potentially useful method of reducing summation artifacts.

Dose in radiography is constrained by the imaging task, the x-ray quantum mottle, and the detector specifications. Quantum mottle is caused by the fluctuation in the number of x-ray quanta produced and transmitted through the tissue. For the same detector, the fewer the x-ray quanta, the greater the relative fluctuation, and the lower the signal-to-noise ratio of the object to be detected. An example of detector limitations is the characteristic ("H and D") curve, which determines a minimal useful exposure. The issues of dose in stereoradiography are either not mentioned in textbooks⁴⁻⁶ or it is suggested that a stereographic technique requires a total of twice the exposure of a single-projection technique.⁷ Signal detection theory suggests that, under quantum limited conditions, an ideal observer would be able to combine information from the two stereoscopic views and thereby suppress quantum mottle. Thus, under this model, two stereoscopic views, each acquired with one half of the dose of a single-projection radiograph, would provide the same level of resilience to quantum noise as a single projection acquired with the same total dose, but provide the inherent benefits of stereoscopic viewing.

Human observers perform certain visual tasks more efficaciously when fusing information from both eyes.^{8,9} In this paper we are concerned with the tasks of contrast perception and noise suppression, which are complementary to the well described advantages of stereoscopy in depth perception. For example, threshold measurements of sinusoidal patterns have shown a decrease in threshold (i.e., an increase in sensitivity) of a factor of $\sqrt{2}$ when viewing is performed binocularly as opposed to monocularly.¹⁰ This increase in sensitivity is precisely as expected for an ideal observer combining the signal from each eye. The quantum mottle in x-ray projections is different from the sources of noise in these experiments; in a radiograph, a given realization of the noise is permanently recorded at the time of acquisition and it is presented to each eye as a fixed pattern. For example, we note that flat random-noise fields presented stereoscopically cause lustre¹¹ (i.e., the image to appear to shimmer) due to an attempt by the visual system to stereoscopically fuse the random bright and dark variations.

The question of threshold detection of objects stereoradiographically is different from detection in other stereoscopic settings. To address this difference and examine the role of dose in stereoscopy we performed an observer study. Observer studies of stereoradiography have been reported in the literature previously. Kundel *et al.*⁹ compared stereoscopic acuity and effects of monocular depth cues under direct vision and in stereofluoroscopy, while Goodsitt, Chan, and Hadjiiski¹² studied depth perception in stereomammography. Berkson *et al.*⁶ compared the number of false negatives/positives in mono- and stereoscopic chest radiographs and Hsu *et al.*¹³ studied detection of simulated abnormalities in stereomammography.

Our observer study was based upon the hypothesis that in the merging of left and right eye images by the human visual system, the dose needed for each of the two stereoradiographic images is equal to one half of the dose for a single x-ray image viewed monoscopically. Thus, by corollary, we hypothesize that viewing a stereoscopic image will result in an effective increase in SNR by a factor of $\sqrt{2}$. A series of contrast-detail (C-d) experiments were performed with stereoradiographic images acquired over a range of exposures. The C-d experiment belongs to a class of threshold-visibility psychophysical measurements.¹⁴ In

the study, observers attempted to detect details in a C-d phantom. The observers scored the phantom monoscopically (both eyes seeing the same radiographic projection) and stereoscopically (each eye seeing a separately acquired projection). The focus of the study was on the issue of whether the human observer could combine the stereoscopic images in a manner so as to reduce the apparent quantum mottle. The two projections in each stereoradiographic pair were, therefore, acquired separately, although with the same geometry. No depth information was encoded, i.e., all objects were positioned in the imaging plane, to avoid the confounding issues of the variable ability of observers to fuse stereo pairs. The observers' performances were evaluated in terms of the difference in number of details seen stereo- vs. monoscopically, effective stereoscopic dose (equal to the dose needed for a monoscopic viewing with the same performance as for the stereoscopy), and the effective decrease in the threshold SNR values.

II. MATERIALS AND METHODS

A. Image acquisition

Radiographic images of an RMI-180 mammographic C-d phantom (Gammex RMI, Middleton, WI) were used in the observer study. The phantom has 90 objects aligned in nine columns. Adjacent objects within the same column differ in diameter by a factor of $\sqrt{2}$, with a range of 7.07-0.312 mm. The thickness of the objects in adjacent columns also differ by a factor of $\sqrt{2}$, with a range of 1.0-0.062 mm. The phantom projections were acquired with a DirectRay flat panel digital x-ray detector (Hologic/Direct Radiography, Newark, DE),¹⁵ without a grid. Observers were presented with a subregion of 650×810 pixels with the original resolution of $147 \mu\text{m}$ pixels, including all the phantom details.

Imaging was performed at 60 kVp and at six mAs stations in the range of 2-100 mAs, using a general radiography Bi-150 30/50 x-ray tube (Siemens, Munich, Germany) with tungsten target, a measured HVL of 1.34 mm Al (at 60 kVp), and a Heliophos 5S generator

(Siemens, Munich, Germany). Additional filtration of 6cm of lucite was used to simulate tissue and appropriately harden the beam. The block of lucite was positioned near the x-ray focus in order to reduce scatter and provide for uniform beam filtration. The phantom was imaged in contact with the detector (112 cm from the focal spot) and was placed within a wide lucite frame of equal thickness, providing uniform scatter throughout the whole phantom area. At each mAs station, we acquired five images of the phantom, as well as ten dark field (x-rays off) and ten bright field (x-rays on, with the phantom removed) images. The bright and dark fields were used for correcting the gain and offset variations of the individual detector elements (dels).

B. Image processing

The raw acquired phantom images were corrected to compensate for the effects of detector nonuniformity and adjusted for the non-linearity of human contrast sensitivity.

1. Detector nonuniformity

A standard procedure for reducing the pixel variations due to the gain and offset variations of dels is to apply a dark and bright field correction. Corrected pixel values were computed as:

$$(I_{i,j})_{corr} = K \frac{I_{i,j} - E\{D_{i,j}\}}{E\{B_{i,j}\} - E\{D_{i,j}\}} + \bar{I}_{new}, \quad (1)$$

where I and I_{corr} are the original and corrected pixel values, respectively; $E\{D\}$ and $E\{B\}$ are the averages of the dark and the bright fields, respectively; and, K and \bar{I}_{new} are parameters transforming the range (contrast) and the mean image pixel values. Subscripts i and j denote the position of the pixel in the image array.

The existence of malfunctioning dels, whose corresponding pixel values are not proportional to the incident x-ray flux and differ significantly from their neighboring pixels, was observed and the corresponding pixel values corrected. Recently, several researchers have

investigated this problem. Aach and Metzler¹⁶ proposed image deconvolution using the spectral analysis of the defect image and Tang *et al.*¹⁷ used wavelet analysis for identification and interpolation of flat panel images used for cone beam CT.

In our case, the average value and the variance of all the dark fields were computed for each del, and the same procedure was repeated for all of the bright fields. First, dels for which the digital value was constant across all of the dark- and bright- field images were identified as non-functioning. The pixels corresponding to the non-functioning dels were replaced by the average of their immediate neighbors. Second, we computed the spatial variance within 3x3 pixel neighborhoods of the phantom images, and averaged the spatial variance values over a small and large neighborhood (of size 3 and 5 pixels in diameter, respectively). The averaged variance values were then tested against the following criterion:

$$\frac{\langle \sigma \rangle_{sm}}{\langle \sigma \rangle_{lg}} > C, \quad (2)$$

where $\langle \sigma \rangle_{sm}$ and $\langle \sigma \rangle_{lg}$ are the spatial averages of the values of the pixel standard deviations, computed over the small or large neighborhood, respectively, and C is the criterion value. Pixels satisfying the criterion were replaced by the average of their immediate neighbors. Many of the affected dels were grouped along several vertical and horizontal lines. The value of parameter C that would correct all of the pixels along these lines would also produce an undesirably high number of replaced pixels randomly distributed over the image. Replacing too many correct pixels might change the statistics of the noise and affect the results of the study. Therefore, we identified the lines of malfunctioning dels in images and directly applied the correction. For the rest of the image, the value of $C = 2.1$, which produced only a small number of undesired replacements, was selected.

2. Non-linear human contrast sensitivity

Human contrast sensitivity is a non-linear function of luminance. Relative changes in luminance are more easily noticed in bright image areas than in dark areas.¹⁸ Perceptual

linearization is an image transformation that adjusts the brightness so that equal changes in the quantity being displayed (here, x-ray fluence at the detector surface) will be equally perceived. The contrast sensitivity of the human visual system is approximated by Barten's model.¹⁹ The model was derived for a standard target of a 2 deg x 2 deg square filled with a horizontal or vertical sinusoidal modulation of 4 cycles/deg, placed in a uniform background of the mean target luminance.¹⁸ The threshold modulation at which the target becomes just visible to the average observer defines the just-noticeable difference, JND, at the luminance value of the background. The interpolation of the luminance levels corresponding to 1023 JNDs is given by the grayscale standard display function:¹⁸

$$\log_{10} L(N_{\Delta}) = \frac{\sum_{i=0}^4 a_i (\ln N_{\Delta})^i}{1 + \sum_{i=1}^5 b_i (\ln N_{\Delta})^i} \quad (3)$$

where N_{Δ} and L are the JND index (i.e., the number of just-noticeable differences) and the corresponding luminance value, respectively. Coefficients a_i and b_i of the rational polynomial interpolation are given in the DICOM standard.¹⁸ We have incorporated the grayscale standard display function into the transformation from the flat-panel output 12-bit pixel value to the monitor input 8-bit digital-driver value. This transformation consists of three parts.²⁰ This decomposition offers flexibility to perform observer studies using different monitors or at different overall brightness or contrast levels.

In the first step, the monitor characteristic, relating luminance levels to the 8-bit digital driver levels, was interpolated from photometric measurements made by a TEK Lumacolor J17 photometer (Tektronix, Beaverton, OR). The luminance values were measured in the center and at the periphery of the monitor. The average values at 24 digital driver levels were used for interpolation. A fourth order polynomial fit was used for interpolation with maximum error of 1.68 digital driver levels (0.6%). Second, the transformation from the luminance values to the number of JNDs was approximated by the grayscale standard display function, given by Eq. 3. Third, the linear transformation from 12-bit flat panel output to the JND index was used to adjust the common overall brightness and contrast of all the phantom images included in the study. The overall brightness was selected in a small

preliminary observer study as the one which gave the largest increase in number of details seen stereo- vs. monoscopically. Based on that study, the mid-level between the largest, highest contrast element and its annular neighborhood was transformed to a JND index of 350, corresponding to a digital driver level of 90.

We have used two strategies for displaying the phantom images. In the first approach, we kept the contrast between the first phantom detail and its background fixed for all the images displayed in the study. The range between the average brightness in and around the first detail was mapped to a range of 328-372 JNDs, corresponding to a range of 73-110 digital driver levels. In the second approach, the images were modified to have fixed variance of the background noise. Each 12-bit pixel value was multiplied by the ratio between the standard deviation of the background noise (of the given image) and the standard deviation of the background desired for display. The new values of the average background and the background standard deviation were selected so that a range of about ± 3 background standard deviations could be shown by the 8-bit monitor digital driver levels. A discussion about the effects of display strategy on the results of the experiment is given in Section IV. In both strategies, the linear transformation from the flat-panel output to the JND index, was image dependent. An example of a processed phantom image is shown in Figure 1.

C. Observer study

1. Selection and display of images

Six medical physicists participated in the study. Each observer was presented with 60 images, consisting of 30 for monoscopic viewing and 30 for stereoscopic viewing. The monoscopic images were displayed so that both the left and right eye saw the same image, while for the stereoscopy, the left and right eye images were different. Each of the observers saw the same set of monoscopic images (there were 5 images for each of 6 exposure levels). A set of 5 out of twenty possible stereo image pairs for each mAs was selected randomly for

each observer.

The two sequences of 30 images, one for mono- and the other for stereoscopic viewing, were separately randomly permuted and then interleaved into a single sequence of the form:

$$\dots M_n S_n M_{n+1} S_{n+1} \dots,$$

where M_i and S_i represent mono and stereo images, respectively. Next, the positions of the mono and stereo images, in each mono-stereo pair, were randomly changed in order to break the repetition of mono following stereo, and to decrease possible observer bias.

2. Test of stereoscopic acuity

The stereoscopic acuity of the observers participating in the study was tested using a standard clinical test, the RANDOT Stereotest (Stereo Optical Company, Chicago, IL). The test consists of image pairs with or without angular disparity. The images in a pair are orthogonally polarized and the stereo effect is observed using appropriately polarized glasses. The images are divided into three groups with different content (geometric figures, animals, and triplets of circles) designed to assess the stereoscopic acuity in a wide range of patients' age. The images in each of the groups gradually decrease in angular disparity and roughly cover the range of 20-500 seconds of arc when viewed from 40 cm distance. Stereoscopic acuity is measured by identifying the image, and the corresponding angular disparity, beyond which the observer cannot distinguish between the objects with and without disparity. Table I shows the minimum observable angular disparity for the six observers.

3. Viewing conditions and scoring

The C-d experiments were performed in a darkened room, with a black monitor background. The distance between the observer's eyes and the monitor was approximately 1 m. The monitor used in the study was equipped for stereoscopy with a stereoscopic goggles system (StereoGraphics, San Rafael, CA). A transmission box, attached to the monitor,

controlled the opening and closing of the liquid crystal shutters in the goggles synchronously with the changing of the image on the monitor. Therefore, each of the eyes was presented the corresponding image with a repetition frequency of 56 Hz. The goggles were used for both mono- and stereo experiments to provide a comparable brightness level in both experiments.

Several training sessions for image scoring were organized for observers in order to establish a uniform decision criterion. The observers were trained to inspect the objects from largest to smallest and from greatest to least contrast. The objects were inspected for general roundness ("whether or not more than 50% of the edge was visible"), size ("whether or not more than 50% of the object was missing"), and the expected position in the detail array. The goal was to prevent misinterpretation of the clustered background noise as phantom details. A graphical user interface was developed allowing an observer to identify the smallest detail seen in a column by clicking over the detail position.

We have analyzed the relationship between the inter- and intra-observer variability, by having one of the observers additionally reading all the C-d experiments in the study. Thus, we could compare the average C-d performance of a group of observers with a single round of experiments, and the average performance of a single observer after repeating the study multiple times.

For further comparison, we have also repeated the C-d experiments for all the observers without the use of the stereoscopic goggles. Due to the 112 Hz switching between the two stereoscopic images on the monitor, the observers were, effectively, presented with an average of the left and right eye image. Therefore, we could compare the performance of observers attempting to utilize information from disparate images with the performance of observers looking at the combined images.

III. RESULTS

The observers took, on average, 39 minutes (std. dev. = 2.8 minutes) to score a set of 60 combined mono and stereo images. Figure 2 shows the number of details seen mono-

and stereoscopically by a single observer, averaged over all images with the same mAs. Figure 3 shows the difference between the number of details for stereo and mono images, for all the observers. When averaging over different observers, we have included the results of all but one of the observers. This observer reported uncorrected vision in one eye, corresponding to low stereo acuity, and demonstrated a large value of the minimum observable angular disparity in the stereo vision RANDOT test (Table I, Observer 6). Furthermore, the difference between the number of details seen stereo- vs. monoscopically, for the observer in question (Figure 3, points labeled by triangles) was significantly smaller compared to the others. We have compared the stereo- and monoscopic performance of the observers by analysis of the C-d curves and an analysis of the SNR.

A. Analysis of C-d curves

For a low-contrast object with given thickness t and diameter d , contrast is proportional to t , and the detectability is determined by the signal-to-noise ratio, $\text{SNR} = t d K \sqrt{X}$, where X is the exposure in mAs and K is a proportionality constant. C-d curves relate the diameter and thickness of objects at the limits of visibility. Ideally, the (t, d) points in C-d experiments would form a line with negative unit slope on a log-log plot, satisfying:

$$\log_{10} t + \log_{10} d = \log_{10} \text{SNR}_T - \log_{10} K - \frac{1}{2} \log_{10} X, \quad (4)$$

where SNR_T is the value of the SNR at the threshold of perception.

For each observer we calculated their C-d curves by averaging the size of the smallest visible detail in each column, over a set of images, e.g., for the same exposure. Computing the average detail size is problematic when no details are visible in a given column for one or more images, since the contribution of those images to the average is ambiguous. To avoid this problem, we chose the median diameter for generating C-d curves. Figure 4 shows the average C-d curves for a single observer (the same observer as in Figure 2). Comparison of the C-d curves corresponding to stereo- and monoscopic viewing has been performed

using the approximation of a line with negative unit slope, as per Eq. 4. The difference in the intercept values between the fitted stereo and mono C-d curves can be related to the effective exposure for stereoradiography, assuming the same threshold SNR for mono and stereo experiments, by

$$\log_{10} d_M - \log_{10} d_S = \log_{10} \frac{d_M}{d_S} = \log_{10} \sqrt{\frac{X_{Seff}}{X_M}}, \quad (5)$$

where d_M and d_S are the diameters of the smallest visible details viewed mono- and stereoscopically, respectively, for the same detail thickness. X_M is the exposure used in acquiring the projection viewed monoscopically, and X_{Seff}/X_M is the ratio of the effective stereoscopic exposure (in terms of object visibility) to the exposures used to produce the individual projections. Thus, X_{Seff} is defined as the exposure needed to obtain an image which, when viewed monoscopically, would produce the same C-d characteristic as the stereo image in question. If our hypothesis that human observers can combine information from both images is true, then the intercepts of the corresponding linear fits to the C-d curves would be separated by $\sqrt{2}$. Figure 5 shows the linear approximation of the C-d curves for a single viewer.

Figure 6 (a) shows the relative reduction in exposure when using stereo- rather than monoscopic viewing normalized with the hypothesized reduction by half. Plotted are the percent values of $R_X = X_{Seff}/(2 X_M) = [d_M/(\sqrt{2} d_S)]^2$, averaged over all the observers, for both display conditions for each per-projection exposure level. If the hypothesis is true, the ratio R_X would be equal to 100%. Figure 6 (b) presents R_X for multiple readings done by a single observer and both display conditions. For clarity of presentation, the results obtained with different display conditions are slightly horizontally displaced on the graph.

B. Analysis of SNR cut-off

The objects used in this observer study were of low contrast and imaged on a detector with essentially no correlation in the noise between detector elements (a white noise power

spectrum)¹⁵. Therefore, for monoscopically viewed images the classic Rose model^{21,22} is applicable, in which the signal-to-noise ratio (SNR_M) can be computed from the subject contrast and the standard deviation in the pixels values, and object visibility is directly related to SNR_M . The subscript "M" is used here to emphasize that this is the SNR applicable to an analysis of viewing a single image. In Figure 7 the number of objects visible as a function of exposure were calculated for a class of ideal observers which would detect all objects above a given threshold SNR_{T_M} . Thresholds SNR_{T_M} of two through seven are shown; the number of objects decreases with increasing threshold. Superimposed on Figure 7 are the fits to the actual performance of one observer from Figure 2. For monoscopic viewing, the data for this observer falls between the theoretical curves corresponding to SNR_M thresholds of 5 and 6, (in agreement with the customary range of estimates of Rose's k). For an observer capable of combining information from stereoscopic images the signal-to-noise ratio of each object should increase by a factor of $\sqrt{2}$, (i.e., $\text{SNR}_S = \sqrt{2} \text{SNR}_M$), so that the object count as a function of per-projection exposure would correspond to a monoscopic signal-to-noise ratio cut-off reduced by a factor of $\sqrt{2}$. Consistent with this, the real observer from Figure 7 does show an increased sensitivity, as will be discussed in detail later.

Following the Rose model, the results were analyzed by identifying a threshold SNR under each viewing condition. For each observer scoring of the phantom, the detected details had greater SNR_T than the details not detected, with only a few details near the threshold not following this pattern. Thus, for each observer scoring of the phantom, the threshold was calculated as the mean of the smallest SNR_M of the details detected and the largest SNR_M of the details not detected. The averages of these per-scoring values over the 5 monoscopic viewings give the monoscopic threshold SNR_{T_M} for each viewer at each exposure level, and similarly the 5 stereoscopic viewings give SNR_{T_S} . A hypothetical observer capable of reducing the quantum noise in the phantom images by using information from both images of the stereoscopic pair would then effectively find the signal to noise ratio of each disk increased by a factor of $\sqrt{2}$, and thus would present a decrease in the SNR_M of the threshold objects by a factor of $1/\sqrt{2}$. Thus, for such a hypothetical observer, one expects

the ratio $R_{SNR} = \text{SNR}_{T_M}/\text{SNR}_{T_S} = \sqrt{2}$. Figure 8 (a) shows the ratio R_{SNR} averaged over all the observers at each exposure level. Figure 8 (b) shows the and the ratio R_{SNR} for multiple readings performed by a single observer. Discussion of the experimentally observed results is presented in the next section.

IV. DISCUSSION

A. Effects of display conditions

The transformation from the flat panel 12-bit output to the number of JNDs was implemented in an image dependent fashion, as described in Section II, by keeping fixed (a) the background contrast of the largest detail or (b) the standard deviation of the background noise, in all the displayed images. Using the first approach, images acquired with high nominal exposure were displayed such that the background noise range was limited to only a few 8-bit digital driver levels, with the potential for quantization distortion. The latter approach, however, changed the contrast of the largest detail in the images with different exposures, which could lead to possible saturation of the display. Moreover, the perceptual linearization is a nonlinear transformation that may affect the perception of the noise patterns. The effects of these issues on the results of the C-d experiment are not obvious.

For all performance measures and both display conditions, we observed better agreement with theory at lower exposures. The normalized effective dose ratio (Figure 6) at the higher exposures, showed more benefits from stereoscopy for the images displayed with fixed noise, than for the images with fixed contrast. The SNR ratio is near $R_{SNR} = \sqrt{2}$ at low exposures, as expected for the hypothetical observer combining information from each of the stereo pair of images. At higher exposures, the ratio is less, but still greater than one.

The value of the normalized effective dose ratio, averaged over all six mAs stations, is $R_X=89.7\%\pm 8.4\%$, corresponding to a reduction in threshold SNR of $R_{SNR}=1.339\pm 0.066$, for the images displayed with fixed contrast, and $R_X=94.2\%\pm 5.0\%$, corresponding to

$R_{SNR}=1.372\pm 0.038$, for the images with fixed noise (compare with Figure 8). The total dose to obtain a stereo pair $D_S = D_M/R_X = 2D_M/R_{SNR}^2$ where D_M is the dose for a single radiographic projection. Thus, stereomammography requires a dose of $1.12\pm 0.13 D_M$ to $1.06\pm 0.06 D_M$, for the respective values of R_{SNR} .

The obtained reduction in the SNR threshold can be compared with the results reported by Hsu *et al.*¹³. In that study of stereomammographic detection of simulated objects, the performance was evaluated by an ROC analysis. Reported values of the area under the ROC curve, A_z , were 0.82 (stereo) vs 0.74 (mono) for their arrangement experiment, and 0.75 (stereo) vs 0.71 (mono) for their density experiment. Assuming that A_z is equal to the probability of correct detection, the corresponding reduction in threshold SNR can be computed as the ratio of stereoscopic and monoscopic d' values²³, yielding $R_{SNR} = 1.423$ for the arrangement experiment and $R_{SNR} = 1.219$ for the density experiment.

We have performed an additional validation of the contrast-detail experiment results by comparing the performance measures averaged over five observers with the average performance of repeated readings by a single observer (see Figure 6 (b) and 8 (b)). There is little difference in the results of these experiments.

B. Effects of viewing condition

Results of the C-d experiments with and without the stereoscopic goggles are shown in Figure 9. The error bars correspond to the standard error of the average values. For clarity of presentation, the 2 datasets are slightly displaced on the graph. Normalized dose ratio, averaged over all 5 observers (solid lines) was compared with the performance of observer 6, with low stereo acuity (dashed lines). While the average performance of the five observers with (bold) and without the goggles (thin) did not differ significantly, observer 6 performed much better without the goggles. This was expected as when using the goggles the image shown to the uncompensated eye of the low stereo acuity observer was effectively unused under either the stereoscopic or monoscopic viewing conditions, therefore showing basically

no advantage of stereoscopy. Without the goggles, an averaged image was shown to both eyes, and the difference in the background noise for the mono and stereo images became visible, without, however, the advantage of parallax.

C. Effects of additive detector noise

The images used in this study were acquired radiographically, with a digital x-ray detector. All images, regardless of mAs, were x-ray quantum noise limited, rather than detector noise limited. Thus, in the C-d experiments reported, the limiting factor for detection was the x-ray quantum fluctuations. Furthermore, a detector entrance exposure of 10 mR, typical for the detector being evaluated, would have required a technique of 14 mAs. Hence, the results reported are likely to be generally applicable to digital radiography and digital mammography. Extensions of this approach can be envisioned to address the issue of the dose requirements for tomosynthesis. However, in that instance, careful evaluation of the dominant noise source in the individual projections, and in the reconstructed data is necessary.

D. Other issues affecting the efficiency of stereoscopic viewing

The following issues are potential sources of concern in our experiment. Since it was, to the best of our knowledge, the first C-d study of the stereoscopic viewing in radiography, no reference suggestions were found to address the experimental design. Future experiments, modified to improve the following conditions, may give a more accurate estimate of the advantages of stereoradiography.

Observers used the stereoscopic goggles while viewing both mono and stereo images, in order to keep the average brightness level comparable and reduce bias of having the mono images directly identified. The goggles reduce the brightness level of the scene. We have not analyzed the amount of this brightness reduction, nor its uniformity with the change of brightness. Perceptual linearization was applied without taking into account this brightness

reduction, and this might be of concern if the non-linearity of the human contrast sensitivity was not properly compensated. Note, also, that structured anatomic noise is not included in this set of test images, but its modeling is considered for future research.^{24,25} We have also begun another approach to testing the hypothesized benefits of stereoradiography using a 2-alternative forced-choice experiment.

V. CONCLUSIONS

A series of C-d experiments was performed, testing the hypothesis that the radiation dose required for stereoradiography is one half the dose for a single x-ray image viewed monoscopically, due to the combination of images by the human visual system. For images acquired at a fixed exposure, more objects were detected under stereoscopic than monoscopic viewing conditions. For the lower range of the x-ray exposures tested, where the quantum fluctuations were easily visualized, the increase in the number of details observed was the same as expected for a hypothetical observer combining the two projections to remove noise. With increasing x-ray exposure, the increment between the number of objects detected under stereoscopic and monoscopic conditions decreased, but was always positive. The experimental results indicate that a stereoradiograph can be acquired at a dose approximately 1.1 times that of a single projection radiograph. The study results are potentially influenced by the brightness reduction of stereoscopic goggles, background noise quantization, and the lack of anatomical noise.

ACKNOWLEDGMENT

This work was funded by the U.S. Department of Defense, Grant DAMD 17-98-1-8169. The authors are grateful to Dan Beideck, Scott Cupp, Natasa Milojkovic, and William Tao Shi for participating in the experiment.

REFERENCES

- ¹ E. Thomson, "Stereoscopic roentgen pictures," *Electrical Engineer* **21**, 256 (1896).
- ² S.L. Warren, "The roentenologic study of the breast," *Am. J. Roentgenology* **24**, 113-124 (1930).
- ³ T.S. Curry, III, J.E. Dowdey, R.C. Murry, Jr., *Christiansen's Physics of Diagnostic Radiology*, 4th ed. (Lea & Febiger, Philadelphia, PA, 1990).
- ⁴ C.A. Jacobi and D.Q. Paris, *Textbook of Radiologic Technology*, 6th ed. (The C.V. Mosby Company, St. Louis, MO, 1977)
- ⁵ M. Tortorici, *Concepts in Medical Radiographic Imaging: Circuitry, Exposure, and Quality Control* (W.B. Saunders Co., Philadelphia, PA, 1992).
- ⁶ J. Berkson, C.A. Good, D.T. Carr, and A.J. Bruwer, "Identification of "positives" in roentgenographic readings," *Am. Rev. Resp. Dis.* **81**, 660-665 (1960).
- ⁷ R.R. Carlton and A. McKenna Adler, *Principles of Radiographic Imaging: An Art and a Science* (Delmar Publishers, Inc., Albany, NY, 1992).
- ⁸ R.W. Reading, *Binocular Vision: Foundations and Applications* (Butterworths, Boston, MA, 1983).
- ⁹ H.L. Kundel, P.R. Lynch, L. Peoples, and H.M. Stauffer, "Evaluation of observer performance using televised stereofluoroscopy," *Investigative Radiology* **2**, 200-207 (1967).
- ¹⁰ F.W. Campbell and D.G. Green, "Monocular versus binocular visual acuity," *Nature* **208**, 191-192 (1965).
- ¹¹ C.W. Tyler, "Cyclopean vision," in *Binocular Vision*, edited by D. Regan (CRC Press, Boca Raton, 1991) [Vision and Visual Dysfunction **9**, pp. 38-74].
- ¹² M.M. Goodsitt, H.-P. Chan, and L. Hadjiiski, "Stereomammography: Evaluation of depth perception using a virtual 3D cursor," *Med. Phys.* **27**, 1305-1310 (2000).

- ¹³ J. Hsu, D.M. Chalberg, C.F. Babbs, Z. Pizlo, and E. Delp, "Preclinical ROC studies of digital stereomammography," *IEEE Trans. Med. Imaging* **14**, 318-327 (1995).
- ¹⁴ G. Cohen, "Contrast-detail analysis of imaging systems: caveats and kudos," in *Recent Developments in Digital Imaging*, edited by K. Doi, L. Lanzl, and P.-J.P. Lin (American Institute of Physics, New York, 1985), pp. 141-159,
- ¹⁵ E.L. Gingold, D.L.Y. Lee, L.S. Jeromin, B. Rodricks, M.G. Hoffberg, and C.L. Williams, "Development of a novel high-resolution direct conversion x-ray detector," in *Physics of Medical Imaging*, edited by J.T. Dobbins III and J.M. Boone [Proc. SPIE **3977**, 185-193 (2000)].
- ¹⁶ T Aach and V. Metzler, "Defect interpolation in digital radiography – how object-oriented transform coding helps," in *Image Processing*, edited by M. Sonka and K.M. Hanson [Proc. SPIE **4322**, pp. 824-835 (2001)].
- ¹⁷ X. Tang, R. Ning, R. Yu, and D. Conover, "Cone beam volume CT image artifacts caused by defective cells in X-ray flat panel imagers and the artifact removal using a wavelet-analysis-based algorithm," *Med. Phys.* **28**, 812-825 (2001).
- ¹⁸ *DICOM Standard PS-3.14-2000: Gray-scale Standard Display Function* (National Electrical Manufacturers Association, Rosslyn, VA, 2000).
- ¹⁹ P.G. Barten, "Physical model for the contrast sensitivity of the human eye," in *Human Vision, Visual Processing and Digital Display*, edited by B.E. Rogowitz [Proc. SPIE **1666**, 57-72 (1992)].
- ²⁰ P.R. Bakic, M. Albert, and A.D.A. Maidment, "Dose requirements in stereoradiography," in *Physics of Medical Imaging*, edited by L.E. Antonuk and M.J. Yaffe [Proc. SPIE **4682**, 126-137 (2002)].
- ²¹ A. Rose, *Vision: Human and Electronic* (Plenum, New York, NY, 1973).
- ²² A.E. Burgess, "The Rose model, revisited," *J. Opt. Soc. Am. A* **16**, 633-646 (1999).
- ²³ D.M. Green and J.A. Swets, *Signal Detection Theory and Psychophysics* (John Wiley and Sons,

Inc., New York, NY, 1966)[Section 2.6, p. 47].

²⁴ F.O. Bochud, C.K. Abbey, and M.P. Eckstein, "Statistical texture synthesis of mammographic images with clustered lumpy backgrounds," *Optics Express* **4**, 33-43 (1999).

²⁵ P.R. Bakic, M. Albert, D. Brzakovic, and A.D.A. Maidment, "Mammogram synthesis using a 3D simulation. II. Evaluation of synthetic mammogram texture" *Med. Phys.* **29**, 2140-2151 (2002).

FIGURES

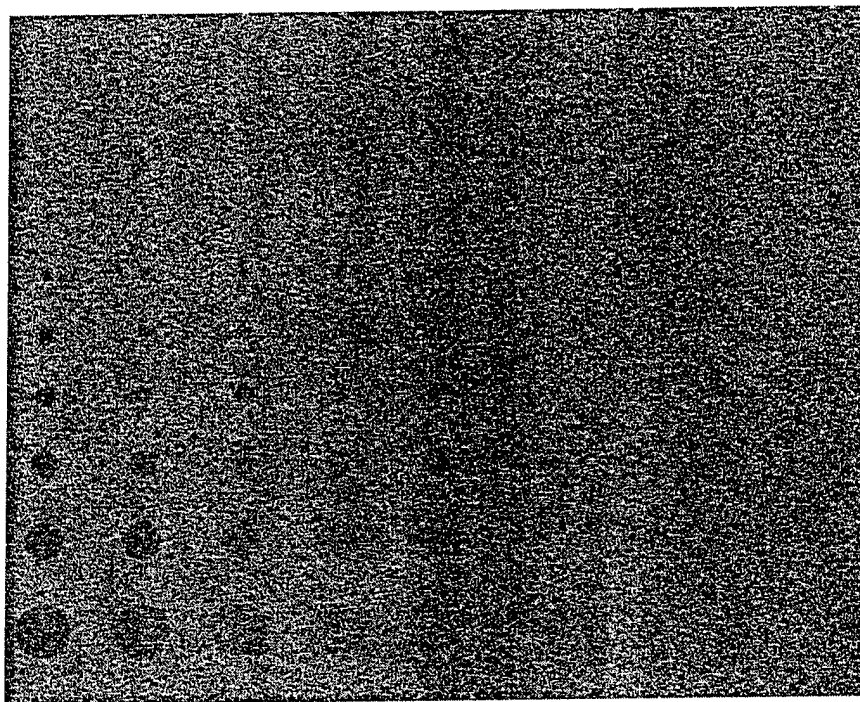


FIG. 1.

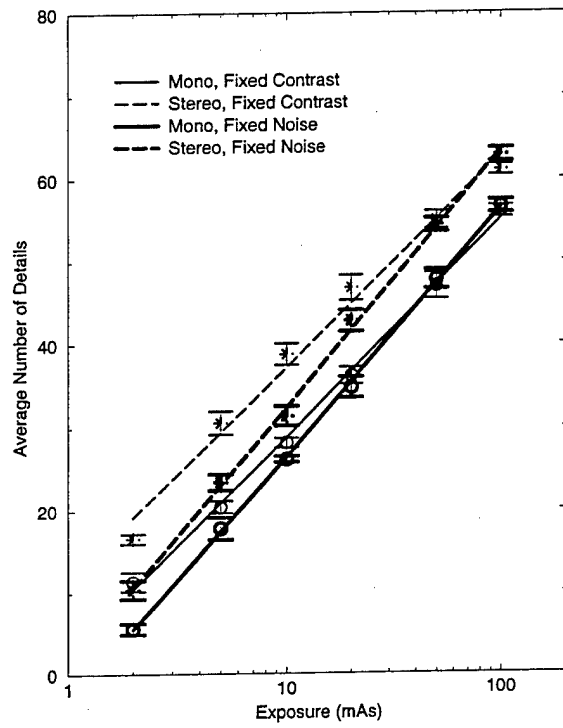
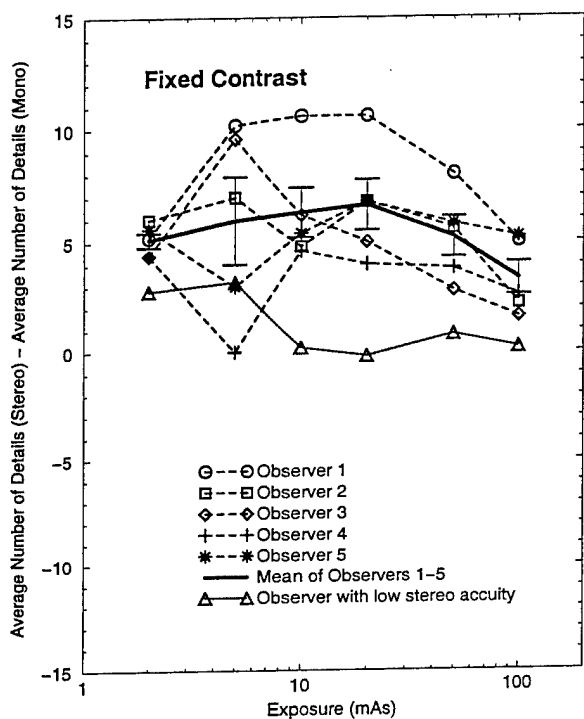
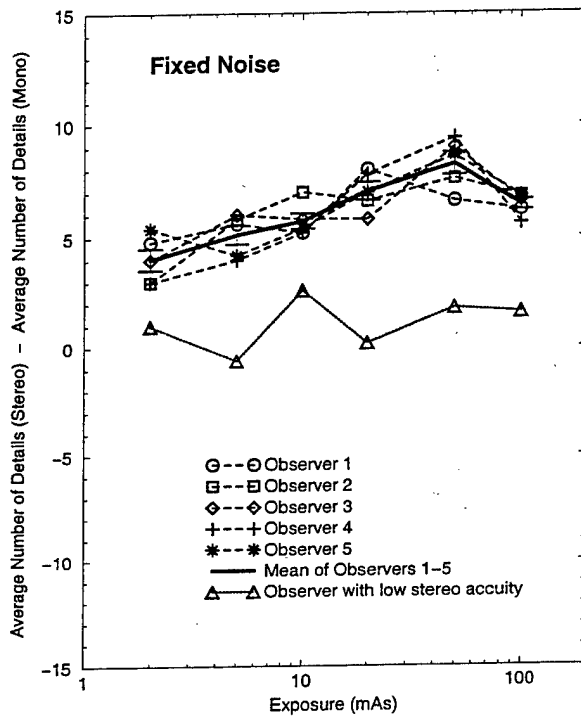


FIG. 2.



(a)



(b)

FIG. 3.

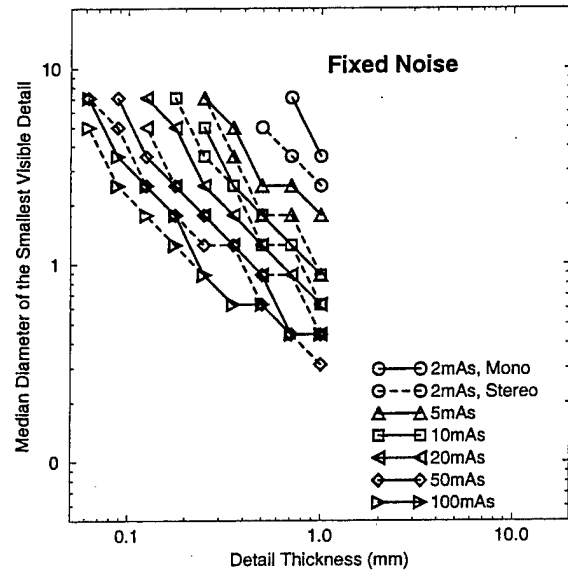
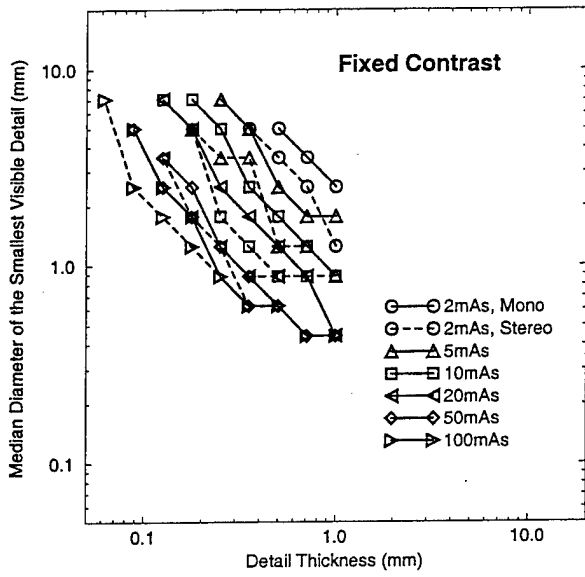


FIG. 4.

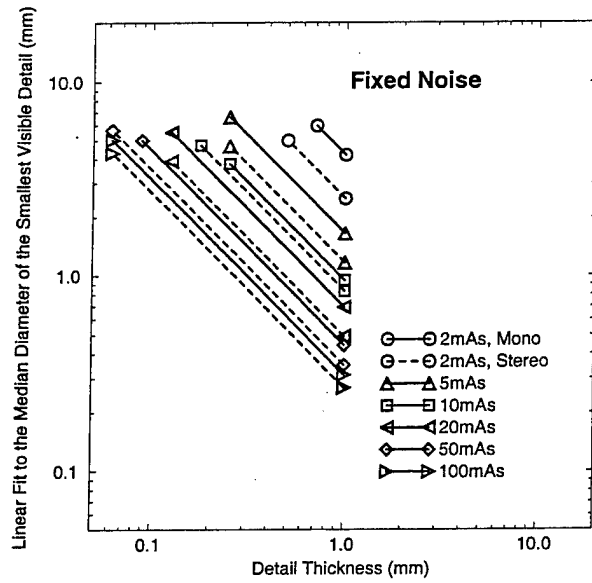
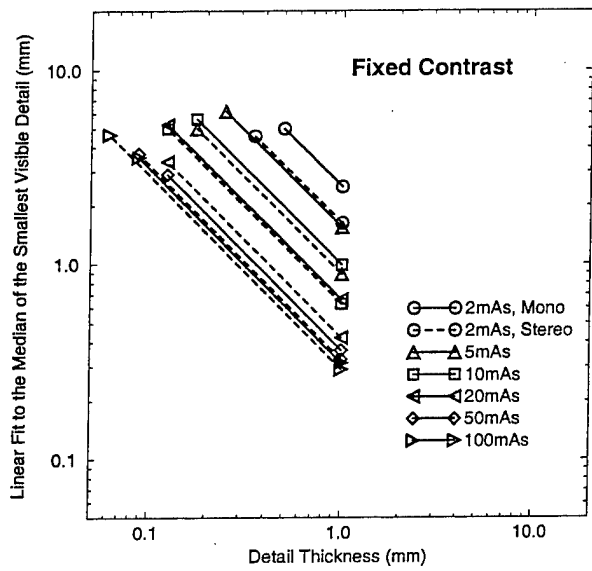


FIG. 5.

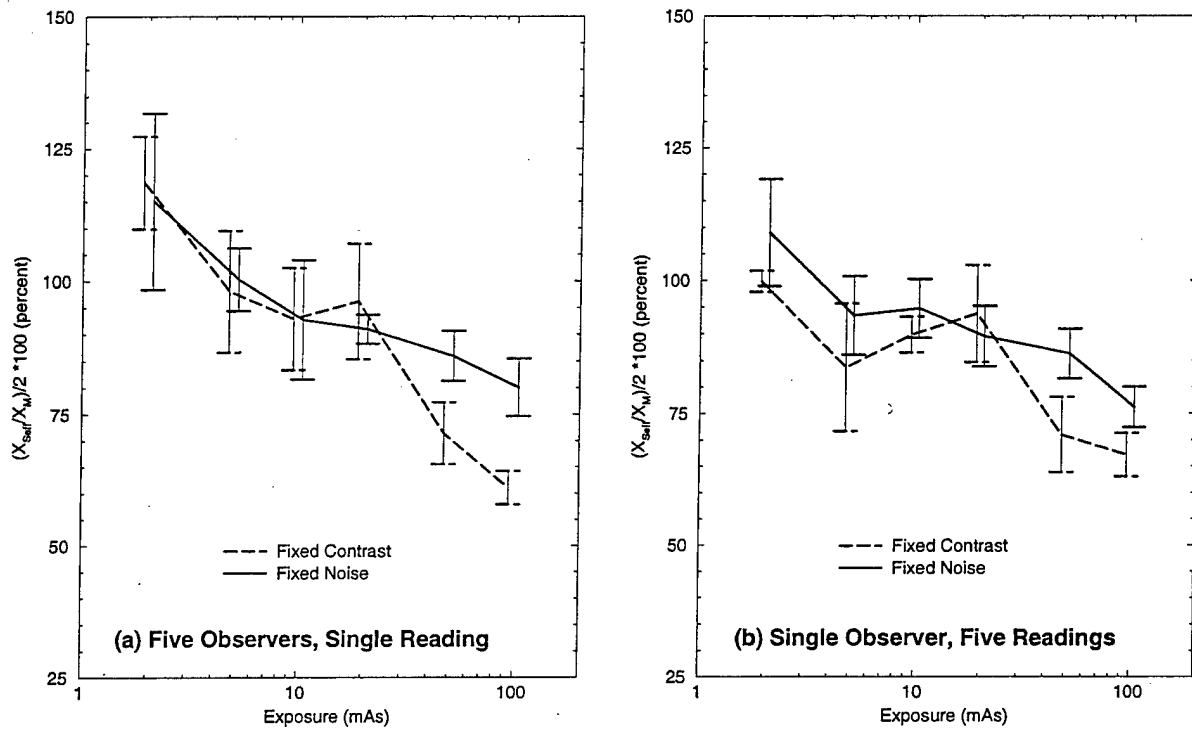


FIG. 6.

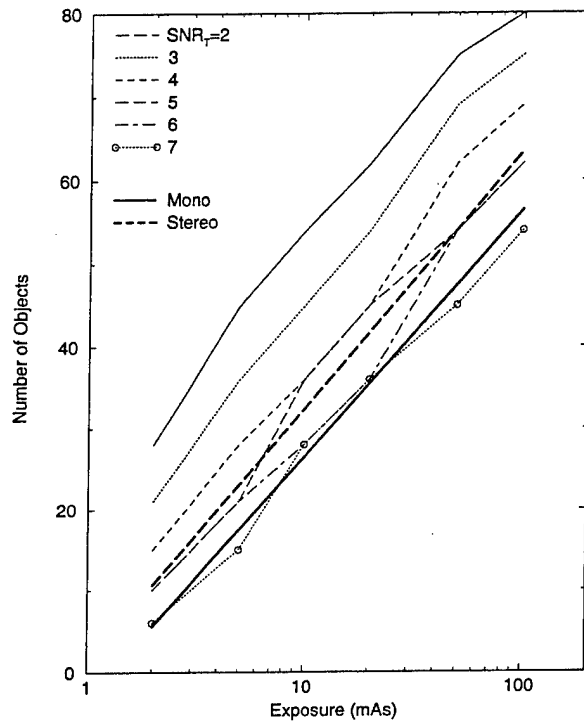


FIG. 7.

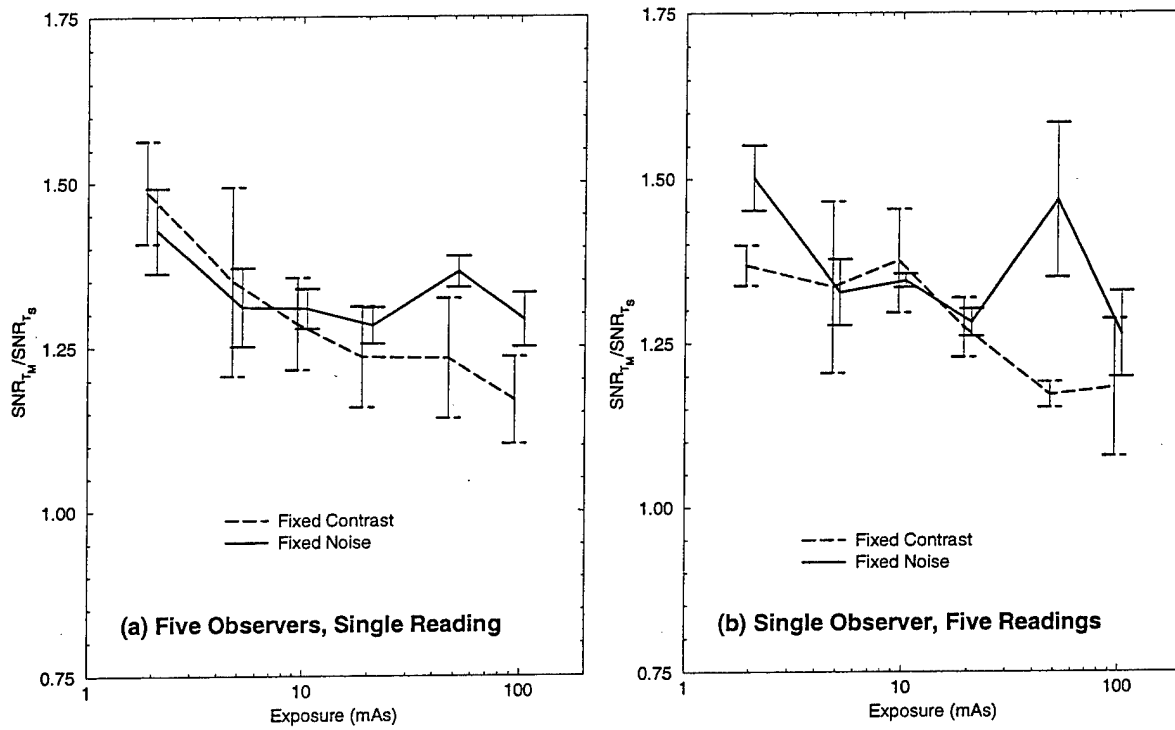


FIG. 8.

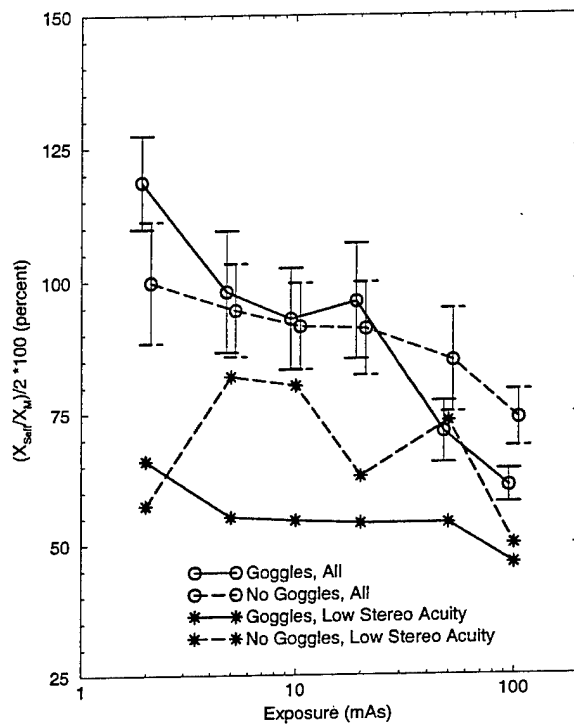


FIG. 9.

Fig 1 An example of a phantom image used in the study. The image was acquired with an exposure of 10mAs and post-processed to compensate for the effects of detector nonuniformity and to adjust for the non-linearity of human contrast sensitivity.

Fig 2 Number of details seen in the C-d phantom for two image display modes: fixed contrast (thin) and fixed noise (bold). Shown are the average number of details (symbols), the standard error (bars), and the linear fits (lines), for mono- (solid) and stereoscopic (dashed) viewing.

Fig 3 Comparison between mono- and stereoscopic viewing. (a) Difference in the number of objects seen by stereo- vs. monoscopy, for each observer, and images displayed with fixed contrast. (b) Difference in the number of objects seen by stereo- vs. monoscopy, for each observer, and images displayed with fixed noise.

Fig 4 C-d curves for a single observer (observer 1), for monoscopic (solid) and stereoscopic (dashed) viewing, and two display conditions: (a) with fixed contrast and (b) with fixed noise.

Fig 5 Linear approximation of C-d curves for a single observer (observer 1), for monoscopic (solid) and stereoscopic (dashed) viewing, and two display conditions: (a) with fixed contrast and (b) with fixed noise.

Fig 6 Normalized dose ratio, $[X_M/X_S]/2 = [(d_M/d_S)^2]/2$, as a function of exposure, for two display conditions, and averaged: (a) over 5 observers and (b) over 5 readings by a single observer (observer 3). Bars represent the ranges of \pm one standard error.

Fig 7 Number of details seen in the C-d phantom by an ideal observer, with various threshold SNR values (thin). The results for the real observer from figure 2, the fixed noise display and stereoscopic viewing (bold line) are given for comparison.

Fig 8 Comparison of the observers mono- and stereoscopic performance using the analysis of the SNR cut-off values for two display conditions, and averaged: (a) over 5 observers

and (b) over 5 readings by a single observer (observer 3). Bars represent the ranges of \pm one standard error.

Fig 9 Comparison of the normalized dose reduction for the C-d experiments with (bold lines) and without (thin lines) the stereoscopic goggles. Shown are the results averaged over 5 observers (solid lines) and for a single observer with low stereoscopic acuity (dashed lines).

TABLES

TABLE I.

Observer	$\Delta\alpha_{min}$ [arc sec]
1	25
2	70
3	30
4	25
5	25
6	200

Table I Results of the RANDOT stereo test for six observers. Tabulated are the values of the minimum observable angle of stereo disparity in seconds of arc.